Control of scattered coherent light and photoacoustic imaging : toward light focusing in deep tissue and enhanced, sub-acoustic resolution photoacoustic imaging

Thomas Chaigne

ESPCI ParisTech | UPMC Sorbonne Universités | Institut Langevin Ondes et Images | Laboratoire Kastler Brossel Physique quantique et applications

THÈSE DE DOCTORAT DE L'UNIVERSITÉ PARIS 6

Spécialité

Physique

Présentée par

Thomas Chaigne

Pour obtenir le grade de

DOCTEUR de l'UNIVERSITÉ PARIS 6

Sujet de la thèse :

Control of scattered coherent light and photoacoustic imaging: toward light focusing in deep tissue and enhanced, sub-acoustic resolution photoacoustic imaging

Soutenue le 7 janvier 2016

devant le jury composé de :

M.	**MERTZ**	**Jérôme**	**Rapporteur**
M.	**RIGNEAULT**	**Hervé**	**Rapporteur**
Mme.	**FRAGOLA**	**Alexandra**	**Examinateur**
M.	**NTZIACHRISTOS**	**Vasilis**	**Examinateur**
M.	**PSALTIS**	**Demetri**	**Examinateur**
M.	**GIGAN**	**Sylvain**	**Directeur de thèse**
M.	**BOSSY**	**Emmanuel**	**Co-directeur de thèse**

Contents

Introduction

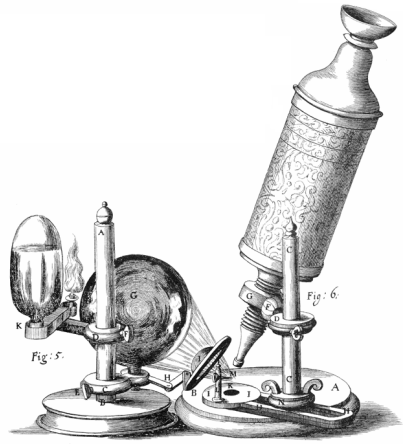

Figure 1 – Hooke's microscope apparatus, from [Hooke 03]

Optical microscopy appeared at the end of the 17^{th} century, understood as the observation with magnifying lenses of objects invisible to the bare eye because of their microscopic size. It immediately enabled wide progress, in particular in biology where a brand new microscopic wildlife was now accessible. Among the first scientific publications on microscopic observations, we can cite Robert Hooke's work [Hooke 03], which first described the various microscopic structures of cloth, tree bark, human skin pores, and small insects such as fleas or louses. Optical microscopy played a fundamental role in the discovery of microbial life by Pasteur, and helped to eradicate in a few decades several contagious diseases that had been devastating populations for centuries.

Among other breakthroughs, Santiago Ramon y Cajal unraveled the neuronal structure of the brain in 1887 [Ramon Y Cajal 04]. "A look was enough" to establish that the brain was made of interconnected discrete cells rather than of a continuous network, which was not an evidence at that time. One shall appreciate the artistic quality of Hooke's and Cajal's drawings, as no camera was available at this time to imprint their observations. All of these discoveries were made based on the observation of thin samples. For instance, Alexandre Yersin discovered the plague bacillus by looking at serous liquid from buboes, and Cajal's observations were performed using histological thin brain sections.

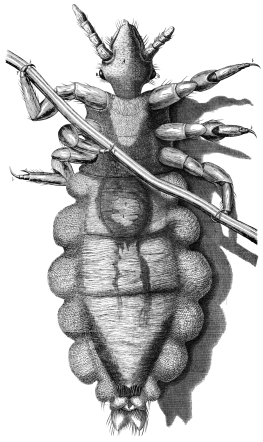

Figure 2 – Louse as drawn by Hooke [Hooke 03]

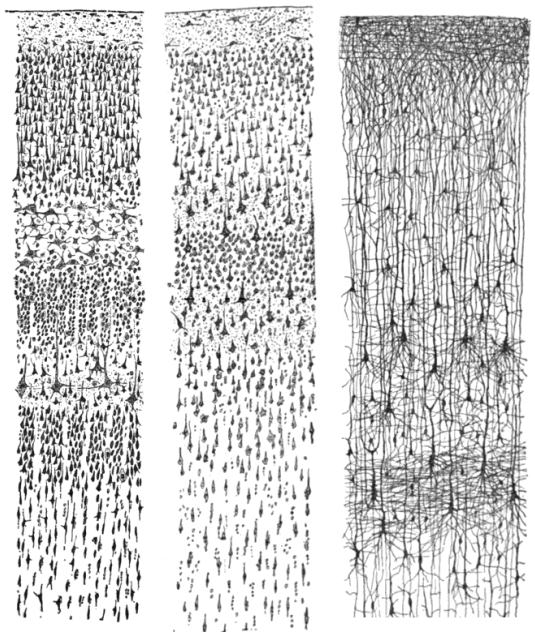

Figure 3 – Different portions the human cortex, as drawn by Cajal [Ramon y Cajal 99]

This might obviously be for a practical purpose, a glass slide of a few centimeters being easier to handle than a suppurating patient. However, this also originates from a simple analysis: one cannot see through biological tissue, and the potential objects of interest must be extracted from their opaque surrounding before any observation. Light does actually propagate through turbid tissues, but it is scattered by the complex microscopic structure, scrambling any information about the embedded objects. For a long time, optical microscopy has been restricted to transparent thin samples, while many other biomedical imaging modalities were significantly developed during the past few decades. Deep tissue high resolution optical imaging would still be of primary importance as it could combine non-ionizing radiations, high contrast, high resolution, and high frame rate at relatively low cost, as opposed respectively to X-ray imaging, ultrasound imaging, and magnetic resonance imaging.

Significant progress has been made toward this goal in the past 30 years. Ballistic photons filtering techniques have been developed to image using only these photons propagating in straight lines inside the tissue, thus retaining some information. Adaptive optics techniques, inspired by recent developments of astronomical observation, have been designed to compensate for the low order fluctuations of the refractive index in tissue. However, beyond one millimeter, none of these techniques could be employed because an overwhelming majority of photons have been scattered, and become useless for optical imaging. Or do they? Since 2007, following a seminal experiment by Vellekoop and Mosk [Vellekoop 07], numerous works have shown that scattered coherent light could actually be controlled using spatial light modulators (SLM). This approach has been enabled by recent innovations in electronics and in micro-mechanical technologies. It is based on optical phase conjugation and on studies of wave propagation in scattering disordered media. The limited number of controllable degrees of freedom prevent from perfectly correcting the tissue turbidity, but it still allows to focus light down to the optical diffraction limit with a very high contrast. These works hold great promise for high resolution optical imaging inside biological tissue,

using only scattered light. However, many of these techniques require a feedback signal monitoring the light intensity at the location where one wants to focus light. In most of these works, the feedback signal was obtained from a photodetector placed at the targeted location. In most practical scenarios though, one cannot directly place such a detector inside scattering tissue.

In this thesis, we extensively study the potential use of photoacoustic imaging to measure this light intensity feedback deep inside soft tissue. Photoacoustics is indeed an effective approach to image absorbing structures inside tissue. After absorption of a short optical pulse, these structures generate broadband ultrasound waves that can be detected with an external transducer. This imaging modality has been developed for two decades and benefits from the recent development of high sensitivity ultrasonic probes. In the first chapter of this thesis, we introduce the basic principles of optical resolution imaging, and detail to which extent it is impaired by light scattering. We then describe how coherent scattered light can be manipulated via wavefront shaping, and list the potential attempts to apply it to deep tissue imaging. We also provide theoretical elements about photoacoustics, as well as a brief description of ultrasonic detection and image reconstruction, which will be needed throughout the manuscript. In the second chapter, we show that the combination of optical wavefront shaping with photoacoustic imaging enables to focus light on absorbing structures without any direct optical access to the target location. We specifically adapt the concept of transmission matrix to photoacoustic-guided wavefront shaping, which allows to focus at any desired position after one single set of measurement. In the third chapter, we show how the broadband nature of the photoacoustic signals can be used to confine the light focus on tighter regions. In the fourth chapter finally, we show how the simple use of coherent light for photoacoustic imaging enables to overcome common imaging artefacts. As opposed to the conventional incoherent illumination, we show that the spatial and temporal fluctuations of the illumination pattern generated at depth can improve both the visibility and the resolution of photoacoustic imaging.

Chapter 1

Optical imaging in the ballistic regime and beyond

Contents

In this chapter we describe the scientific context in which this PhD study has been carried out. We first introduce some basic principles of optical imaging in homogeneous media. The second point of this introduction is to show how the performances of a simple microscope are degraded when it comes to imaging at depth in biological tissue. To this purpose, we first present a few general notions about light scattering, and we show to which extent it can describe the optical properties of biological tissues. We present a number of techniques to palliate scattering in tissue, and show that they share an ultimate limitation. We finally propose to combine optical wavefront shaping and photoacoustic (PA) imaging, an original imaging modality that benefit from the reduced ultrasound scattering in soft tissue. In order to facilitate the reading of the next chapters, we introduce basic notions of PA generation and its use for imaging purpose.

1.1 Basics of optical resolution imaging

The aim of a microscope is to image and magnify an object, usually too small so that interesting features cannot be accurately distinguished with bare eye. The image represents the spatial distribution of some optical properties, the contrast, of the object, such as absorption. This image can provide structural information about the object, as well as more complex information such as chemical composition. Many different optical properties can be probed using a variety of optical imaging techniques. In this section, we will try to extract general characteristics shared by many of these techniques. One objective is to highlight that the ability to focus light plays a key role in numerous applications.
An optical imaging system such as a microscope can be decomposed into two parts: illumination and detection. These two features interlock around the contrast mechanism. We can essentially sort microscopy techniques into two different categories, depending on the illumination and collection schemes used. The distinction is specifically made whether the resolution is provided by the detection or by the illumination. This discrimination is somehow porous (considering structured illumination microscopy for instance [Neil 97]), but it still allows to emphasize common characteristics.

The first category uses wide-field illumination combined with one or several lenses that form the detection apparatus. In its most basic form, the usual setup consists of two lenses in a 4-f configuration (see Fig. 1.1).

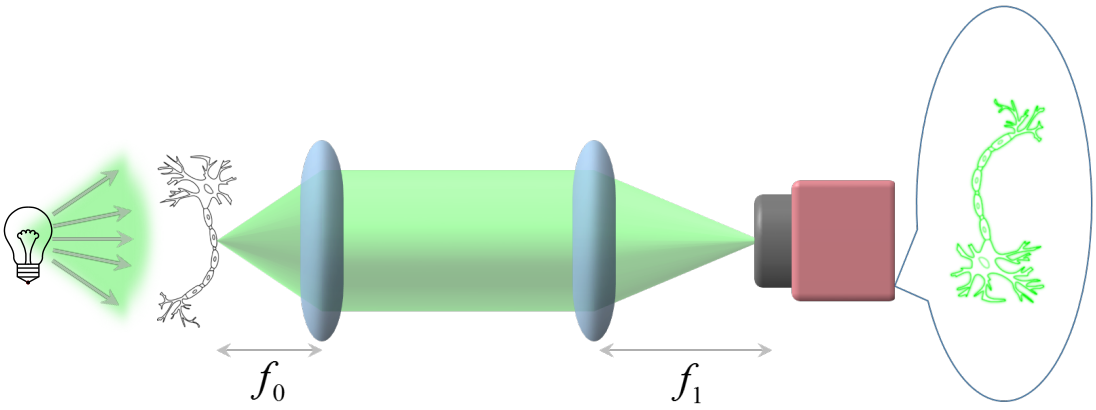

Figure 1.1 – Basic wide-field microscopy setup. From left to right: plane waves illuminate the sample of interest, located in the focal plane of the first lens (focal length f_0). The second lens (focal length f_1) forms the image on a camera. The setup is presented in transmission geometry, but can be easily extrapolated in reflection. In the general case, the image and object planes are only conjugated in intensity. If the two lenses are separated by $f_0 + f_1$, the conjugation is perfect (both in phase and intensity). However, this last configuration is not common in microscopy.

Some contrasts mechanisms like two-photon fluorescence require a very large intensity on the sample to be efficiently excited. One can then no longer use wide-field illumination to probe such contrast. In this case, a second alternative approach uses a tightly focused illumination on the sample to generate enough signal at a given point (see Fig. 1.2). In principle, there is no need for detection to exhibit high resolution, a simple bucket detector collecting the maximum amount of power without any resolution can be sufficient. To image a sample, the focus is scanned throughout the field-of-view and the emitted light is collected for each position, building the image pixel by pixel.

The performance of a microscope is above all characterized by its resolution, i.e. the minimum distance that must separate two points sources in order to distinguish them on the image (see Fig. 1.4). The ultimate resolution achievable with a standard microscope has been theorized by Ernst Abbe around 1870. A point source is imaged as a finite-size spot by the microscope. This spot, which we will refer to as the system point spread function (PSF), has a finite size due to diffraction through the lenses aperture and in general because of the imperfections of the optical system[1] (see Fig. 1.3). In the very common case of a

[1] The relevant parameter here is the apparent point size, as it would be seen with a 1:1 magnification detection.

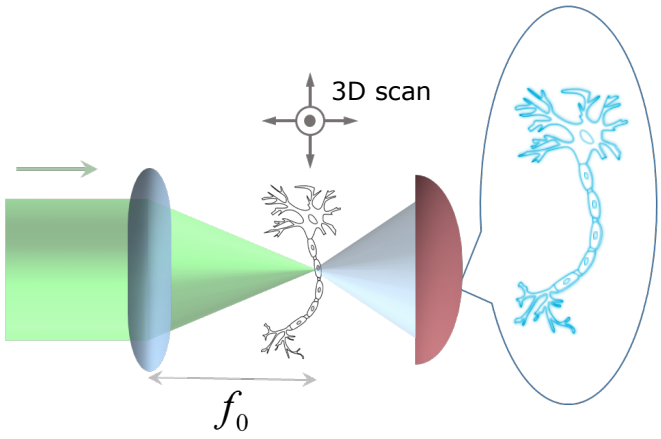

Figure 1.2 – Scanning microscopy setup. Light is focused on the sample. The emitted fluorescence is collected by a bucket detector. The focus is scanned throughout the sample to build the image.

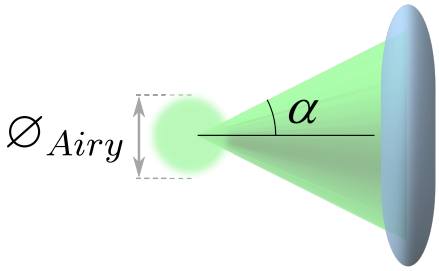

Figure 1.3 – Diffraction-limited width of a focused light spot.

circular aperture, this PSF is the so-called Airy disc, which is analytically given by the Fourier transform of the circular aperture:

$$I(r) = I_0 \frac{2J_1(\frac{\pi}{\lambda} r NA)}{\frac{\pi}{\lambda} r NA}$$

where I_0 denotes the central intensity, J_1 is the Bessel function of the first kind of order one, λ the illumination wavelength, r the radial distance to the optical axis and $NA = n\sin(\alpha)$ the numerical aperture of the imaging system, with n the refraction index of the medium in which light propagates, and α the maximum angle of collection, i.e. the angle of the wavevector with the largest transverse component that is transmitted through the lens (see Fig. 1.3).
Its width is approximately given by:

$$\varnothing_{Airy} = \frac{\lambda}{2NA} = \frac{\lambda}{2n\sin(\alpha)}$$

If we now consider focused illumination microscopy techniques, the resolution is determined by the size of the focal spot that one is able to generate on the

sample. By optical reciprocity, this size is identical to the previous diffraction limited Airy disc width. The "point sources separation" can be understood in slightly different ways, as illustrated in Fig. 1.4. Therefore several resolution criteria have been proposed over the years, nonetheless all proportional to $\varnothing_{Airy}$. Several super-resolution methods have recently been introduced to overcome (by

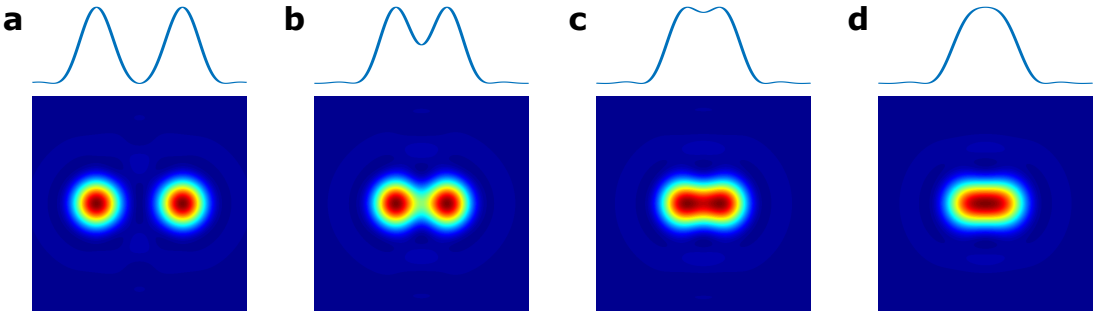

Figure 1.4 – Resolution of an optical imaging system. a) Fully resolved point sources. b) Point sources resolved according to Rayleigh's resolution criterion. c) Point sources resolved according to Sparrow's resolution criterion. d) Unresolved point sources.

far) this Airy resolution criterion, using fluorophore localization or evanescent waves for instance, but this lies beyond the scope of this thesis [Hell 94, Betzig 06, Dickson 97, Schermelleh 10].

A strong hypothesis that has been made so far is that the medium in which light propagates has a homogeneous refractive index. In such cases, simple ray or wave optics theories can be used to build the appropriate microscopy system and to predict its performances. This hypothesis inherently limits any optical imaging technique to homogeneous samples or at least to superficial layers when it comes to image biological structures inside tissue. At further depth, microscopic inhomogeneities of refractive index cause light scattering that prevent from focusing light deep inside tissue.

1.2 Introduction to light scattering

1.2.1 Light-matter interaction

When light encounters a particle, e.g. an atom, a molecule or even a simple electron, the electric field of the incident wave forces the constituting charges into an oscillatory motion. The accelerated charges emit in turn some electromagnetic radiation in all directions: this is the scattered radiation. In all following sections, we will consider only coherent elastic scattering: the incident and scattered

waves have the same wavelength and a well defined phase relation. The oscillatory motion of the electric charges can also convert the incident electromagnetic radiation through inelastic processes, either into a non-radiative form of energy (heat, vibrations,...) or via a radiative process (fluorescence). This phenomenon is called absorption and yields to a progressive decrease of the total coherent radiative energy.
Light is scattered whenever it comes upon an obstacle, and is thereby related to the heterogeneity of the medium in which it propagates. Yet everything apart from vacuum is heterogeneous in a sense: any medium is made of discrete atoms which will scatter light propagating in the medium. However, light does propagate in straight line in some medium, like water, glass or air. In a dense homogeneous medium, in which the molecular separation is smaller compared to the wavelength of the incident light, it can be shown that the scattered wave superimposes itself with the incident wave to give a refracted wave that propagates at the velocity $\frac{c}{n}$, where c is the light velocity in vacuum and n is the refractive index of the medium [Bohren 08]. Snell-Descartes laws can actually be derived using this microscopic approach. The refractive index depends on the polarisability of a single molecule and on the number of molecules per unit volume. While this number is statistically homogeneous at the scale of the wavelength, it may present significant local nanoscopic fluctuations, which may then yield a small multi-directional scattered component. This explains for instance why one may actually visualize a laser beam propagating in water (even very pure): most of the energy follows the beam direction, but a small portion is quasi-isotropically scattered and reaches the eye [Bohren 08, Morel 74].
In such a medium, geometrical optics can be used, as an overwhelmingly large portion of the beam propagates in straight line. When considering smooth fluctuations of the refractive index at large scale compared to the wavelength (tens to hundreds of micrometers), ray tracing is in principle still achievable, considering refraction laws. The fluctuations of the refractive index in this regime are called aberrations. In biological tissue however, light also encounters fluctuations of the refractive index at a scale comparable to the wavelength, and the wave nature should then be considered: the incident wave is entirely scrambled.

1.2.2 Light scattering in biological tissue

Biological structures exhibit strong heterogeneities at a whole range of different scales. Fig. 1.5 provides some spatial scales about common biological structures. This complex medium can be optically modeled with a fluctuating refractive index. In principle, light propagation can be predicted with Maxwell equations if this position-dependent refractive index is known. However, this cannot generally be solved due to the unknown extreme complexity of the structures at stake.

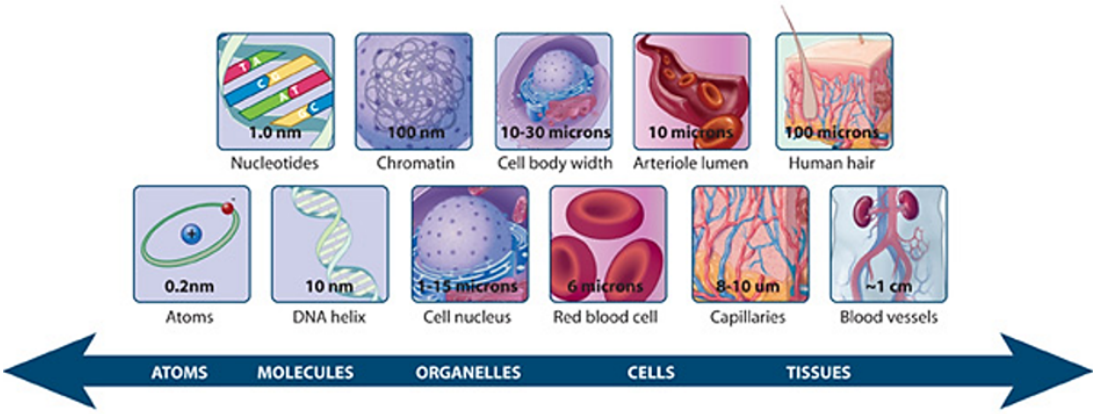

Figure 1.5 – Size scales of various biological structures. source: www.nature.com/scitable

Numerous theoretical models have been developed to rather predict mesoscopic or macroscopic quantities, such as fluence rate evolution in tissue, or reflection and transmission of light by tissue. These models usually introduce effective parameters that characterize the tissue, allowing some tabulation [Jacques 13]. We present here a widespread approach based on radiative transport theory [Cheong 90, Chandrasekhar 13]. In this framework, scattering and absorption effective coefficients of tissue can be defined, and we provide some insights about their macroscopic interpretation.

The radiative transport approach describes light propagation as the transport of a flux of photons, having a given probability to be scattered or absorbed by the medium. Light transport within such medium is modeled using the radiance of light $\mathcal{L}(\mathbf{r}, \mathbf{u})$, which represents the power (per unit surface and solid angle) carried by a monochromatic light wave propagating in the direction $\mathbf{u}$, at a given position $\mathbf{r}$. The fluence rate $d\phi(\mathbf{r}, \mathbf{u})$ propagating through a surface element $d\mathbf{S}$ centered on $\mathbf{r}$, in a solid angle $d\Omega$ centered on the direction $\mathbf{u}$ is related to the radiance by:

$$d\phi(\mathbf{r}, \mathbf{u}) = \mathcal{L}(\mathbf{r}, \mathbf{u})\mathbf{u} \cdot d\mathbf{S}d\Omega \tag{1.1}$$

$\mathcal{L}(\mathbf{r}, \mathbf{u})$ may decrease when photons are either absorbed or scattered in a different direction. It may also increase when photons are scattered from a direction $\mathbf{u}'$ to the direction $\mathbf{u}$.

The radiative transport equation transcribes this energy balance:

$$\mathbf{u} \cdot \nabla \mathcal{L}(\mathbf{r}, \mathbf{u}) = -(\mu_a + \mu_s)\mathcal{L}(\mathbf{r}, \mathbf{u}) + \mu_s \int_{4\pi} p(\mathbf{u}, \mathbf{u}')\mathcal{L}(\mathbf{r}, \mathbf{u}')d\Omega \tag{1.2}$$

where $d\Omega$ is the differential solid angle in the direction $\mathbf{u}'$, and μ_a, μ_s and $p(\mathbf{u}, \mathbf{u}')$ are parameters described thereafter.
These global parameters can be experimentally measured by considering the attenuation of the ballistic intensity of a collimated beam propagating in the tissue. This intensity can actually be related (in a non-trivial way) to the ballistic fluence rate [Ishimaru 78, Sheng 06]. We consider here only the stationary case, but time dependence can be included in this formalism.

Absorption coefficient

Photons can be absorbed by atoms and molecules of the medium to excite electronic transitions or vibrational motions. Most of these transitions relax non-radiatively, and usually most of the energy is transformed into heat. These nanoscopic phenomena can be described with the effective absorption coefficient μ_a. This average parameter characterizes the global decrease of the ballistic intensity due to absorption, accounting for potential local fluctuations of the absorption properties of the medium.
The evolution of this ballistic intensity, considering a collimated beam propagating in a solely absorbing tissue, is then given by the following equation:

$$I(z) = I_0 e^{-\mu_a z}$$

where z is the propagation length, and I_0 the initial fluence rate. This exponential decrease is known as the Beer-Lambert law. The corresponding absorption mean free path is defined by $\ell_a = \frac{1}{\mu_a}$. It can be interpreted as the average distance between two absorption events. However, this should be carefully nuanced: tissues are not similar to a collection of discrete scattering particles. This should rather be considered as a statistical interpretation: the probability dP for a photon to be absorbed over a given distance dz is proportional to I: $dP = \mu_a e^{-\mu_a z} dz$, which leads to: $\langle z \rangle = \int_0^{+\infty} z\mu_a e^{-\mu_a z} dz = \frac{1}{\mu_a} = \ell_a$. On average, a photon will then propagate over a distance ℓ_a before being absorbed.

Scattering coefficient

This coefficient describes the ballistic photons decay due to scattering by the inhomogeneities of the refractive index. The evolution of the ballistic intensity

of a collimated beam propagating in a solely scattering tissue is then given by the following equation:

$$I(z) = I_0 e^{-\mu_s z} \tag{1.3}$$

The scattering mean free path is defined as $\ell_s = \frac{1}{\mu_s}$. It can be interpreted as well as the average distance between two scattering events. In general, three scattering regimes can be considered, depending on the propagation length of light in the medium:

$L \ll \ell_s$: ballistic regime
$L \simeq \ell_s$: single scattering regime
$L \gg \ell_s$: multiple scattering regime

Extinction coefficient

Although the underlying physical phenomena are distinct, both absorption and scattering result in a decay of the ballistic intensity. As it can be challenging to discriminate the magnitude of each phenomenon, an extinction parameter driving the exponential decay due to both processes can be defined as $\mu_{ext} = \mu_a + \mu_s$. Its inverse ℓ_{ext} is called the extinction mean free path.

Phase function

Depending on the size of the scatterers, the scattering process is more or less isotropic. The previous scattering coefficient only describes the decrease of energy along the direction of the ballistic beam. The directional spreading of the total energy can be described by the phase function $p(\mathbf{u}, \mathbf{u}')$, which gives the probability for an incident photon in the direction $\mathbf{u}$ to be scattered in the direction $\mathbf{u}'$ ($\int_{4\pi} p(\mathbf{u}, \mathbf{u}') d\Omega = 1$). For biological tissue, it is usually considered that this function only depends on the angle θ between $\mathbf{u}$ and $\mathbf{u}'$, and can be well approximated by the Henyey-Greenstein phase function [Thomas 02, Jacques 87].

Anisotropy factor

The anisotropy factor g characterizes the anisotropy of the scattering process (no surprises). Under the assumption that p depends only on θ, it is mathematically defined by:

$$g = \langle \cos\theta \rangle = \langle \mathbf{u} \cdot \mathbf{u}' \rangle = \int_{4\pi} \mathbf{u} \cdot \mathbf{u}' \; p(\mathbf{u}, \mathbf{u}') d\Omega \tag{1.4}$$

For an isotropic scattering process g is equal to 0, and when the scattering is directed mostly in the forward direction g approaches 1. For biological tissue, g typically takes value between 0.8 and 1, which means that light is mostly scattered in the forward direction.

Transport mean free path

Finally, a last parameter called the transport mean free path can be defined: $\ell^* = \frac{\ell_s}{1-g}$. In the same manner as the extinction length characterizes the macroscopic decay of the ballistic light, this length describes the transport of the scattered light at the macroscopic scale. It represents the characteristic path length after which the propagating beam "looses the information" of its primary incident direction. In other words, the light propagation becomes isotropic after a few transport mean free paths (see Fig. 1.6). One considers that the multiple

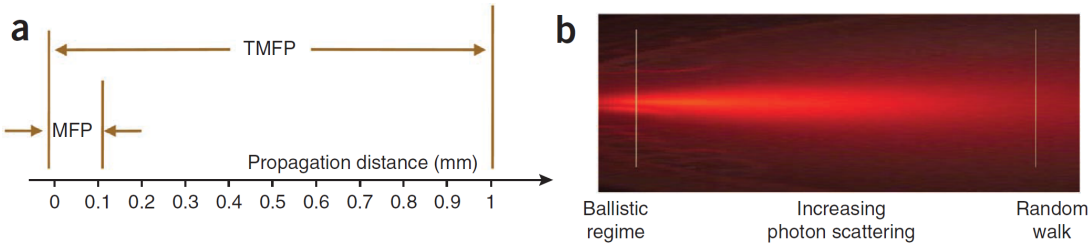

Figure 1.6 – Light scattering in complex biological media. a) Typical scattering lengths in biological tissue. b) Simulated light beam propagation inside scattering tissue. source: [Ntziachristos 10]

scattering regime starts from this propagation length. In biological tissue, the scattering mean free path is ∼100 µm, which typically leads to a transport mean free path of about 1 mm in the near infrared [Ntziachristos 10].
All the parameters described in this section can also be wavelength dependent, as illustrated for instance in Fig. 1.7 for the absorption coefficient of several endogenous biological substances.

1.3 Optical imaging in biological tissue

After 1 mm in biological tissue, i.e. a few scattering mean free paths or one transport mean free path, the light propagation is becoming more and more isotropic, and there is no ballistic component left. This highly limits the optical imaging ability of simple systems at depth (as described in section 1.1),

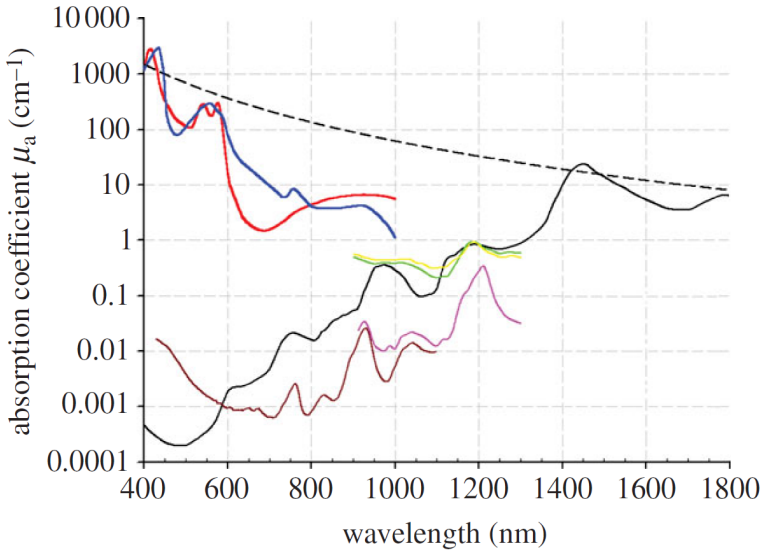

Figure 1.7 – Wavelength dependence of optical absorption coefficients. red: oxy-hemoglobin (150 g.L^{-1}), blue: deoxy-hemoglobin (150 g.L^{-1}), black plain line: water, brown and pink: lipids, black dotted line: melanin, green: collagen, yellow: elastin. source: [Beard 11]

as they rely on this ballistic light. This transport mean free path represents a first limit for high resolution optical imaging (sometimes referred to as the soft limit [Wang 09]): scattering usually prevails over absorption in tissue, so that the light intensity is not so strongly absorbed at this depth. Resolution is thus degraded, but photons are still reaching this depth. The second limit (so-called hard limit) corresponds to the maximum depth that can be reached by the scattered photons before being all absorbed. This depth is of the order of 6 cm and is the very limit of non-invasive optical imaging in biological tissue [Wang 09]. Beyond, the last resort is endoscopy: light is delivered and collected in an invasive way, using optical fibers inserted inside the tissue. Fiber bundles have been used for many years [Hopkins 54, Santos 09] and are now widely employed for imaging purposes, for instance in neuronal imaging [Szabo 14]. Multimode fibers have also been extensively investigated in the past few years, potentially enabling to reduce the endoscope size [Choi 12, Cizmar 12, Papadopoulos 12, Simandoux 15b, Sivankutty 15].

In this section, we present some non-invasive techniques widely used in biology to image structures embedded in scattering tissue, at depth ranging from l_s to a few l^*. This obviously does not constitute an exhaustive list. The goal is to exhibit the diversity of available techniques, and in particular to present both passive (ballistic component filtering) and active (wavefront correction) methods.

1.3.1 Imaging with ballistic photons

One straightforward strategy to image structures embedded in tissue is to isolate the ballistic photons, since they behave as in free space. One can thus use the same ray optics concepts and benefit from optimal resolution. The limitation is the amount of signal available for detection, which decreases exponentially with depth.

Confocal Microscopy

In a typical fluorescence microscope, the sample is illuminated using either wide-field or focused illumination, and the image is build by collecting the total emitted fluorescence. However, due to scattering, a non-negligible portion of this fluorescence signal does not originate from the imaging focus but from other locations inside the tissue. This background fluorescence reduces the image contrast. The key idea of confocal microscopy is to filter out this background by adding a pinhole before the detector in the confocal plane of the objective (see Fig. 1.8) [Minsky 88, Wilson 11].

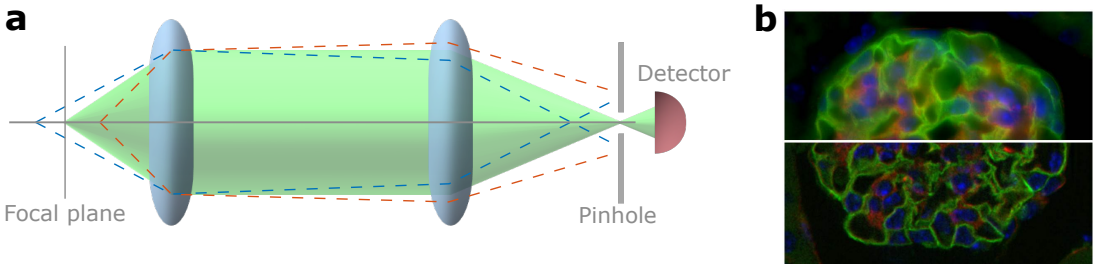

Figure 1.8 – Confocal microscopy. a) Schematic of the setup: only light originating from the focal plane can reach the detector (plain green beam), the remaining light coming from shifted planes is blocked by the pinhole (dotted red and blue lines). b) Comparison between standard wide-field microscopy image (top) and confocal microscopy image (bottom) of a fixed 15 µm thick kidney slice. source: microscopysolutions.ca

Multi-photon fluorescence microscopy

This technique also aims at suppressing the diffuse fluorescent background. It uses non-linear two-photon absorption to favour fluorescence generation in a very tight focal region [Denk 90, Helmchen 05].
The non-linear process enables to generate fluorescence only in regions of very

high intensity: the fluorescent light intensity varies proportionally to the squared pump intensity. It is also sensitive to the temporal profile of the excitation pulse: it thus prevents scattered photons to generate undesired background fluorescence, because the scattered pulse is temporally broadened [McCabe 11] (see Fig. 1.9.a,b). This technique is eventually limited by the background emitted at the surface of the sample, where the excitation pulse is short enough to excite fluorescence. Imaging depths of the order of the millimeter have been demonstrated (see Fig. 1.9.c) [Kobat 11]. This method can also be extended to higher order non-linearities, for instance using three-photon fluorescence [Horton 13].

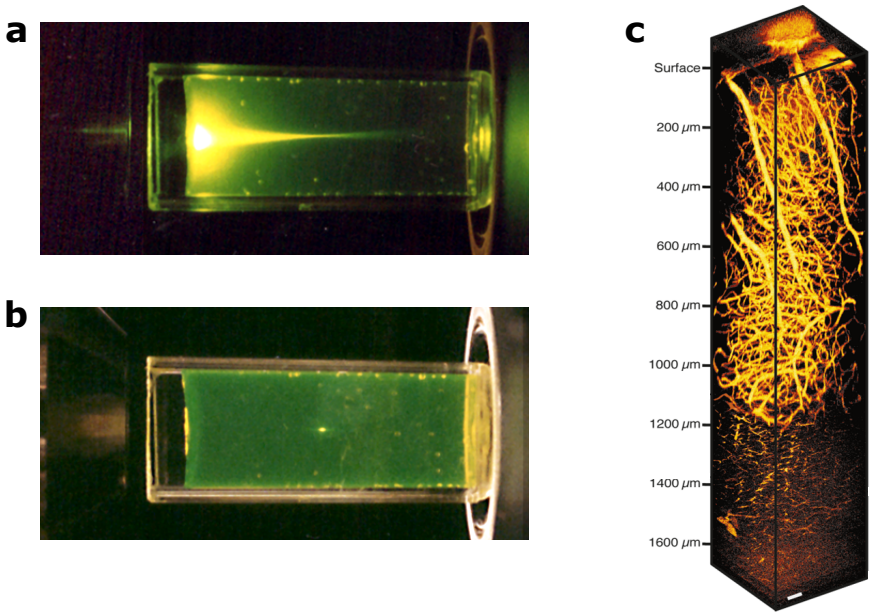

Figure 1.9 – Two-photon microscopy. a) Single-photon fluorescence generation: a strong fluorescence background is generated by the diffusive halo. b) Two-photon fluorescence generation: fluorescence is generated only at the focus of the objective. c) In vivo two-photon fluorescence images of cortical vasculature in mouse brain. The laser power and the integration time are adjusted at each depth to provide comparable fluorescence intensities. source: a,b: Webb Lab, Cornell University; c: [Kobat 11]

Confocal and multi-photon microscopy both use spatial filtering to select only the ballistic photons to build an image. Different kinds of filtering exist. Temporal filtering relies on the fact that photons emerging early from of the scattering sample (in transmission) are least scattered. By adding a temporal detection, it is possible to select only ballistic or least scattered photons [Schweiger 99]. However, the electronic can be very costly for multi-pixel temporally-resolved fast detection.
Another filtering criterion is the temporal coherence. A successful illustration of this concept is the optical coherence tomography (OCT) [Huang 91, Dubois 04].

The experimental setup is based on a simple Michelson interferometer, with one mirror replaced by the sample of interest. The axial resolution is provided by the coherence length of the illumination source, which can be made very short using for instance white light. In the particular case of full-field OCT, the interference signal is generated on the camera only by light paths of similar lengths along the two arms of the interferometer. This enables to virtually section the sample. By shifting the reference mirror, the image plane is axially scanned. This technique is however very limited because it selects photons that are only back-scattered once. The signal thus strongly decreases at depth.

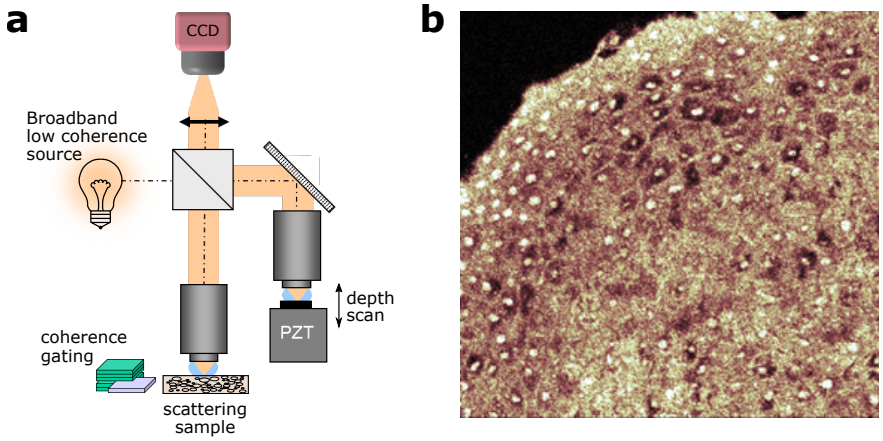

Figure 1.10 – Optical coherence tomography. a) Full-field optical coherence tomography setup. b) En-face OCT image of a fixed human esophagus epithelium, recorded at an average depth of 100 µm below the sample surface. source: [Dubois 04]

Adaptive optics

In the weak scattering regime, light can still be focused if a strong ballistic component persists. However, large scale fluctuations of the refractive index (compared to the operating wavelength) can still deviate and scramble this focus. These fluctuations induce a distortion of the wavefront, called aberrations, both on the illumination and detection paths. If known, these aberrations can be corrected using deformable mirrors.
This technique has been first developed for astronomical observations, where fluctuations of the atmosphere density, and hence of the refractive index, also distorts images [Babcock 53, Roddier 99]. One has first to measure the aberrations using a guide star and a wavefront sensor: the guide star acts as a point source and the emitted wavefront is measured after propagation in the aberrating medium (see Fig. 1.11). The phase conjugate of this wavefront is then displayed on a deformable mirror in order to retrieve a planar wavefront before the imag-

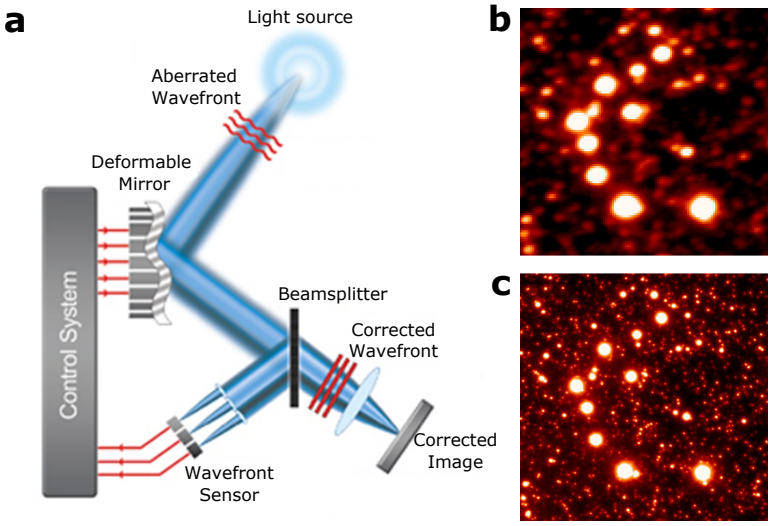

Figure 1.11 – Adaptive optics for astronomy. a) Principle: the incident aberrated wavefront is measured, the adapted correction is displayed with a deformable mirror, the corrected image is finally measured on the detector. b) Uncorrected image (region nearby the center of the globular cluster Omega Centauri). c) Corrected image. source: a: bostonmicromachines.com; b,c: [Marchetti 07]

ing telescope. Two main types of guide star can be used. One can first use an actual star located nearby the region to be imaged. When there is no bright enough real star to use for wavefront measurement, laser-induced artificial guide stars can alternatively be used. A laser is shot toward the upper layers of the atmosphere to create a point source, either by exciting sodium fluorescence, or by being simply back-scattered by the atmosphere.
In microscopy as well, the key point is to find the appropriate beacon to measure the aberrations [Booth 14]. A first straightforward technique is to use a small point-like emitter embedded in the tissue nearby the location to image. It is usually performed by implanting this emitter, which compromises the non-invasiveness of the process [Vermeulen 11]. A second technique is to generate an artificial guide star by using two-photon fluorescence. The light used to measure the aberrations is then the fluorescence generated at the focus [Aviles-Espinosa 11]. A third and more indirect method can also be implemented. In this procedure, one assesses the aberrations by maximizing some metric, related to the total fluorescence intensity or the image sharpness [Debarre 07]. The aberrations are guessed by trying different combinations of basic aberrations (usually decomposed on the Zernike polynomials basis). It should be noted that aberrations are also present in the optical elements themselves, and can be compensated for with the same process. Simulated typical phase aberrations and the corresponding aberrated focal spots are presented in Fig. 1.13. These aberrations can usually be decomposed as a linear combinations of basic aberrations, or modes.

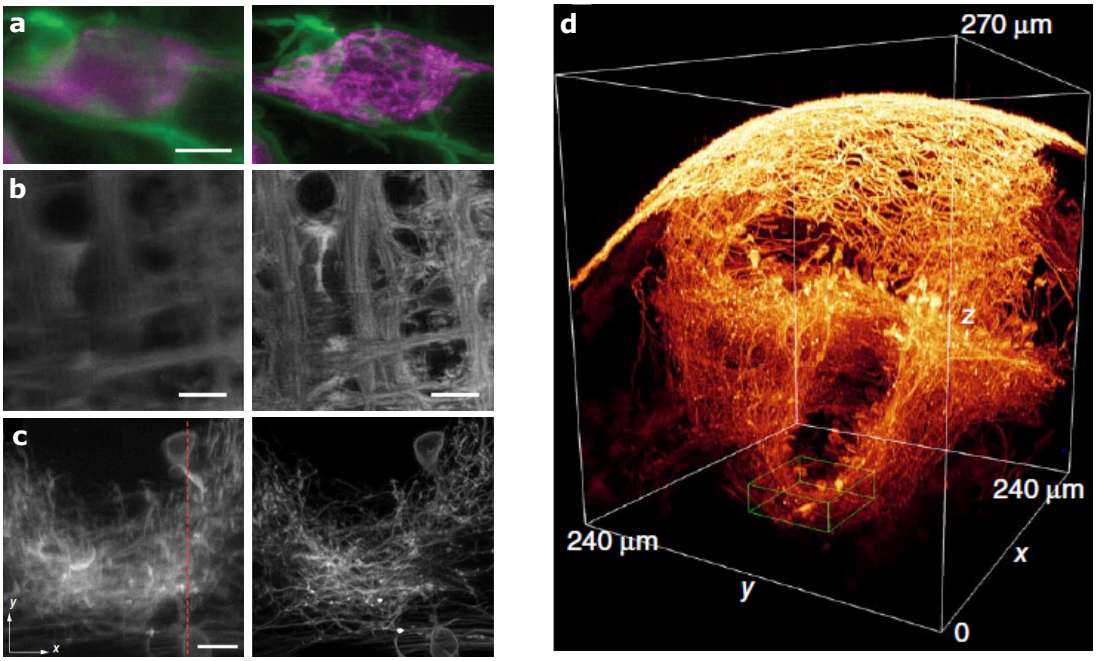

Figure 1.12 – Adaptive optics for microscopy. In a,b,c the left image is obtained without adaptive optics (AO), the right one with AO. a) Confocal image of mitochondria (magenta) and plasma membrane (green) of a cell ∼150 µm deep in the zebrafish hindbrain. Scale bar: 5 µm. b) Two-photon fluorescence image of a small region in the zebrafish brain. Scale bar: 10 µm. c) Two-photon fluorescence image of a small region in the living zebrafish brain, corresponding to the green box in d. Scale bar: 10 µm. d) 3D two-photon fluorescence image of a large portion of living zebrafish brain, with AO correction. source: [Wang 14a]

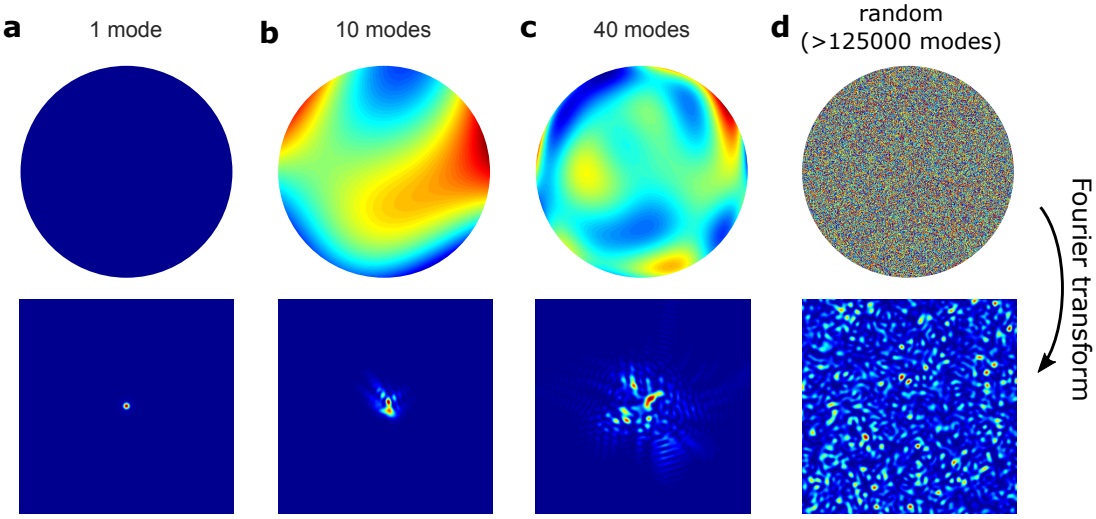

Figure 1.13 – Typical phase aberrations described as a linear combination of the first N Zernike polynomials (top row) and corresponding aberrated focal spot (bottom row) (simulations). a) N=1 mode (no aberration): perfect focusing is possible without phase correction. b) N=10 modes, c) N=40 modes: perfect correction is possible when controlling only a limited number of modes. d) N larger than 100000 modes: no perfect correction is possible here when controlling only a limited (<100) number of modes. The focal spots are obtained by computing the squared amplitude of the Fourier transform of the phase masks.

The number of actuators of the deformable mirror required to perform the wavefront correction is approximately given by this number of modes. This approach is no longer possible deep inside tissue, where light is strongly scattered and that no significant ballistic fraction of the incident beam survives.

1.3.2 Imaging without ballistic photons: Diffuse optical tomography

At larger depth, beyond the transport mean free path, light is almost entirely scattered:

$$\frac{I_{ballistic}(z = l^*)}{I_0} = e^{-l^*/l_s} = e^{-1/(1-g)} \simeq e^{-10} \simeq 4.5 \cdot 10^{-5}$$

in the ideal case of non-absorbing biological tissue. To perform imaging significantly beyond this depth, one has to extract information from photons that followed very different and very tortuous paths. Diffuse Optical Tomography (DOT) achieves such task using fluence measurements from an array of detectors that collect light emitted by an array of light sources (see Fig. 1.14). Using

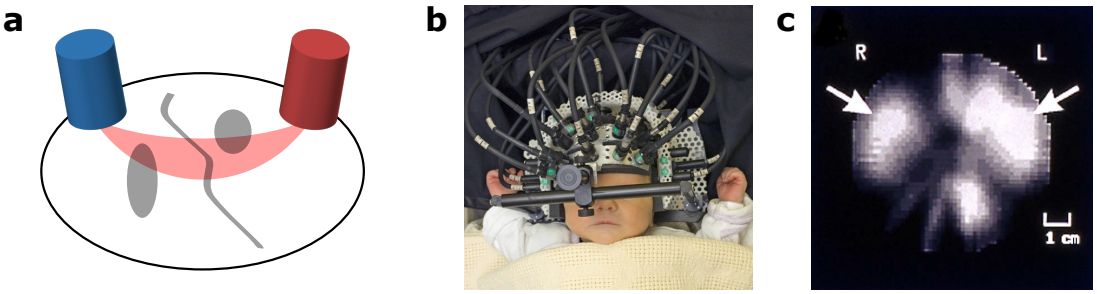

Figure 1.14 – Diffuse Optical Tomography. a) Principle of DOT: a source (blue) sends light deep inside a complex medium, a detector (red) measures a fraction of the scattered light that travels through a typical "banana" shaped region (light red). Measurement correlations along with modeling of photons transport are then used to retrieve the scattering and absorption properties of the medium. b) Typical clinical setup. c) Infant brain image obtained with DOT. source: [Hebden 07]

these measurements along with a forward model of photon transport inside complex medium, it is possible to retrieve scattering and absorption information of tissue [Boas 01]. However, this technique suffers from a very poor resolution, that can be shown to be of the order of the probed depth (usually a few centimeters).
Therefore, it seems impossible to provide high resolution images using only scattered photons, as the relevant information is scrambled during the complex light propagation. It would be appealing to control these photons in the same manner

as weakly scattered photons are controlled in adaptive optics techniques. However, a quick calculation of the number of optical modes required to perform such correction at depth equal to the transport mean free path shows that one would need millions of actuators:

$$N_{modes} \sim \left(\frac{L}{\lambda}\right)^2 \simeq 10^6$$

where L is the size of the illuminated area at the output of the scattering sample (approximately equal to its thickness, of the order of 1 mm) and λ the operating wavelength (about 1 µm). This humongous number exceeds by far the number of correction modes involved in standard adaptive optics, which is usually less than 100 to perform a nearly perfect correction. This task has thus been overlooked, until the idea emerged that one actually does not need a perfect correction at all for focusing purpose.

1.4 Focusing light through strongly scattering medium

In 2007, Vellekoop and Mosk performed the first wavefront shaping experiment through multiply scattering media [Vellekoop 07]. They demonstrated that coherent light can be focused through a highly scattering opaque paint layer by controlling only the incident wavefront. By iteratively optimizing this wavefront, they were able to enhance light intensity at a desired target location behind the scattering layer. This now considered eye-opening experiment has aroused a lot of interest and many applications have been developed around this new concept [Mosk 12]. In this section, we provide a brief introduction to speckle, and describe this iterative optimization experiment. We then describe the transmission matrix approach, which essentially characterizes the mode mixing in the complex medium due to scattering.

1.4.1 Coherent light propagation in scattering media

We briefly describe here the propagation of spatially coherent monochromatic light through a scattering layer. The medium is assumed to be linear: the incoming and outgoing fields are linearly related. When traveling in such a medium, light follows very tortuous paths, introducing a complex distribution of phase retardation. The resulting interference pattern at the output of the medium, the so-called speckle pattern, is a complex though deterministic figure (see Fig. 1.15.b). The intensity fluctuates spatially, with an exponential proba-

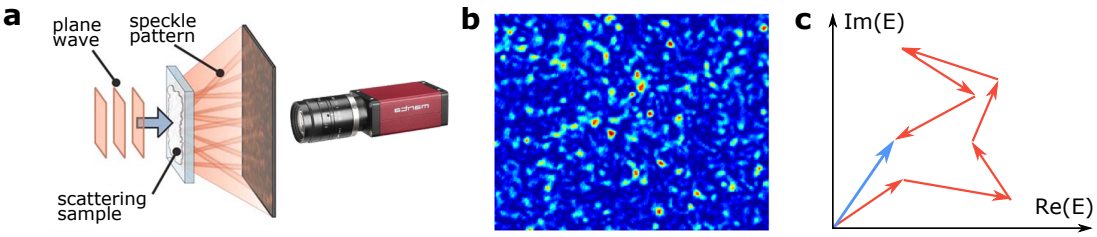

Figure 1.15 – Speckle. a) Light propagates through a strongly scattering sample, a camera measures the scattered light intensity at one given plane behind the sample. b) Typical interference speckle pattern obtained with the previous simple experimental setup. c) Simplified Fresnel representation of the resulting electric field at one single pixel of the camera. source a: [Vellekoop 07]

bility distribution. This pattern presents an irregularly arranged juxtaposition of small "grains", whose size depends on the experimental configuration (see appendix B). A speckle grain is brighter when the interferences tend to be slightly more constructive than the average at its location. Throughout this manuscript, we will always consider fully developed speckles, which means that the phases of the different contributions that followed different paths are uniformly distributed between 0 and 2π. The complex interferences are usually modeled as the sum of randomly distributed phasors (as shown in Fig. 1.15.c) [Goodman 07]. This approach uses the Fresnel representation of the resulting output electric field as the superposition of complex elementary components. At one given point, the resulting electromagnetic amplitude is then related to the modulus of the phasors sum. This sum of phasors can be modeled by a random walk in the complex plane, because of the apparent randomness of the output phase distribution, due to the complex arrangement of scattering particles.
Nevertheless, these complex random interferences are deterministic. They can thus be coherently manipulated and exploited for focusing and imaging by controlling the input wavefront. To focus light at a target point, one would have to line up these phasors along the same direction, i.e. to add a specific phase to each input component of the beam.

1.4.2 Light focusing via iterative optimization

In this section, we describe the seminal experiment of Vellekoop and Mosk [Vellekoop 07]. The basic idea is to find the optimal wavefront to send through the scattering medium in order to enhance the light intensity at a target point located behind. Similarly to adaptive optics, the phase of the incident beam can be precisely controlled using a Spatial Light Modulator (SLM). This SLM is an array of pixels that can locally shift the phase of the impinging beam (either in transmission or in reflection). Liquid crystals based SLM and piston-like

micro-mirrors are the two main technologies. However, the correction cannot be perfect now because the number of controllable input modes (SLM pixels) is very small compared to the number of output modes (speckle grains). Nonetheless, we shall see that light can still be focused. The experimental setup is illustrated in Fig. 1.16. The SLM shapes the incident beam wavefront, the beam then propagates through a complex scattering medium (e.g. white paint made of silica beads, 10 to 100 nm in diameter), and the output intensity in one plane behind the medium is measured with a camera.

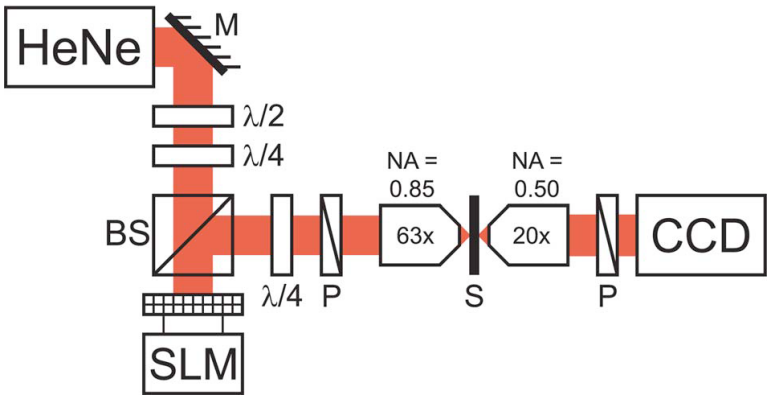

Figure 1.16 – Light focusing via iterative optimization: experimental setup. The laser beam wavefront is shaped by an SLM. Polarization optics select a phase modulation mode, as required when using a liquid crystal SLM. The SLM is imaged onto the entrance pupil of the objective (lens not shown). The shaped wavefront is focused on the strongly scattering sample (S), and a CCD camera images the transmitted intensity pattern along one single polarization. $\lambda/4$, quarter-wave plate; $\lambda/2$, half-wave plate; M, mirror; BS, 50% non-polarizing beam splitter; P, polarizer. source: [Vellekoop 07]

To focus light on one target location (usually one pixel of the CCD camera), the optimization process iterates this step for each input mode:

- the phase of the input mode is swept between 0 and 2π in a finite number of steps (see Fig. 1.17.b,d), resulting in a sinusoidal modulation of the intensity at the target CCD pixel (see Fig. 1.17.c).
- the phase of the input mode is set as to maximize the intensity.

This step is then repeated for every input mode, gradually building the focus at the desired location (see Fig. 1.17.e-h). The procedure described above uses the canonical basis of the SLM: one SLM pixel corresponds to one input mode. We can consider different input bases, that mainly influence the robustness of the optimization in noisy environments and the convergence of the optimization procedure. The intensity modulation caused by the phase modulation of a single

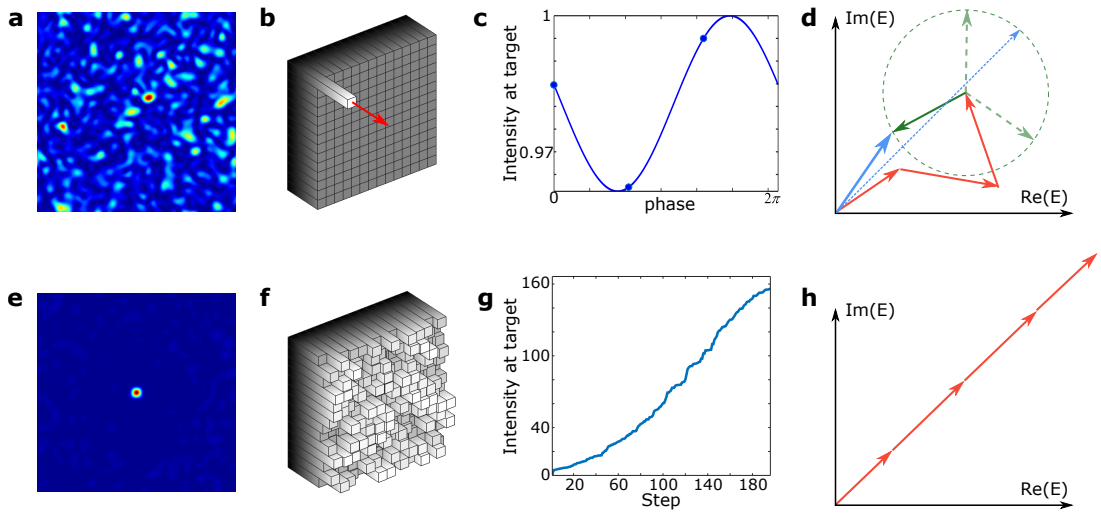

Figure 1.17 – Light focusing via iterative optimization (simulations). a) Initial speckle pattern. b) The phase of one SLM pixel is swept between 0 and 2π. c) Intensity of the central camera pixel as a function of the SLM pixel phase (circles: measurements, line: sine fit). d) Fresnel representation of the electric field at the target location. For simplification we represented only the contributions of 4 pixels of the SLM. orange arrows: fixed SLM pixels, green arrow: phase-shifted pixel, plain blue arrow: total field of the optimized speckle grain, dotted blue arrow: total field at the end of the current step of the optimization. e) Final speckle pattern. f) Corresponding input phase pattern displayed on the SLM. g) Evolution of the feedback intensity during the optimization. h) Fresnel representation of the electric field of the optimized grain at the end of the full optimization.

SLM pixel is indeed very faint. In a noisy experimental environment, it can be hardly detectable if the modulation depth is of the same order of magnitude than the inherent noisy signal fluctuations. It is then favorable to simultaneously modulate the phase of several SLM pixels at each step [Vellekoop 08a].
To quantify the efficiency of the focusing process, the intensity enhancement factor η is defined as the ratio between the final peak intensity at the target location and the average intensity of the background speckle[2]. When optimizing the intensity of a single speckle grain, this enhancement has been shown to be [Vellekoop 07]:

$$\eta = 0.5 \cdot N_{SLM} \quad \text{when } N_{SLM} \gg 1 \tag{1.5}$$

where N_{SLM} is the number of SLM pixels.

[2] The background speckle intensity is indeed equal to the average intensity of the initial speckle when the total number of speckle grains is very large. Let N be the total number of speckle grains and I the average intensity per speckle grain. The total average intensity is therefore NI. If the intensity of the target speckle grain is equal to $100I$ after focusing, it means that the total average intensity of the background is $NI - 100I \sim NI$ if N is large enough.

In adaptive optics, the correction quantification often uses the so-called Strehl ratio. This number is defined as the ratio between the peak intensity obtained with the corrected though aberrated setup and the peak intensity that would be obtained with a perfect unaberrated setup. This Strehl ratio approaches 1 when the correction is nearly perfect [Kubby 13]. It can also be interpreted as the ratio between the number of corrected modes and the total number of output modes (i.e. the modes that describe the aberrated wavefront, Zernike polynomials for instance). In adaptive optics experiments, typical Strehl ratios are of the order of 0.1. When dealing with multiple scattering, the number of output modes easily approaches the million and the number of SLM pixels is of the order of 100-1000, which leads to Strehl ratios around 10^{-3}. This somehow explains why adaptive optics in this regime has been overlooked for a long time. However, very imperfect correction does not mean that focusing is impossible, it only implies a finite contrast.

1.4.3 Transmission matrix approach

If one wish to focus elsewhere, the full optimization has to be carried out once again. Specifically for scanning purpose, one must run the optimization procedure for each point, which can be very time consuming. As the camera measure the intensity modulation at any point within the field-of-view, a lot of information is lost as only one single pixel intensity is used in the previous experimental scheme. Therefore it can be preferable to use the transmission matrix approach. As only linear propagation is considered here, all the measured information can then be gathered in one matrix which encodes the influence of every SLM pixels on any camera pixel. This matrix linearly links the input field (at the SLM plane) to the output field (at the imaging plane of the camera) , and can be related to the Green function of the scattering medium. This approach has been pioneered in Sylvain Gigan's group, building both on Mosk's experiment and on previous works on acoustics carried out at the Institut Langevin. The optical transmission matrix of a scattering sample has been measured first measured by Popoff and colleagues in [Popoff 10b]. In essence, this matrix predicts how the scattering medium transmits the electromagnetic field of each input mode, by spreading the energy over several output modes.
Mathematically, this relationship is given by the complex-valued optical transmission matrix T with elements $t_{mn} = |t_{mn}|e^{i\phi_{mn}}$:

$$E^{out} = TE^{in} \tag{1.6}$$

where E^{in} is the optical field on the SLM, and E^{out} the field in one given output plane, which is imaged with a camera (see Fig. 1.18).

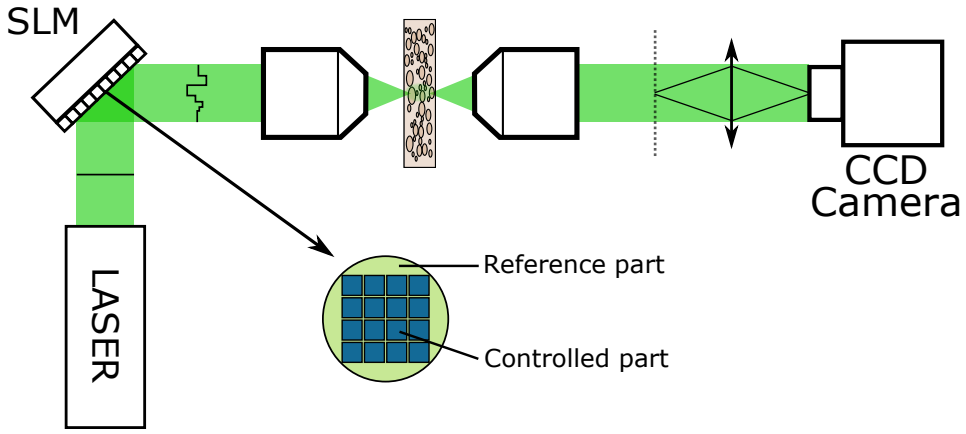

Figure 1.18 – Optical transmission matrix: experimental setup. The wavefront of a monochromatic laser is shaped by an SLM. Light then propagates through a scattering medium, and the output field is imaged on a CCD camera. An unmodulated portion of the beam wavefront is used here as a co-propagating reference arm.

For each camera m^{th} pixel ($m = 1...M$) measuring the output optical field, it equivalently reads:

$$E_m^{out} = \sum_{n=1}^{N_{SLM}} t_{mn} E_n^{in} \tag{1.7}$$

where N_{SLM} is the number of controlled SLM pixels and M the number of pixels of the camera used to measure the output optical field.
The ideal way to measure this matrix would then be to sequentially measure the speckle field generated by each SLM pixel. However, the SLM is only controlling the phase of the pixels, so their intensity cannot be switched off. Therefore, a different input basis that confers non-zero intensities to every pixels must be used for the matrix measurement. The Hadamard basis fulfills this condition: the vectors of this basis attribute equal intensity to each SLM pixel, and the orthogonality resides in the π phase shift applied to half of the pixels (see Fig. 1.19). It will be the basis of choice for our experiments.

As the camera is only sensitive to intensity, the field measurement should be performed using interferometry. The standard technique is to use an external reference arm by splitting the beam before the scattering medium. Alternatively, some unmodulated part of the beam reflected by the SLM can be used as the reference beam, thus avoiding instability issues (see Fig. 1.18). This reference will be denoted by E^{ref} in the following equations. The measurement setup is similar to the one introduced in the previous section (Fig.1.16).

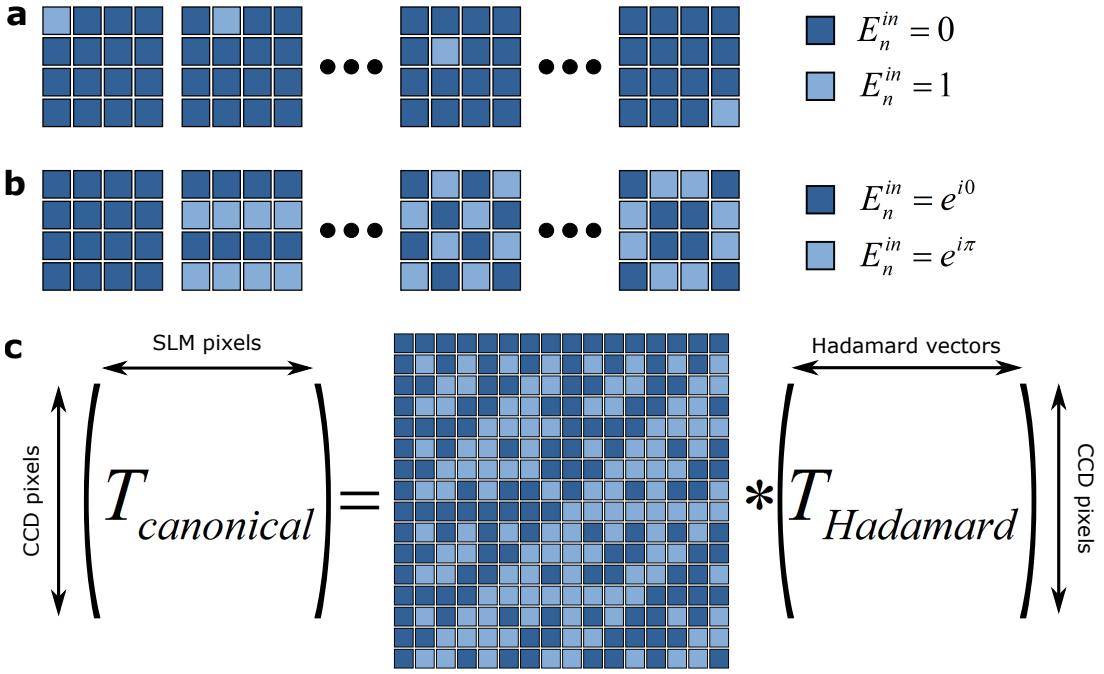

Figure 1.19 – SLM bases for transmission matrix measurement. a) Canonical basis: the SLM pixels are switched on and off in turns. b) Hadamard basis: half of the SLM pixels are π phase-shifted (except for first vector).c) Once measured in the Hadamard matrix, a simple change of basis allows to retrieve the transmission matrix in the SLM pixels basis.

The output electric field on the m^{th} camera pixel writes:

$$E_m^{out} = E_m^{ref} + \sum_{n'=1}^{N_{SLM}} t_{mn'} E_{n'}^{in} \tag{1.8}$$

where we now decompose the E^{in} input field over the Hadamard vectors. This enables to measure the matrix by "switching on" the n^{th} input mode at a time: $E_{n'}^{in} = \delta_{n,n'} |E_{n,0}^{in}| e^{i\phi^{SLM}}$, where ϕ^{SLM} an additional phase shift imposed by the SLM and $E_{n,0}^{in} = |E_{n,0}^{in}|$ is the field impinging on the SLM, assumed here to be a plane wave. The matrix is measured by successively sweeping the phase ϕ^{SLM} of each of these input modes between 0 and 2π. This leads to a sinusoidal modulation of the intensity of each m^{th} camera pixel (as shown in Fig. 1.17.c) when phase shifting the n^{th} input mode:

$$\begin{aligned} I_{mn}(\phi^{SLM}) &= |E_m^{out}|^2 \\ &= |E_m^{ref}|^2 + \left|t_{mn} E_{n,0}^{in}\right|^2 + 2\,\mathrm{Re}(|E_m^{ref}| e^{-i\phi_m^{ref}} |t_{mn}| e^{i\phi_{mn}} |E_{n,0}^{in}| e^{i\phi^{SLM}}) \\ &= |E_m^{ref}|^2 + \left|t_{mn} E_{n,0}^{in}\right|^2 + 2|E_m^{ref} t_{mn} E_{n,0}^{in}| \cos(-\phi_m^{ref} + \phi_{mn} + \phi^{SLM}) \end{aligned} \tag{1.9}$$

The phases and amplitudes of these modulations are then extracted to build the matrix. It should be noted that the transmission matrix is measured with respect

to the static reference speckle field. This reference can be partially filtered out when required, for instance to quantify statistical properties of the transmission matrix [Popoff 10b]. However, it does not impede focusing applications.
In [Popoff 10b] (among others), the matrix is measured in Fourier space: each pixel (SLM or CCD) is conjugated to a given wave vector (input or output respectively). The reason here is that plane wave are eigenmodes of free space propagation: the matrix will be diagonal if vacuum replaces the scattering layer. To focus light using this matrix, one has to invert Eq. 1.6 to compute the right

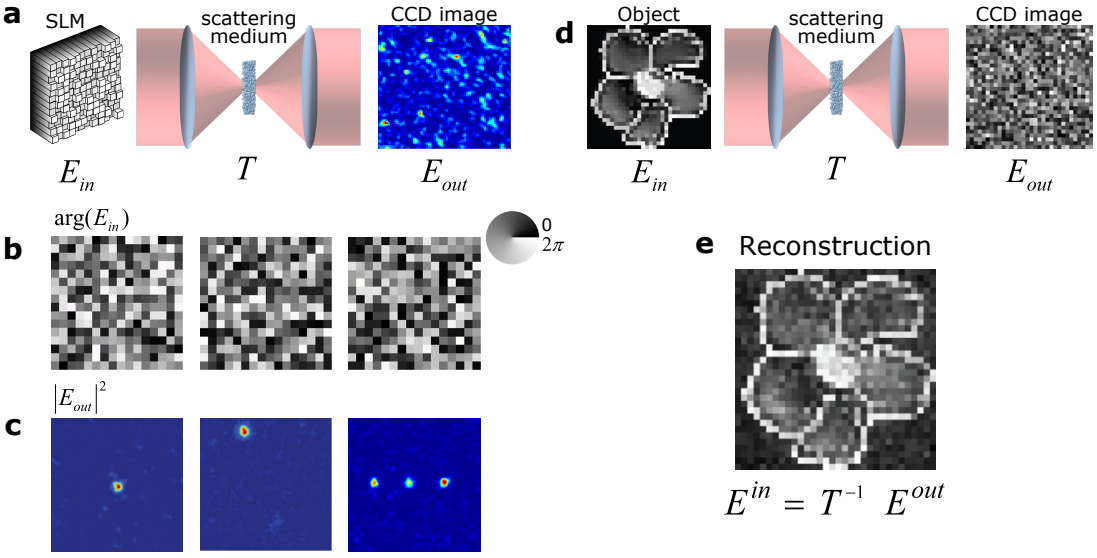

Figure 1.20 – Transmission matrix. a) Simplified schematic of the experimental setup. Input and output electric fields are linked by: $E^{out} = TE^{in}$. b) Focusing phase masks. c) Camera images when focusing patterns in (b) are displayed on the SLM. d) An object is displayed on the SLM, the resulting speckle pattern is recorded on the camera. e) The object is recovered by inverting (in a non-trivial way) the transmission matrix. source: [Popoff 10b, Popoff 10a]

input field E_{in} to send in the medium in order to obtain a target output field E_{out}^{target}. The strict inverse matrix would be plagued by experimental noise, and it has been shown that phase conjugation is the effective way to focus light using this matrix (see Fig. 1.20.a-c) [Prada 94]. This matrix can also be used for imaging purposes, as shown in figure (see Fig. 1.20.d,e). These works highlighted that light focusing and imaging could be performed through highly scattering samples, by characterizing and manipulating multiply scattered light.

The information contained in the transmission matrix is relevant for a given microscopic configuration of the scattering sample. In biological tissue though, fluid flows, heart beats, breathing or brownian motion result in speckle decorrelation. For imaging purpose in biological tissue, one should then be able to measure the transmission matrix before this decorrelation occurs. Fast characterization

techniques have thus been developed, using for instance digital micromirrors devices (DMD) [Conkey 12b]. In this approach, the transmission matrix is partially measured, as DMDs can only apply a binary control of the amplitude of the incident wavefront. Phase control could still be performed with such device using Lee holography [Lee 79] or a recently demonstrated superpixel-based method [Goorden 14]. Micromechanical systems (MEMS) could alternatively be used [Stockbridge 12], and scanning galvanometric mirrors have also been considered to measure the transmission matrix in multimode fibers [Choi 12].

1.4.4 Attempts to focus light inside scattering media

However, these techniques cannot be used to imaged directly inside tissue, as they requires a direct measurement of the speckle intensity at the target location. To probe the light intensity at depth, one must use some other indirect feedback mechanism [Horstmeyer 15]. We briefly review here several internal beacons that have been proposed in the past few years.

All-optical guide stars

Fluorescence optimization

In [Vellekoop 08c], Vellekoop and colleagues proposed to use fluorescent emitters embedded in a scattering white paint layer. By optimizing the total outgoing fluorescence, they have been able to concentrate light on these emitters (see Fig. 1.21). However this technique cannot be used for practical imaging application because the intensity will be approximately evenly distributed over all emitters. Therefore it does not guarantee any tight focusing deep inside the scattering sample (see Fig. 1.21.d), except in the case of a single small beacon.
To overcome this limitation, Katz and colleagues proposed to rather optimize a non-linear fluorescence signal [Katz 11, Katz 14]. This enables to constrain the focusing on one single speckle grain (see Fig. 1.21.g), although its position cannot be neither chosen nor known. However, this was only demonstrated through and not inside the scattering sample. Moreover, simulations in [Katz 14] suggest that only optimization of three-photon fluorescence would lead to tight focusing inside the scattering sample.
Besides, the fluorescent emitters cannot be repositioned at will, limiting any application requiring a scan of the focus. In specific conditions though, the focus can be stirred within the limited so-called memory effect range [Vellekoop 10b]. This concept will be further developed in the second chapter of this thesis.

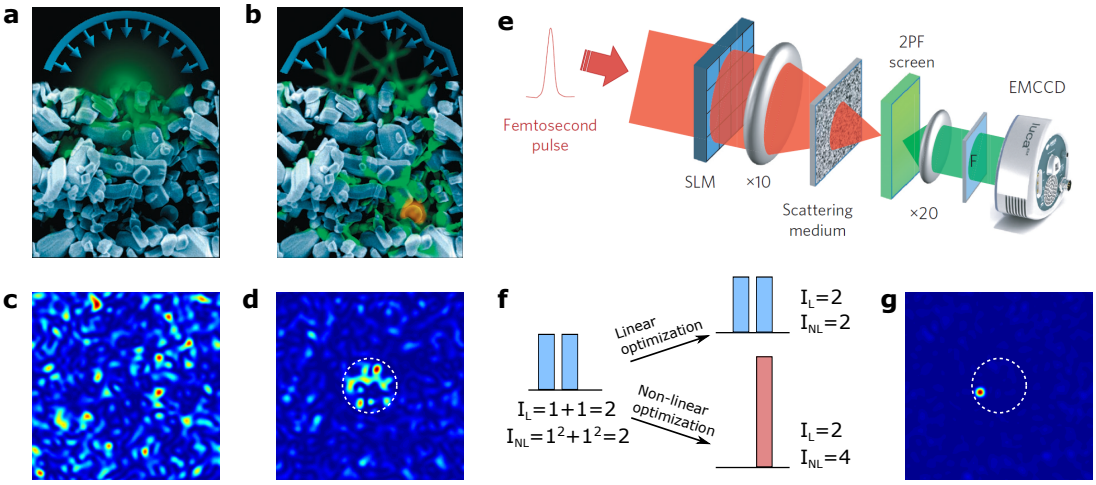

Figure 1.21 – Fluorescence feedback. a) Artist sketch of the experiment: uncorrected wavefront generate a diffusive halo in the scattering medium, in which is embedded a fluorescent bead. b) Result of the optimization of the fluorescence: light is focused on the fluorescent emitter. c) Speckle pattern in the transverse plane containing the bead before optimization (simulations). d) Final speckle pattern: the emitter is delimited by the dotted white line. If this bead is larger than the speckle grain width, several grains will be simultaneously enhanced (simulations). e) Experimental setup for two-photon fluorescence optimization. The fluorescence signal can be measured either in transmission or in reflection. f) Principle of non-linear signal optimization: the non-linear signal is maximized when light is focused in one speckle grain, whereas it makes no difference for a linear signal if the intensity is spread over several speckle grains or focused in one single grain. g) Resulting speckle pattern after optimization of the non-linear fluorescence: light is focused one single speckle grain (simulations). source: a,c: [Gerstner 08]; e: [Katz 11]

Second harmonic generation and phase conjugation

Another attempt to focus light inside scattering sample is to use second harmonic generation (SHG) from particles embedded inside the sample. The approach developed by Hsieh and colleagues is actually not based on iterative wavefront shaping, but rather on phase conjugation (see Fig. 1.22) [Yaqoob 08, Hsieh 10a, Hsieh 10b]. After measuring the outgoing wavefront of the second harmonic signal generated by the nanoparticles, they conjugate its phase with an SLM and send it back into the medium. By optical reciprocity, light is then refocused onto the particles (see Fig. 1.22). Optical phase conjugation has the additional advantage of using the full resolution of the SLM without requiring more measurement steps, as it would be the case using optimization or transmission matrix-based focusing techniques.

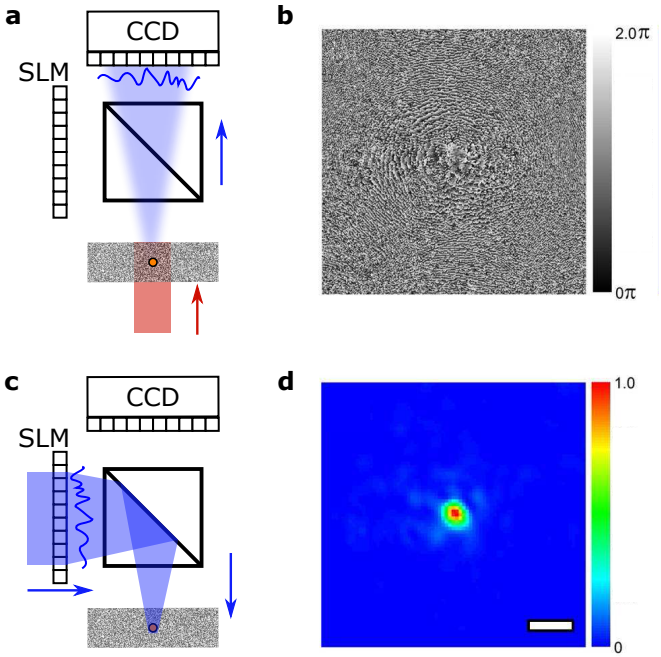

Figure 1.22 – Digital optical phase conjugation of second harmonic signal. a) Second harmonic radiation (blue) is excited by a pump beam (red) from a nanoparticule (orange dot) embedded inside a scattering medium. The scattered field is measured on a CCD camera. b) Conjugated phase pattern of the hologram measured with the CCD camera. c) This conjugated phase pattern is displayed on an SLM and read with a second laser beam (blue). Light is thus focused back on the SHG emitter. d) Normalized intensity of the phase conjugated focus through a scattering layer (which differs from the situation actually depicted in (c)), measured in the plane of the SHG emitter. scale bar: 5 µm. source b,d: [Hsieh 10b]

However, it requires a guide star that emits temporally coherent light. SHG is preferred for such task, but narrowband filtered fluorescence can also be phase conjugated [Vellekoop 12]. It is however not well suited for practical applications as the filtering would significantly decrease the amount of available signal. This has also been demonstrated only through scattering layers and not inside.

Coupling optics and acoustics

All-optical techniques share a common weakness: the signal probing light intensity at depth is also distorted by the scattering medium. As a result, very high excitation intensities are often required to generate detectable feedback signals, especially in the case of non-linear mechanisms. Moreover, if the whole sample is fluorescent, the modulation of the non-linear signal generated deep inside the sample would also be perturbed by a huge surface background, as mentioned in section 1.3.1.

An alternative approach introduces mechanisms coupling light and ultrasound (in the MHz range). As the latter are only weakly scattered by soft tissue, this strategy is particularly well-suited for biological applications. Ultrasonic waves indeed propagate mostly in a ballistic manner in soft tissues (blood, fat, muscle,...). These soft tissues exhibit very similar properties for ultrasound propagation (mainly compression properties, close to those of water). Ultrasonic waves are thus barely refracted, and can be considered to propagate in straight line in soft tissue, at a velocity approximately equal to 1.5 mm.µs^{-1}. They can therefore be manipulated exactly as light in transparent media, for focusing or imaging purposes, which is widely used for obstetric ultrasound imaging for instance. The resolution of this imaging technique is approximately given by the wavelength of the ultrasounds, which ranges from the millimeter down to a few tens of micrometers, for frequencies ranging from a few MHz to a few tens of MHz. Unlike optics, this resolution is limited by absorption rather than scattering. The ultrasound absorption coefficient in tissue varies quasi-linearly with the ultrasonic frequency [Goss 79], which establish a trade-off between imaging depth and resolution. This coefficient is of the order of 0.5 dB/cm/MHz, which still enables to image up several centimeters deep.
Coupling light and sound enables in essence to probe light intensity in a specific tight region deep inside soft tissue thanks to the preserved acoustic resolution. Two particular coupling mechanisms are of interest here: acousto-optic modulation and photo-acoustic generation[3].

Acousto-optic tagging

The acousto-optic effect has been known for almost a century: diffraction of light by an acoustic wave propagating in a fluid or a crystal was theoretically predicted by Léon Brillouin in 1922 [Brillouin 22] and experimentally shown by in 1932 by Lucas and Debye [Debye 32].
Basically, an acoustic wave propagating in a homogeneous medium at the frequency f_{ac} has two effects on a light beam: it deflects the beam as a grating, and the m^{th} diffraction order is frequency-shifted by $m \cdot f_{ac}$. In heterogeneous media, it has been shown that both refractive index modulation due to pressure fluctuations and modulation of optical path lengths due to scatterers vibrations affect the phase of the optical wave.
As a consequence, a small fraction of the light intensity is frequency shifted by $\pm f_{ac}$, often referred to as "tagged" light. It represents a shift of about 10^{-6} nm in wavelength. This effect has been used for almost twenty years to perform acousto-optic imaging , which uses the variations of tagged light intensity to image optical absorption contrast inside tissue [Kempe 97, Resink 12]. The

[3] To avoid confusion: the first word is referring to the type of wave that generates the corresponding effect, the second to the detection of waves of interest

resolution relies on the ability to focus ultrasound deep inside tissue: tagged photons are then only generated within the focal volume of a focused ultrasonic transducer.
Coming back to light focusing inside scattering tissue, one approach is to measure the outgoing frequency-shifted wavefront and to apply the same phase conjugation technique described above. As tagged photons originate only from the ultrasonic focus, the phase conjugated beam will be refocused back to this location (see Fig. 1.23). This has been first demonstrated by [Xu 11], but once again only

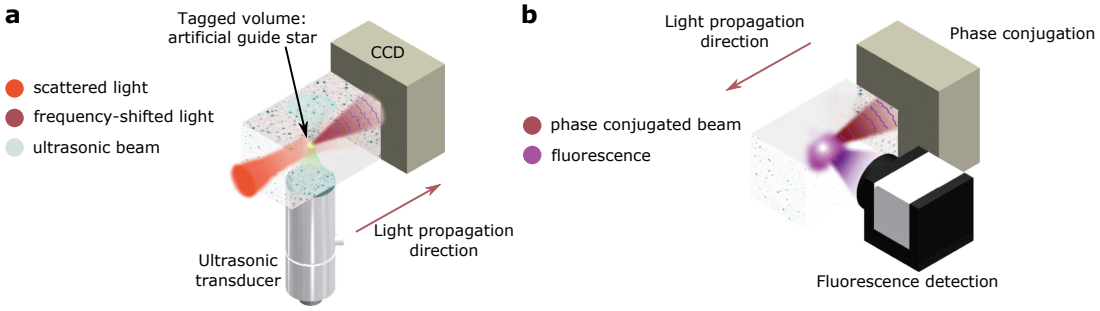

Figure 1.23 – Acousto-optics and optical phase conjugation. a) A small fraction of scattered light is acoustically tagged. The corresponding light field is measured with a CCD camera. b) The phase conjugated beam focuses back in the scattering sample and can for instance generate fluorescence. source: [Si 12]

through scattering layers. The size of the focus is limited by the acoustic frequency, but additional measurements and mathematical treatment interestingly enable to focus down to the the single speckle grain resolution [Judkewitz 13]. Tagged light can also be used as a simple feedback signal for wavefront shaping. By iteratively optimizing the amount of tagged photons, Tay and colleagues have been able to focus light within the acoustic focus [Tay 14a].
The main limitations of acousto-optics are the very weak quantity of tagged photons and the magnitude of the frequency shift itself. It is therefore quite challenging to isolate the tagged photons from the main beam. Moreover, the phase conjugation approach requires tedious optical alignment between an SLM and a CCD chip.

Photoacoustic imaging

The PA effect is the generation of sound consequently to light absorption. When a laser pulse hits an absorbing portion of the sample (which can be for example a small blood vessel [Zhang 06]), the local increase in temperature generates an ultrasound pulse that propagates away from the absorber[4]. The amplitude of the

[4] PA waves can also be generated by a continuous laser with modulated intensity, but this technique will not be addressed in this thesis.

ultrasound wave is both proportional to the light intensity on the absorber and to its absorption. Because the ultrasound wave propagates in soft tissues with negligible scattering it can be measured non-invasively by an ultrasonic transducer (or a set of transducers [Wang 12, Bossy 06]) placed outside the sample [Xu 06]. After a single laser shot, the PA signals from all absorbing targets in the transducers' field-of-view are recorded with time-of-arrivals corresponding to their distances from the transducers. An image of the absorption distribution is then formed from the time resolved signal(s). Using a standard one-dimensional (1D) array of transducers, a single laser pulse yields a two-dimensional (2D) image . Alternatively, a single spherically-focused transducer having an elongated "pencil-shaped" sensitivity profile, provides a 1D image within its depth of field directly from the signals time-of-arrivals using a single laser pulse. Thus, a PA imaging system serves, in essence, as a virtual camera sensing the light absorption distribution inside the medium, having a resolution limited by the size of the acoustic focus. Because of increasing attenuation of ultrasounds with frequency, this resolution cannot be arbitrarily increased, and is at best of the order of a few micrometers. As a result, the depth-to-resolution ratio of PA imaging at depth is around 200 in practice [Beard 11, Wang 12]. By using a PA feedback from a single ultrasonic transducer, Kong et al. were the first to propose and perform wavefront shaping to focus light on absorbers located behind a scattering sample [Kong 11]. In this thesis, we further expanded this idea.
In the next section, we provide basics about PA generation, and some technical insights about ultrasound detection and image reconstruction.

1.5 Principles of photoacoustic imaging

In this section we provide some theoretical and experimental notions about photoacoustics that will be needed throughout the following chapters. We first describe the physics and the principle of acoustic-resolution PA imaging in deep tissue. We then introduce some technicalities about ultrasonic detection and image reconstruction from PA signals.

1.5.1 Photoacoustics theoretical basics

Brief historical interlude

The first observation of the PA effect was reported by Alexander G. Bell in 1880, during his research about remote sound communications. He noticed that sound was produced by crystalline selenium discs when illuminated by a sun beam with

modulated intensity [Bell 80]. However at the time light sources were quite weak, and it was hard to efficiently quantify the received acoustic signal, as the only available receiver was the human ear.
New developments were enabled thanks to the invention of both piezoelectric acoustic detectors and lasers during the twentieth century. Applications for biological tissue imaging appeared during the mid-1990s, and the first high quality in vivo images arose in the early 2000s. Since, PA imaging became a very active and fast growing field in biomedical imaging [Wang 12].

Fundamental equations of photoacoustics

In the following, biological tissue will be considered as a medium with homogeneous acoustical properties close to those of water[5] and potentially heterogeneous optical properties. We consider here the simplest linear model for PA generation in a homogeneous liquid medium. The PA phenomenon is governed by the coupled evolution of the temperature field $T(\mathbf{r},t)$ and the pressure field $p(\mathbf{r},t)$ at position $\mathbf{r}$ and time t, as described by the following equations [Gusev 93]:

$$\rho_0 c_p \frac{\partial T}{\partial t}(\mathbf{r},t) = \kappa \Delta T(\mathbf{r},t) + P_V(\mathbf{r},t) \tag{1.10}$$

$$\Delta p(\mathbf{r},t) - \frac{1}{c_s^2}\frac{\partial^2 p}{\partial t^2}(\mathbf{r},t) = -\rho_0 \beta \frac{\partial^2 T}{\partial t^2}(\mathbf{r},t) \tag{1.11}$$

where the different parameters denote:

- ρ_0: volumetric mass density of water
- c_p: heat capacity at constant pressure of water
- κ: thermal conductivity of water
- P_V: heat source term
- $c_s \simeq 1500$ m.s^{-1}: sound velocity in water (approximate value in water at 20°C)
- β: thermal expansion coefficient at constant pressure of water

Eq. 1.10 describes the temperature diffusion process with a source term. Eq. 1.11 is an acoustic wave equation with an acoustic source term arising from temporal variations of temperature.

[5] Water will always stand for liquid water in this thesis.

Light absorption drives the heat source:

$$P_V(\mathbf{r},t) = \mu_a(\mathbf{r})\phi(\mathbf{r},t) \tag{1.12}$$

where μ_a is the spatially varying optical absorption of the medium (and will be the imaging contrast), and ϕ is the light fluence rate in the medium, which also depends on position $\mathbf{r}$ and time t.

Confinement regimes

We will now consider the specific case of nanosecond pulsed illumination, which is most widely used for PA imaging. We shall see that a few additional assumptions enables to further simplify the previous equations, and thus to provide potential solutions for image reconstruction.
We consider an absorbing object of typical size D_a under a pulsed illumination of typical duration τ_p, and we introduce the heat diffusion coefficient $\chi = \frac{\kappa}{\rho_0 c_p} \simeq 1.4\ .\ 10^{-7}\ m^2.s^{-1}$ (in water at 20°C).
A first characteristic time scale of the problem is:

$$\tau_{th} = \frac{D_a^2}{\chi} \tag{1.13}$$

It quantifies the time over which the heat diffuses on the characteristic length of the absorber D_a. The thermal confinement regime is reached whenever $\tau_p \ll \tau_{th}$. In this regime, there is no significant heat diffusion during light absorption. Eq. 1.10 can thus be simplified:

$$\frac{\partial T}{\partial t}(\mathbf{r},t) = \frac{1}{\rho_0 c_p} P_V(\mathbf{r},t) \tag{1.14}$$

which in turn leads to:

$$\Delta p(\mathbf{r},t) - \frac{1}{c_s^2}\frac{\partial^2 p}{\partial t^2}(\mathbf{r},t) = -\frac{\Gamma}{c_s^2}\frac{\partial P_V}{\partial t}(\mathbf{r},t) \tag{1.15}$$

where $\Gamma = \frac{\beta c_s^2}{c_p}$ is the so-called Grüneisen parameter ($\Gamma \simeq 0.1$ in water at 20°C). Under this assumption, the source term can be written as:

$$P_V(\mathbf{r},t) = \mu_a(\mathbf{r})\phi(\mathbf{r})f(t) \tag{1.16}$$

where f denotes the temporal profile of the illumination. Considering a typical laser pulse duration of 5 ns, the thermal confinement regime is reached when the absorber diameter is much larger than about 27 nm. Therefore this condition

will always be valid in PA imaging, except in a few cases involving nanometric particles [Zharov 11, Prost 15].

The second time scale is the time during which the pressure wave propagates along the typical length of the absorber D_a:

$$\tau_{ac} = \frac{D_a}{c_s} \tag{1.17}$$

The stress confinement regime is reached when $\tau_p \ll \tau_{ac}$. For a typical laser pulse duration of 5 ns, the stress confinement regime will be reached when the absorber diameter is larger than 7.5 µm.
When $\tau_p \ll \tau_{ac}$ and $\tau_p \ll \tau_{th}$, the light absorption is considered instantaneous, and the source term can be written as:

$$P_V(\mathbf{r}, t) = \mu_a(\mathbf{r})\phi(\mathbf{r})\delta(t) \tag{1.18}$$

which leads to:

$$\Delta p(\mathbf{r}, t) - \frac{1}{c_s^2}\frac{\partial^2 p}{\partial t^2}(\mathbf{r}, t) = -\frac{\Gamma}{c_s^2}\mu_a(\mathbf{r})\phi(\mathbf{r})\frac{d\delta(t)}{dt} \tag{1.19}$$

Another convenient way to write this equation is to replace the source term by initial conditions, as follows:

$$\begin{aligned} &\Delta p(\mathbf{r}, t) - \frac{1}{c_s^2}\frac{\partial^2 p}{\partial t^2}(\mathbf{r}, t) = 0 && \forall\ \mathbf{r}, t > 0 \\ &p(\mathbf{r}, t = 0) = p_0(\mathbf{r}) = \Gamma\mu_a(\mathbf{r})\phi(\mathbf{r}) && \forall\ \mathbf{r} \\ &\frac{\partial p}{\partial t}(\mathbf{r}, t = 0) = 0 && \forall\ \mathbf{r} \end{aligned} \tag{1.20}$$

This shows that PA waves generation can be seen as relaxation of an instantaneous initial pressure rise.
The resolution of equations 1.10, 1.11 and 1.12 may be carried out using Green function approach. However, even in the most simplified case of heat and stress confinement regimes, no analytic solutions necessarily exist because of the potentially complex distribution of $\mu_a(\mathbf{r})\phi(\mathbf{r})$. Fig. 1.24.a,b illustrates the solution obtained in the simple case of a homogeneously absorbing sphere in the stress and heat confinement regimes [Diebold 91].

We now consider the use of small objects, such that the stress confinement regime is not valid anymore. We assume that the thermal confinement is still valid. The temporal profile of the light pulse must then be taken into account. Let τ_p denote its characteristic time. The pulsed illumination then acts as a low pass filter,

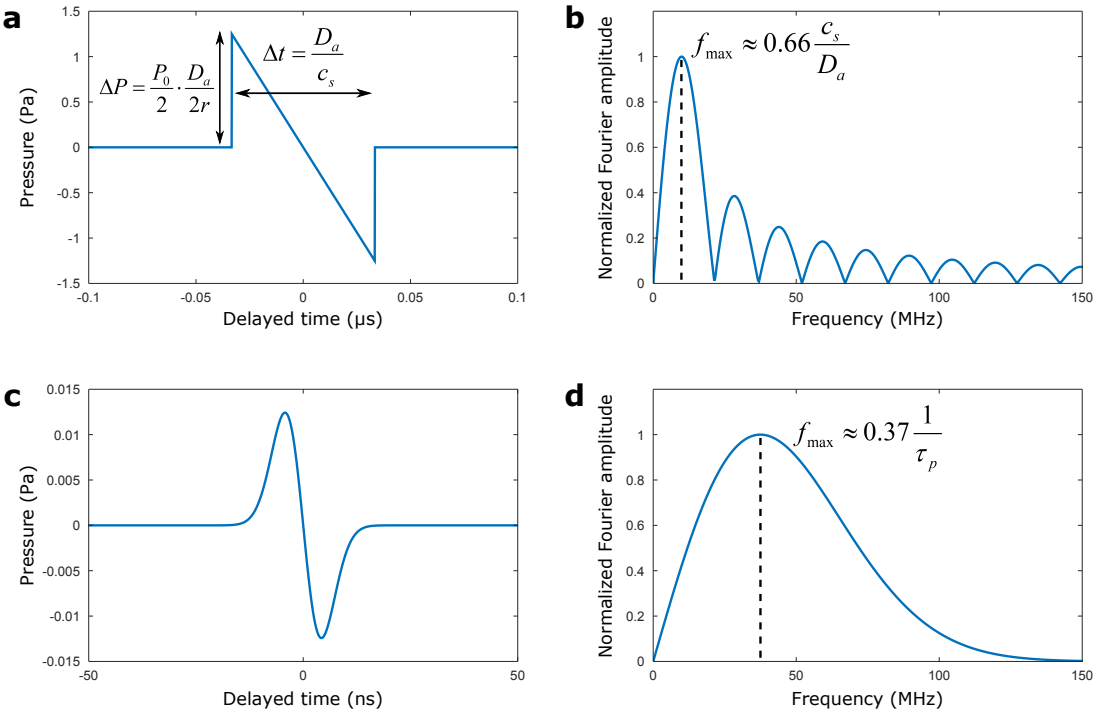

Figure 1.24 – Photoacoustic generation by a homogeneously absorbing sphere. a) PA signal generated by a homogeneously absorbing sphere (diameter: D_a=100 µm, absorption: $\mu_a = 1$ cm^{-1}), illuminated by a light pulse (duration: $\tau_p = 5$ ns, fluence rate: $\phi = 5$ mJ.cm^{-2}), detected at a distance $r = 10$ mm. The sphere and the surrounding medium have the mechanical properties of water: $c_s = 1500$ m.s^{-1}, $\Gamma = 0.1$. The stress confinement is verified. Delayed time (x-axis) is expressed in Eq. 1.21. b) Corresponding normalized spectrum. The frequency of maximum amplitude f_{max} is set by the size of the sphere. c) PA signal generated by a homogeneously absorbing sphere (diameter: D_a=10 µm, absorption: $\mu_a = 1$ cm^{-1}), illuminated by a light pulse (duration: $\tau_p = 10$ ns, fluence rate: $\phi = 5$ mJ.cm^{-2}), detected at a distance $r = 10$ mm. The sphere and the surrounding medium have the mechanical properties of water: $c_s = 1500$ m.s^{-1}, $\Gamma = 0.1$. The stress confinement is not verified here. d) Corresponding normalized spectrum. The frequency of maximum amplitude f_{max} is set by the duration of the illumination pulse.

and it can be shown that the pressure field is proportional to the derivative of the temporal profile f [Calasso 01]:

$$p(\mathbf{r}, t) \propto \frac{df(\widehat{\tau})}{d\widehat{\tau}} \qquad \text{where} \quad \widehat{\tau} = \frac{t - \frac{\|\mathbf{r}\|}{c_s}}{\tau_p} \tag{1.21}$$

When using a 5 ns laser pulse, this regime will be relevant for objects smaller than 7.5 µm: the spectral content is not limited anymore by the size of the imaged structures but by the temporal width of the illumination. Fig. 1.24.c,d illustrates the temporal and spectral behaviour of PA emission of an uniformly absorbing sphere illuminated by a nanosecond pulse with a gaussian temporal

profile, while maintaining the thermal confinement regime.
To sum up, under nanosecond pulse illumination, the ultrasonic frequency is set by:

- the size of the object if its size is larger than ∼10 µm
- the duration of the pulse if the object is smaller than ∼10 µm.

1.5.2 Ultrasonic detection

The principle of deep tissue acoustic resolution PA imaging is to retrieve the initial pressure rise:

$$p_0(\mathbf{r}) = \Gamma \mu_a(\mathbf{r}) \phi(\mathbf{r}) \tag{1.22}$$

from the pressure field measurement on the boundaries of the sample of interest. It should be noted that such initial pressure rise distribution is defined only when both stress and heat confinement are verified. The image reconstruction will be discussed in the next section. The Grüneisen factor $\Gamma = \frac{\beta c_s^2}{c_p}$ will be assumed to be uniform here. However in some cases, inhomogeneities of the speed of sound c_s can be taken into account [Jose 12]. Moreover, the temperature dependence of the thermal expansion coefficient β, either dynamic [Simandoux 15a] or pulse to pulse [Wang 14b], can be used to perform non-linear PA imaging. It should be noticed that the image contrast is not only given by the absorption μ_a, but also by the light intensity distribution. This illumination is considered uniform in most cases, but diffusion models can also be used to compensate for fluence attenuation at large depth [Hussain 12]. Standard PA imaging setups use indeed incoherent lasers as light source, leading in depth to a diffusive halo illumination. Our interest rather lies in the use of coherent illumination, and Eq. 1.22 confirms that the speckle intensity could be probed at depth using such an imaging modality.

To measure the pressure field $p(\mathbf{r}, t)$ at the sample boundaries, three main ultrasonic detection setups are employed.
Optical detection of acoustic waves can be performed, using for instance a Fabry-Perot interferometer, but this entirely lies beyond the scope of this thesis [Zhang 08].
Piezo-electric detection is the prominent technology used in ultrasound imaging.

Such acoustic transducers commonly take two forms:

- single element transducer: usually spherically focused, which means that it can detect acoustic signals originating only from a tight region, called focal volume (see Fig. 1.25.a). It provides a 1D image along its axis, and must be scanned in order to provide 2D or 3D images.

- linear transducer array: composed of multiple cylindrically focused transducers (see Fig. 1.25.c,d), which receive signal from a plane (or a thick layer in practice). It provides a 2D image in a single shot as detection is performed over several elements in parallel. Curved arrays can also used, but it will not be discussed here.

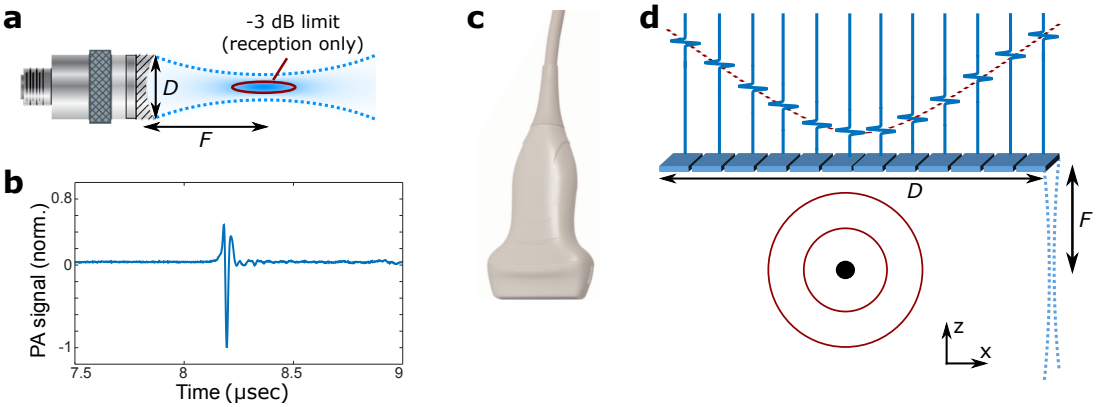

Figure 1.25 – Ultrasonic detection. a) Spherically focused single element transducer. Shaded blue depicts the detection sensitivity. F denotes the focal length of the transducer, D its diameter. b) Typical PA signal obtained with such transducer, generated by an absorber under nanosecond illumination, located within the focal region. c) Ultrasonic linear array used for clinical application. d) Principle of ultrasonic detection with a linear array. An acoustic point source is detected by each element with some delay. The blue dotted lines illustrate the cylindrical focus of the elements. This focus is called the elevation focus, and F denotes the corresponding focal length. D denotes the length of the array.

Although they can in general operate as emitters, ultrasonic transducers are only used as receivers in PA imaging, since the excitation is optical. Typical imaging frequencies range between 1 and 100 MHz, for a field-of-view of the order of centimeters. Much higher frequencies cannot be used at large depth in tissue as they are too much attenuated. These detectors are far from being perfect: they have a finite bandwidth as well as a finite numerical aperture, which lead to several kinds of artefacts in the images. The finite aperture is a geometrical effect: detectors cannot usually cover the full 4π solid angle around the sample. The filtering effect introduced by the finite bandwidth of the transducer has several causes: the finite size of the elements, the electrical response of the transducer,

the detection electronics response, etc... Potential artefacts arising from these limitations will be described in detail in section 4.1. Accounting for all these constraints, in the simplest case of a spherically-focused transducer, the imaging spatial resolution (lateral: Δx, axial: Δz) is given by:

$$\begin{aligned} \Delta x =& \frac{c_s}{f} \cdot \frac{F}{D} && \text{(limited by diffraction)} \\ \Delta z =& c_s \ \Delta\tau \propto \frac{c_s}{\Delta f} && \text{(limited by bandwidth)} \end{aligned} \tag{1.23}$$

where c_s is the speed of sound in water, f the central frequency, F the focal length, D the size (the diameter for a spherically-focused single element transducer, the length for a linear array), and $\Delta\tau \propto 1/\Delta f$ the bandwidth-limited temporal resolution of the transducer, according to the impulse response of the system.

1.5.3 Image reconstruction

For a raster-scanned single element transducer, the reconstruction is usually straightforward as 1D images of absorbers located within the focal zone of the transducer are stacked to provide 2D or 3D images (see Fig. 1.26.a). Synthetic aperture tomographic reconstruction can also be performed for out-of-focus absorbers [Omar 13]. In the case of a linear array, the image reconstruction is performed by a so-called beamforming algorithm. In this section, we describe its general principles.
In the heat and stress confinement regime, the problem of PA imaging is to find the solution $p_0(\mathbf{r}) = \Gamma\mu_a(\mathbf{r})\phi(\mathbf{r})$ of equations 1.20 from the measurement of $p(\mathbf{r}, t)$ on a given surface surrounding the sample of interest [Rosenthal 13, Xu 06]. A back-projection formula has been derived in [Xu 05] (under the assumption of constant sound velocity) and reads:

$$p_0(\mathbf{r}) = \int_{S_0} \left[2p(\mathbf{r_0}, t) - 2t \frac{\partial p(\mathbf{r_0}, t)}{\partial t} \right]_{t=\frac{|\mathbf{r}-\mathbf{r_0}|}{c_s}} \frac{d\Omega_0}{\Omega_0} \tag{1.24}$$

where $\mathbf{r_0}$ denotes the positions of the detectors, S_0 the surface of the detector, corresponding to a solid angle $\Omega_0 = 2\pi$ for planar geometry, $d\Omega_0$ the solid angle element corresponding to the detector surface element, and c_s the sound velocity. In the far-field approximation, i.e. when the distances between sources and detectors are larger than the acoustic wavelengths at stake, the first term $p(\mathbf{r_0}, t)$ can be neglected. The factor $2t$ compensates for the geometrical attenuation and can be neglected in the case of a small field-of-view, which often leads to a faster computational reconstruction. The factor $\frac{d\Omega_0}{\Omega_0}$ can also be disregarded

when assuming point-like transducer elements. A more intuitive presentation of the back-projection algorithm is given in Fig. 1.26.b.

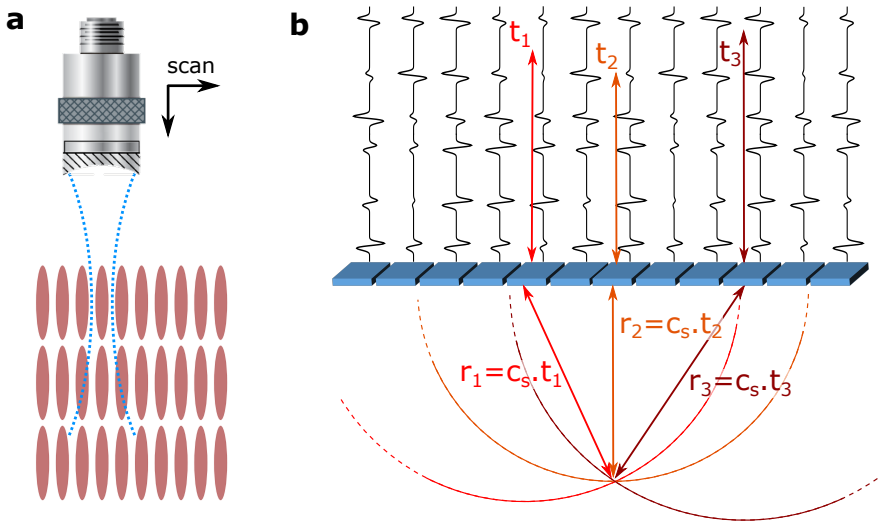

Figure 1.26 – Photoacoustic image reconstruction. a) Single element: the transducer is scanned along 2 or 3 dimensions, the image is obtained directly by placing the successive one-dimensional images next to each other. b) Two-dimensional beamforming with signals from a linear array: the image space is divided in a grid of individual pixels; the value of each pixel is obtained by summing the acoustic signals of each element (or their derivative) at the right delay. On the example, the pixel is located at different distances r_i from all distinct elements, each corresponding to a given delay t_i in the signals. The value of this pixel is thus obtained by summing the signals of element i at t_i.

When the stress confinement regime is not verified, no initial pressure rise p_0 can be defined. Usually PA images are still reconstructed in this case using Eq. 1.24, the temporal profile of the excitation will then cause an additional blur of the resulting image. Nevertheless, it does not constitute a strong limitation: the validity of Eq. 1.24 relies on other hypotheses (infinite bandwidth, full aperture detection) that are usually not verified even in the stress confinement regime. The imperfection of the reconstruction results in a deteriorated resolution, but the linearity of the PA amplitude with respect to the light intensity is still maintained. PA imaging is then able to probe light intensity at depth in a soft scattering sample. In the following chapter, we experimentally demonstrate how this PA signal can be used to measure the transmission matrix of a scattering sample.

1.6 Summary

In this chapter, we presented some basic principles of optical imaging. In particular, we highlighted how the ability to focus light in the sample of interest was a crucial requirement to perform high resolution imaging. Therefore, the imaging depth of optical microscopy in biological tissue is highly limited, due to aberrations and scattering induced by fluctuations of the refractive index at multiple scales. We presented a few strategies to overcome this limitation, either by filtering the non-scattered ballistic component of the incident light beam or by compensating the refractive index aberrations encountered by this ballistic component. We then introduced the concept of complex wavefront shaping, which aims at controlling the scattered light by shaping the incident wavefront with SLMs, similarly to adaptive optics. We emphasized that despite the fact that no perfect correction is achievable with this technique, light can still be focused down to the diffraction limit with a finite contrast, which depends on the number of controllable degrees of freedom of the SLM. This method requires a feedback signal monitoring the scattered light intensity. As this intensity cannot be measured deep inside biological tissue with a regular CCD camera, we introduced several probing mechanisms that can potentially be used to perform light focusing inside scattering tissue. In the next chapters of this thesis, we shall exploit the PA effect to probe the speckle intensity deep inside soft tissue. We therefore introduced basic principles of PA imaging that will be required throughout this manuscript.

Chapter 2

Photoacoustic Transmission Matrix

Contents

Focusing scattered light via wavefront shaping requires a feedback signal probing the light intensity at a given targeted point. Such feedback allows one to maximize this intensity on the target, either through iterative optimization or using the transmission matrix approach (see section 1.4.3). Although manipulation of scattered light seems relevant for imaging purposes, most of the proposed approaches to date relied on a direct and thus invasive optical imaging of the target plane. Building on [Kong 11], we propose here to use the photoacoustic effect to probe light intensity at depth in tissue.

Photoacoustic imaging has emerged in the past decade as a powerful hybrid modality to image optical absorption contrast in turbid soft media [Beard 11]. Because ultrasound waves are only weakly scattered by tissue, images can be obtained at penetration depth up to a few centimeters with sub-millimeter resolution (see section 1.4.4).

In this chapter, we transpose the concept of optical transmission matrix introduced in the first chapter to photoacoustic-guided wavefront shaping. The transmission matrix encodes the complex relations between input incident modes and output target modes. When using a photoacoustic feedback signal, pixels of the photoacoustic image replace the camera pixels as the output modes. The essential advantage of this matricial approach over optimization performed by Kong and colleagues [Kong 11] relies on a measurement sequence that is independent on the number of investigated targets, resolution cells, or the size of the probed volume (i.e. the field-of-view). The information contained in this non-invasively measured matrix can then be directly used to selectively focus light on any absorbing target at will.

We will first define the so-called photoacoustic transmission matrix (PATM), and show how it is related to the optical transmission matrix previously introduced in section 1.4.3 of the first chapter. The experimental setup, involving a one-dimensional PA imaging setup, and the matrix measurement process is then described. In a third section, we demonstrate the focusing capability of this method through various scattering samples, including a 0.5 mm-thick chicken breast sample. We show how the optical memory effect of the scattering medium can be extracted from the PATM, and we study the potential use of singular value decomposition (SVD) of this matrix to localize and discriminate targets. To demonstrate the generality of the principle, we finally extend this matricial approach to two-dimensional PA imaging, using a standard linear ultrasonic array.

This chapter is adapted and extended from:
Chaigne, Katz, Boccara, Fink, Bossy & Gigan, *Controlling light in scattering media non-invasively using the photoacoustic transmission matrix*, Nature Photonics, 2014 [Chaigne 14a]
Chaigne, Gateau, Katz, Bossy & Gigan, *Light focusing and two-dimensional imaging through scattering media using the photoacoustic transmission matrix with an ultrasound array*, Optics letters, 2014 [Chaigne 14c]

2.1 Theoretical framework: how do photoacoustic and optical transmission matrices relate?

In this section, we derive the information content of the PATM, based on the formalism introduced in section 1.4.3 of the first chapter. A PA imaging setup (1D for now) is here replacing the commonly used camera, allowing the non-invasive measurement of the transmission matrix inside a scattering medium (see Fig. 2.1). The main difference is that unlike an optical detection, the resolution of this acoustic imaging system may be not in general able to resolve a single speckle grain. In such a case, the PA signal amplitude from a given position results from several optical speckle grains illuminating absorbing objects within the ultrasound resolution cell volume (determined by the numerical aperture and the frequency response of the acoustic transducer as introduced in section 1.5 of the first chapter).

Let $t_{m'n'}$ be the coefficients of the optical transmission matrix characterized in one plane within (or behind) the scattering medium. Using the same notations as in section 1.4.3, the optical field at the $m'^{\,th}$ speckle grain in that plane is given by :

$$E^{out}_{m'} = E^{ref}_{m'} + \sum_{n'=1}^{N_{SLM}} t_{m'n'} E^{in}_{n'}$$

where $E^{ref}_{m'}$ is a constant background reference light field, originating from the unshaped part of the input field. No external reference beam could be used in this configuration.
According to Eq. 1.22, the measured PA signal amplitude at any time delay τ_m following the laser pulse is, on first approximation [Beard 11], proportional to the linear sum of all the optical modes intensities contained within the absorbing area in the probed elementary acoustic volume v centered around the axial position

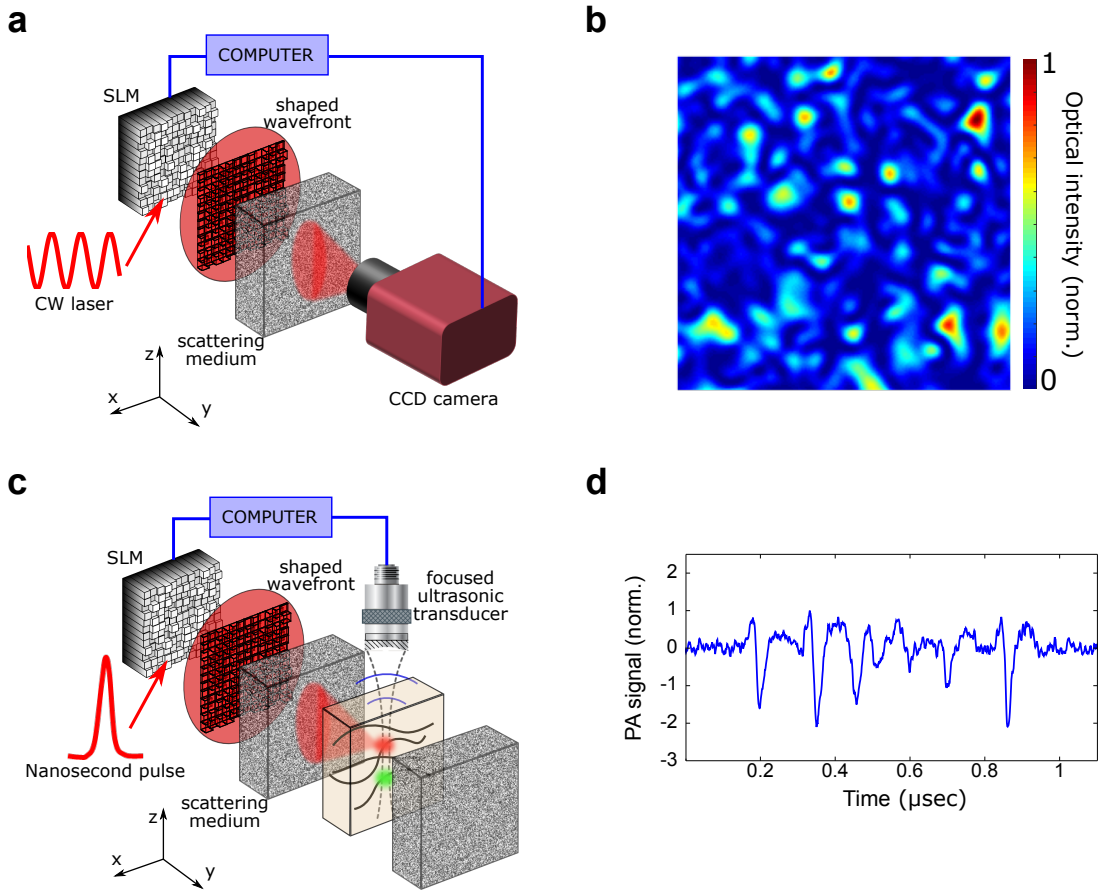

Figure 2.1 – Photoacoustic-guided wavefront shaping principle. a) Standard wavefront shaping setup: the wavefront of a monochromatic continuous wave laser is shaped by an SLM. The shaped light field propagates through a scattering layer, and the outgoing speckle field is imaged in one plane by a CCD camera. b) Optical feedback signal: typical speckle pattern, as measured by the CCD camera. c) Photoacoustic-guided wavefront shaping setup: the wavefront of a nanosecond pulsed laser is shaped. Light then propagates inside the scattering medium and illuminates absorbing structures. A spherically-focused ultrasonic transducer measures the generated photoacoustic signals. d) Photoacoustic feedback signal: typical ultrasonic temporal trace from an absorbing sample under speckle illumination (following a single laser shot), as measured by the transducer; peaks at different time delays correspond to targets at different depths along the transducer axis.

$z_m = c_s \tau_m$ from the transducer:

$$v \simeq \Delta z \cdot \frac{\pi}{4} \Delta x^2 \simeq (c_s \cdot \Delta\tau) \cdot \frac{\pi}{4} \left(\frac{c_s}{f} \frac{F}{D} \right)^2$$

where c_s is the speed of sound in water, Δz and Δx the axial and transverse spatial resolutions respectively, as defined in equations 1.23, with f is the transducer central frequency, F its focal length, D its diameter, and $\Delta\tau = 1/\Delta f$ the

bandwidth-limited temporal resolution of the transducer, according to the impulse response of the system. Thus, under these assumptions, the measured PA signal amplitude $V_{PA}(\tau_m)$ at a time delay τ_m is proportional to the sum of the optical intensities over all the modes m' impinging on absorbing targets contained in the corresponding volume $v(\tau_m)$, centered around $z_m = c_s\tau_m$:

$$V_{PA}(\tau_m) \propto \sum_{m' \in v(\tau_m)} \mu_{a,m'} |E^{out}_{m'}|^2 = \sum_{m' \in v(\tau_m)} \mu_{a,m'} \left| E^{ref}_{m'} + \sum_{n'=1}^{N_{SLM}} t_{m'n'} E^{in}_{n'} \right|^2 \quad (2.1)$$

where $\mu_{a,m'}$ is the local absorption at the position of the m'_{th} speckle grain and $E^{out}_{m'}$ is the optical field at this position. The same transmission matrix measurement protocol presented in the first chapter is performed. Each n^{th} mode of the input field on the SLM (in the Hadamard basis) is successively phase shifted from 0 to 2π relatively to the reference beam: $E^{in}_{n'} = \delta_{n,n'} \ |E^{in}_{n,0}| \ e^{i\phi^{SLM}}$, where ϕ^{SLM} is the additional phase shift.
As a result, the measured PA signal amplitude at any time delay τ_m evolves according to:

$$\begin{aligned} V_{PA,n}(\tau_m) &\propto \sum_{m' \in v(\tau_m)} \mu_{a,m'} \left| E^{ref}_{m'} + E^{in}_{n,0} t_{m'n} e^{i\phi^{SLM}} \right|^2 \\ &= \sum_{m' \in v(\tau_m)} \Big(a_{m'n} + b_{m'n} \cos(-\phi^{ref}_{m'} + \phi_{m'n} + \phi^{SLM}) \Big) \end{aligned} \quad (2.2)$$

with $a_{m'n} = \mu_{a,m'} \left(|E^{ref}_{m'}|^2 + |E^{in}_{n,0} t_{m'n}|^2 \right)$, and $b_{m'n} = 2\mu_{a,m'} |E^{ref}_{m'} E^{in}_{n,0} t_{m'n}|$.
It then follows:

$$V_{PA,n}(\tau_m) \propto \alpha_{mn} + \beta_{mn} \cos(\theta_{mn} + \phi^{SLM}_n) \quad (2.3)$$

where:

$$\begin{aligned} \alpha_{mn} &= \sum_{m' \in v(\tau_m)} a_{m'n} \\ \beta_{mn} \cos\theta_{mn} &= \sum_{m' \in v(\tau_m)} b_{m'n} \cos(-\phi^{ref}_{m'} + \phi_{m'n}) \\ \beta_{mn} \sin\theta_{mn} &= \sum_{m' \in v(\tau_m)} b_{m'n} \sin(-\phi^{ref}_{m'} + \phi_{m'n}) \end{aligned}$$

The noticeable result of Eq. 2.3 is that the measured PA signal, although being proportional to the summed intensities of many uncorrelated optical speckle grains, still follows a cosine modulation as a function of the input phase shift ϕ^{SLM}. The PATM coefficients are thus defined as $t^{PA}_{mn} = \beta_{mn} e^{i\theta_{mn}}$.

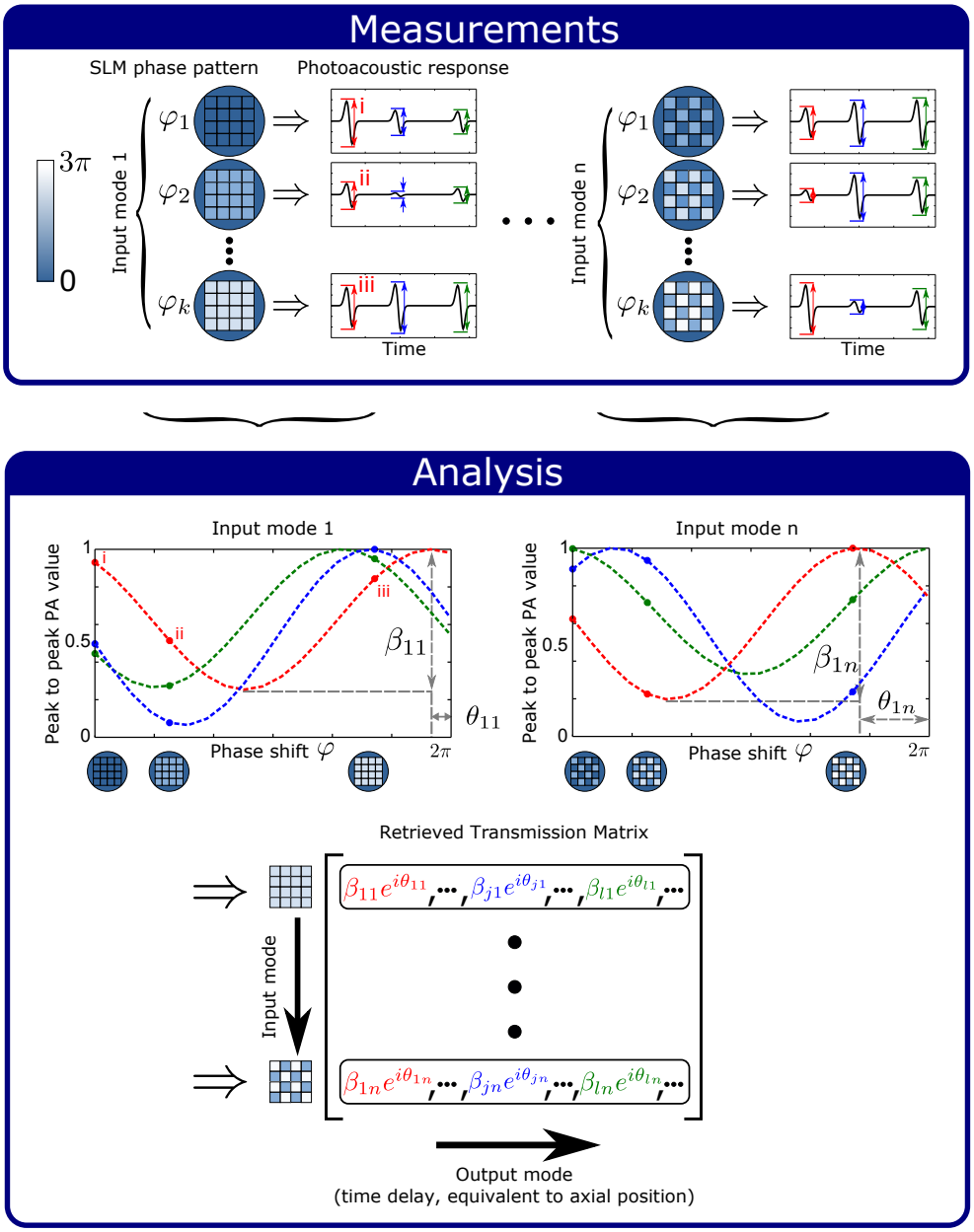

Figure 2.2 – Photoacoustic Transmission Matrix measurement process.
Measurements: the phase of each SLM input mode (in the Hadamard basis) is scanned from 0 to 2π in K steps, and the corresponding photoacoustic trace is measured for each phase-step. The unshaped part of the circular input beam serves as a fixed reference field. The signal peak-to-peak value is then analyzed for a 90 ns time-window scanned across the signal to obtain the influence of every input mode on each of the time-windows (acoustic resolution cells).
Analysis: the peak-to-peak signal of each time-window closely follows a cosine modulation as a function of the input mode phase; the PATM elements are retrieved directly from these cosine modulations phases θ_{ij} and amplitudes β_{ij} for all input-output modes pairs (j,i). The matrix is converted to the SLM-pixel input basis by a basis transformation.

The main practical difference between this PA modulation and the modulation in the all-optical transmission matrix experiment is that the modulation contrast $\frac{\beta_{mn}}{\alpha_{mn}}$ is reduced compared to the direct measurement of the optical transmission matrix. This modulation contrast is inversely proportional to the square root of the total number of summed optical speckle grains, due to the fact that the modulation phase of each speckle grain is uncorrelated with the other[1] [Goodman 07, section 4.6.1]. Even though the output modes of the PATM are somehow averaged over several optical output modes, relevant information can still be extracted from this matrix, as we shall see in the following sections.

2.2 Experimental procedure

2.2.1 Experimental setup: imaging the speckle pattern using a one-dimensional photoacoustic imaging system

The experimental setup is illustrated in Fig. 2.3. A laser pulse (Continuum Surelite, 532 nm wavelength, 8 ns pulse duration, 10 Hz repetition rate, <10 mJ pulse energy) is spatially shaped by a phase-only SLM (Multi-DM, Boston Micromachines, 140 segmented mirrors). The beam is previously expanded to cover the full SLM aperture, and one beam portion of homogeneous intensity is selected using an iris. This is first required to provide equal contributions from all SLM pixels. This spatial filter is also found to be crucial since a high intensity nanosecond pulsed laser tends to exhibit fluctuations in the spatial profile of the beam. It can therefore introduce additional instability as two consecutive pulses would then produce slightly different speckle patterns, even in the case a fixed configuration of the scattering sample.
The pulse energy can be tuned using a half-wave plate combined with a polarizing beam splitter. The SLM plane is conjugated with the scattering surface by a 4-f telescope. This ensures that the optical speckle size on the target remains constant for different SLM phase-patterns [Vellekoop 10a]. A third lens (L5) adds a curvature on top of the SLM phase pattern. This lens ensures the proper mixing of the input modes in the target plane, as the scattering angle is small. The scattered light illuminates a phantom containing an absorbing structure, embedded

[1] According to Eq. 2.2, the modulated part of the PA signal is proportional to a sum of cosine with uncorrelated phases, which can be represented as a random walk in the complex plane. The modulation amplitude is then proportional to $\sqrt{M}$, where M be the number of speckle grains contained within the acoustic resolution volume. The total average signal is proportional to M, which therefore gives a modulation contrast proportional to $\frac{\sqrt{M}}{M} = \frac{1}{\sqrt{M}}$.

in an agarose gel with negligible optical scattering. The coherence length of the nanosecond pulsed laser is about a few millimeters, which is sufficient to ensure a good speckle contrast since the scattering sample is very thin.

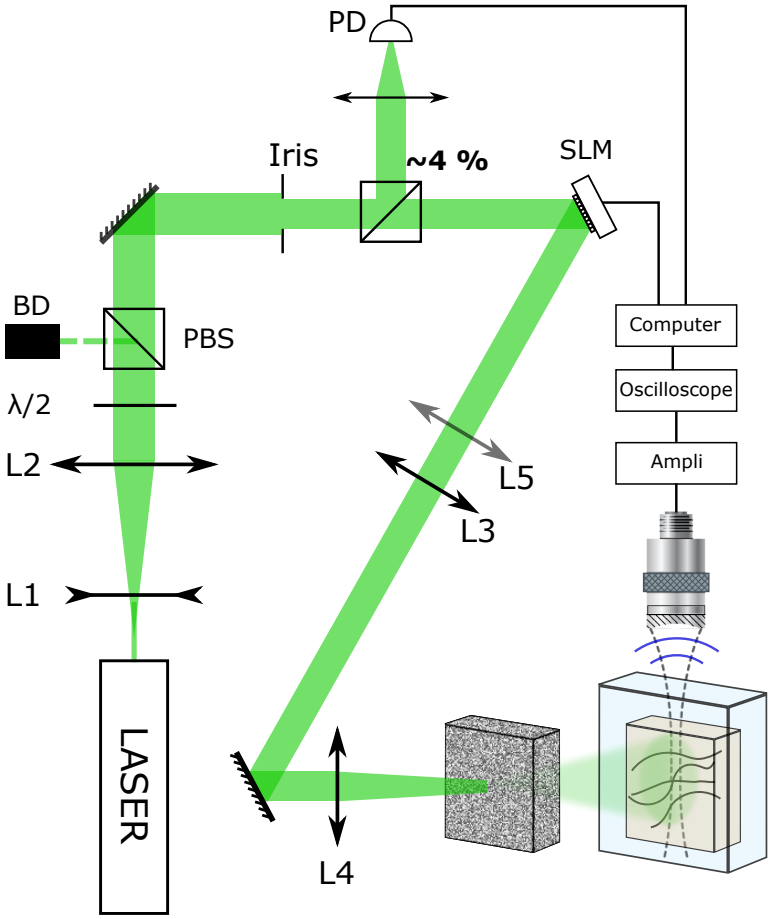

Figure 2.3 – Experimental Setup. L1: f=-50 mm, L2: f=250 mm, $\lambda/2$: half-wave plate, PBS: polarizing beam splitter, SLM: spatial light modulator, L3: f=300 mm, L4: Bausch and Lomb objective, 8x, 0.15 NA, L5: f=1000 mm.

The scattering samples are alternatively 0.5° Newport light shaping diffuser and a 0.5 mm thick chicken breast sample, partially dried and sandwiched between two glass slides. An agarose gel phantom containing 30 µm diameter absorbing nylon wires (NYL02DS, VetSuture) is placed behind the scattering sample. The absorbing wires could for instance mimic capillary vessels, a common structure of interest in PA imaging.
The PA signals generated by these absorbing wires are detected by a spherically-focused ultrasonic transducer (SNX110509-HFM13, Sonaxis), having a central frequency $f = 28$ MHz, a pulse-echo bandwidth $\Delta f = 27$ MHz (-6 dB), a diameter $D = 3.25$ mm, and a focal length $F = 7.5$ mm.

The signal from the transducer is amplified by a preamplifier (Model 5900PR, Sofranel) and recorded on an oscilloscope (Lecroy WaveSurfer 104 MXs-B). The oscilloscope signal is sampled at 1 GHz, and digitally filtered by a bandpass filter between 2 and 60 MHz, to remove any noise source outside the bandwidth of the transducer. To minimize the effects of laser pulse-to-pulse intensity fluctuations, the PA signal from each pulse was normalized by the laser pulse intensity as measured by a photodiode.
According to Eq. 1.23, the imaging spatial resolution (transverse: Δx, axial: Δz) is given by:

$$\begin{aligned} \Delta x &= \frac{c_s}{f} \cdot \frac{F}{D} \simeq 100 \text{ µm} \\ \Delta z &= c_s \Delta\tau \simeq \frac{c_s}{\Delta f} \simeq 60 \text{ µm} \end{aligned} \tag{2.4}$$

One should notice that the absorbing sample is actually not located within the scattering sample but further away. The speckle intensity is then probed behind this scattering sample in the same way as in [Popoff 10b, Vellekoop 07]. As discussed in the previous section, the experimental setup should be designed so that the number of speckle grains contained within the acoustic resolution cell is small enough to yield a measurable modulation of the PA signal.
Inside the scattering sample, after propagation over a few hundreds of micrometers, the speckle grain size is of the order of $\lambda/2$ [Sreenivasiah 79]. The acoustic resolution cell would thus contain $\sim \frac{\Delta x \cdot \Delta z}{(\lambda/2)^2} \simeq 96000$ speckle grains, which would lead to a very dim modulation of the PA signal, on the order of 0.5%.

We only consider the number of speckle grains contained within the apparent surface of the resolution cell and not within the entire volume. The underlying reason is that we only count the number of what we believe to be *independent* speckle grains. Indeed, if the electric field is known on a given closed surface, it can be derived in a unique way for any point within the volume enclosed by this surface, according to the integral theorem of Helmholtz and Kirchhoff [Goodman 05, section 3.3.3]. Our understanding is then that the number of independent degrees of freedom would be only related to the speckle grains illuminating the surface of the absorber. This analysis is currently under investigation, as it actually goes against recent claims that the *volumetric* number of speckle grains has to be taken into account [Deán-Ben 15a]. For the first proof-of-principle experiment, we then chose to artificially decrease this number of speckle grains to provide a large enough PA signal modulation. As the frequency of the transducer is fixed and the absorber size is large compared to the operating optical wavelength, the speckle size must be enlarged. We then let the scattered light propagate in free space for a few centimeters behind the scattering layer to produce ∼25 µm diameter speckle grains (see appendix B). The absorbing sample is then placed in the corresponding plane, which leads to approximately 10 independent speckle

grains per 2D resolution cell.
We employed an engineered diffuser (0.5° Newport light shaping diffuser) to control the output aperture angle while guaranteeing the absence of prominent ballistic light[2]. A small ouput angle enables to maintain a high enough intensity per speckle grain, i.e. to limit the number of output modes, which was found to be crucial for PA signal generation.
Moreover, the output speckle field is actually the incoherent sum of two orthogonally polarized speckle fields, as opposed to all-optical experiments in which a single polarization is usually selected. This results in a reduced contrast of the intensity pattern, leading in turn to a lower modulation of the PA signal by a factor $\sqrt{2}$.

2.2.2 Measuring the photoacoustic transmission matrix

To experimentally acquire the PA transmission matrix, we used the phase shifting procedure previously described. For each n^{th} input mode, ϕ^{SLM} was sequentially swept between 0 and 2π in K=16 equally spaced steps, giving a signal $V^k_{PA,n}(\tau_m)$ corresponding to each $\phi^{SLM}_k = \frac{2\pi k}{16}$, $k = 0, ..., 15$. To span the 140 controlled degrees of freedom of the SLM in the Hadamard basis, we used the smallest Hadamard basis of size ≥ 140 generated by MathWorks MATLAB's "hadamard" function, which is 160[3].
In our experiments, we choose to retrieve the transmission matrix using the PA peak-to-peak amplitude in each 90 ns time window over the measured photoacoustic time trace with 15 ns steps, instead of the signal $V^k_{PA,n}(\tau_m)$ at every time delay τ_m. The time-window width was carefully chosen to match the typical impulse response of the transducer for a single isolated absorber, maximizing the signal-to-noise ratio (SNR) while maintaining spatial resolution (see Fig. 2.4). For each phase step, the PA signals corresponding to 5 successive laser pulses were recorded and averaged, once again to maximize the SNR.
The modulation of each voxel value as a function of the K phase shifts of each SLM input mode is analyzed by computing a discrete Fourier transform (analogous to a lock-in detection).

[2] When rotating the diffuser and averaging the successive speckle patterns imaged on a camera, no prevailing central component was observed.
[3] Hadamard matrices exist for order equal to 1, 2 and any multiple of 4. However, there is no simple algorithm to compute the Hadamard matrix of order $140 = 4 * 35$.

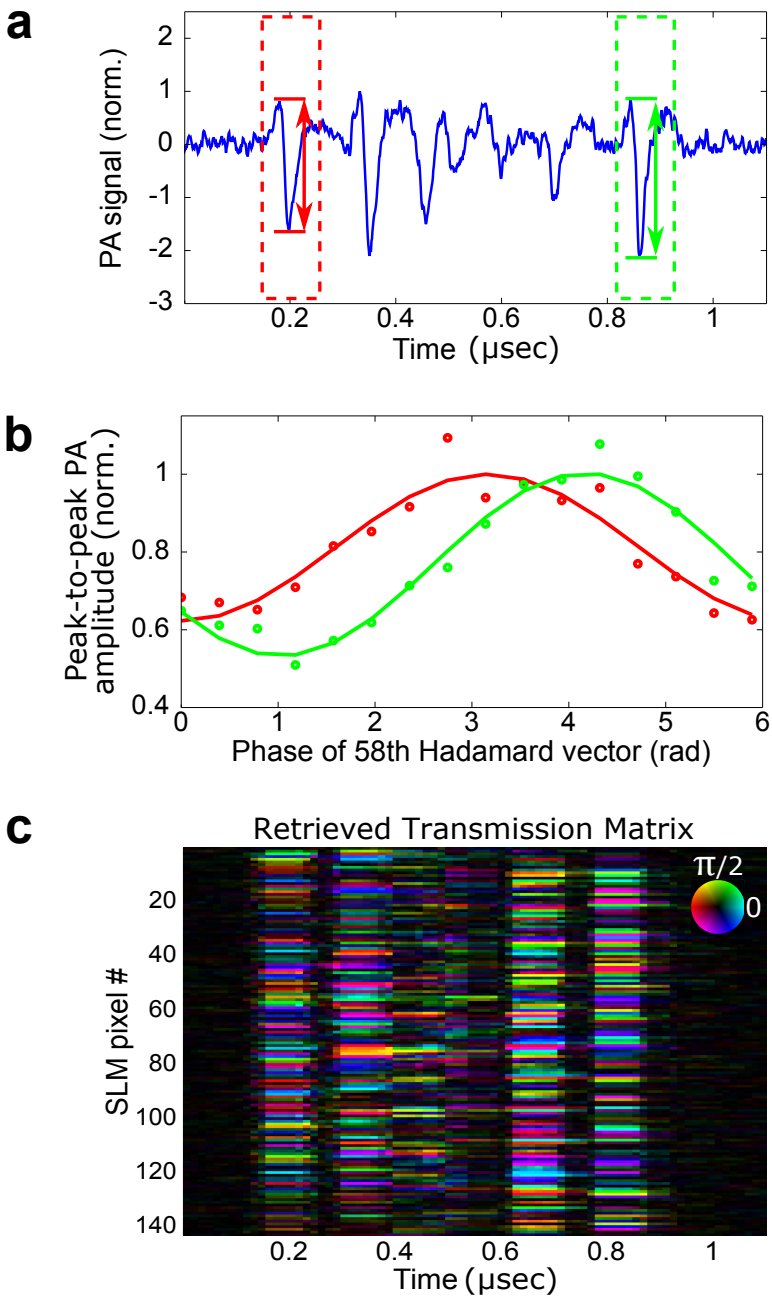

Figure 2.4 – Experimental measurement of the photoacoustic transmission matrix. a) Measured photoacoustic trace for several isolated absorbing targets, following a single laser shot through a scattering diffuser. The signals at different time delays correspond to targets at different axial positions. The framed parts correspond to the 90 ns window scanned over the whole time trace to measure the transmission matrix. The red frame matches the position of the first absorber, the green frame matches the last one. b) Evolution of the peak-to-peak signal amplitudes for two wires, corresponding to the two framed time-windows shown in (a), while scanning the phase of a single SLM input mode (in the Hadamard basis) from 0 to 2π. c) The measured complex-valued transmission matrix gives the influence of each SLM pixel (vertical axis) on each acoustic voxel (horizontal axis). Hue represents phase and brightness represents amplitude.

For each output voxel m of the PA image and input mode n, the amplitude β_{mn} and phase θ_{mn} of this modulation give the PATM element value $t^{PA}_{mn} = \beta_{mn} e^{i\theta_{mn}}$:

$$\begin{aligned} \theta_{mn} &= arg(t^{PA}_{mn}) = -arg\left(\sum_{k=1}^{16} V^k_{PA,n}(\tau_m) \cdot e^{i\frac{2\pi k}{16}}\right) \\ \beta_{mn} &= |t^{PA}_{mn}| = \left|\sum_{k=1}^{16} V^k_{PA,n}(\tau_m) \cdot e^{i\frac{2\pi k}{16}}\right| \end{aligned} \tag{2.5}$$

where $V^k_{PA,n}(\tau_m)$ now denotes the PA peak-to-peak amplitude in the 90 ns time window centered on τ_m.
In principle, this analysis requires $K \geq 3$ steps to satisfy Nyquist-rate sampling. We used K=16 to validate the assumption of signal linearity and to improve the SNR. Experimentally, the peak-to-peak signals closely followed the expected cosine modulation as a function of each input-mode phase (see Fig. 2.4.b), confirming the linearity assumption in Eq. 2.1. Equivalently, K=3 could be used and the SNR could be improved by averaging more pulses per phase step.
The photoacoustic transmission matrix T^{PA} is then directly obtained for all time windows and thus all absorbing targets, simultaneously from a number of measurements that is independent on the number of targets or the acoustic field-of-view.
In total, the PATM is obtained from $K.N_{SLM}$ measurements, resulting in a total acquisition time of 40 minutes in our experiments (K=16, $N_{SLM} = 160$, 5 laser pulses averaged per signal, acquired at a 10 Hz laser repetition rate), including all latencies, triggering and communication delays. Once the transmission matrix was measured in the Hadamard input basis, it is converted to the canonical (input SLM pixels) basis by a unitary transformation (see Fig. 1.19). An example for the PATM obtained experimentally through an optical diffuser is presented in Fig. 2.4.c. This matrix describes the influence of each input mode (SLM pixel, vertical axis) on each ultrasound resolution cell (time window in PA trace, horizontal axis).

2.3 What can you do with the photoacoustic transmission matrix?

2.3.1 Focusing light on absorbing targets

As a first demonstration for utilizing the measured PATM, we present selective light focusing on several absorbers along the focus of the ultrasonic transducer. The results for focusing obtained through an optical diffuser are presented in

Fig. 2.5. Fig. 2.5.a show the experimentally measured transmission matrix. The SLM phase pattern focusing at a specific axial position $z_m = c_s \tau_m$ is obtained by conjugating the phase of the m^{th} column of the transmission matrix:

$$\phi_n^{SLM,\ focusing\ at\ target\ m} = -\theta_{mn} = -arg\left(t_{mn}^{PA}\right) \tag{2.6}$$

for each n^{th} pixel of the SLM (Fig. 2.5.b). The PA signals obtained when successively displaying these focusing phase-patterns on the SLM are presented in Fig. 2.5.c and d. These results confirm a selective enhancement of the photoacoustic signal generated by the selected target.

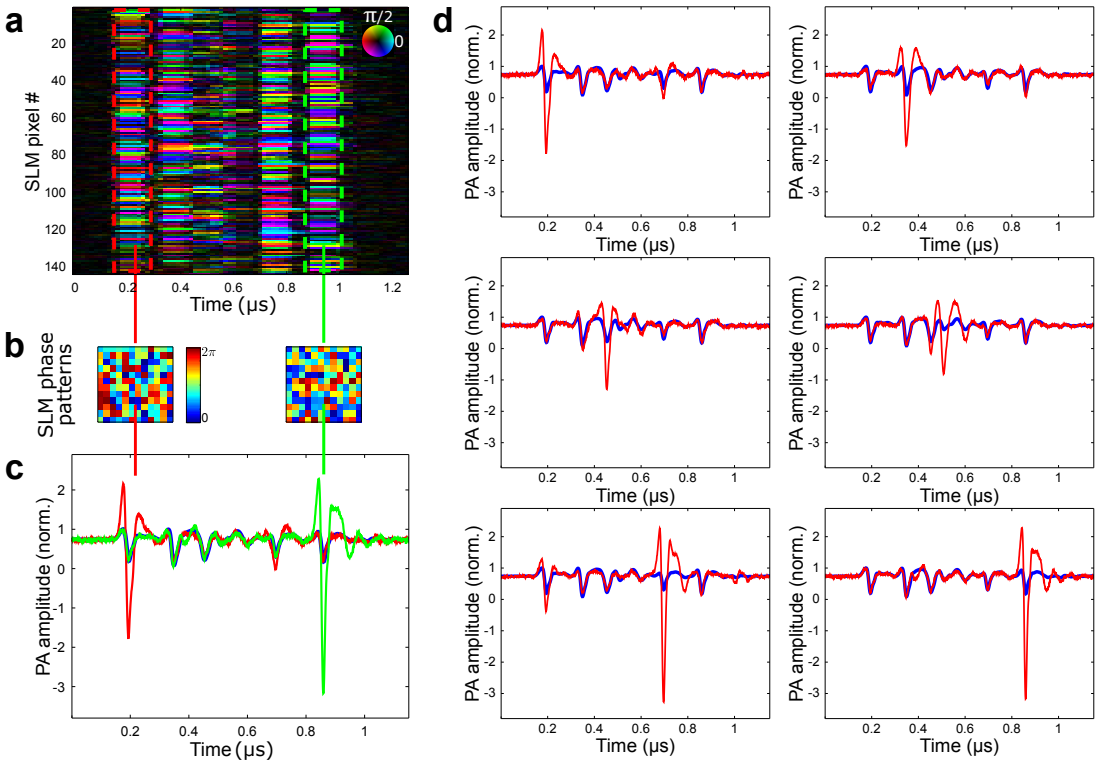

Figure 2.5 – Selective light focusing through an optical diffuser using the PATM. a) Measured transmission matrix. The red and green dashed rectangles highlight the matrix columns corresponding to two absorbing targets identified for focusing. b) The SLM phase masks for focusing on the nearest (red) and farthest (green) absorbers are given by phase conjugating these transmission matrix columns. c) Measured photoacoustic signals when displaying either a flat phase on SLM (blue), the phase-pattern in (b) focusing on the first absorber (red), or the phase pattern in (b) focusing on the farthest absorber (green). d) Photoacoustic signals when either displaying a flat phase on SLM (blue), or the focusing phase pattern for each of the six identified absorbing targets.

To estimate the expected PA signal enhancement, one has to calculate the number of independent optical modes contained within the absorbing area of the target inside the acoustic focus:

- the absorbing targets used are black nylon wires, with a diameter of $\varnothing_{absorber} = 30$ µm.
- the diameter of the acoustic focus is given by Eq. 2.4: $\Delta x \simeq 100$ µm.
- the measured speckle size at the target plane was $\varnothing_{speckle} \simeq 25$ µm.

In the case of a straight wire horizontally crossing the center of the acoustic focus, the probed absorbing area is then 3000 µm^2. The number of speckle grains contained in the effective absorbing region, i.e. the portion of the absorber that is probed by the transducer, is therefore:

$$N_{modes} \simeq \frac{3000}{\pi(12.5)^2} \simeq 6$$

The expected optical enhancement factor is then:

$$\eta = 0.5\frac{N_{SLM}}{N_{modes}} \simeq \frac{0.5 \cdot 140}{6} \simeq 11.5$$

which is close to the obtained experimental PA enhancement factor

$$\eta_{exp} = \frac{V_{PA}^{final}}{V_{PA}^{initial}} \simeq 6$$

The lower enhancement may be attributed to the following possible experimental aspects:

- the presence of noise in the measurements.
- the uneven contribution of the SLM pixels to the PA signal at a given position, leading to a lower effective number of degrees of freedom.
- the optical speckle decorrelation during the experiments: the PATM remains valid as long as the scattering sample is stable. If for any reason the scattering sample moves, either between the measurement of the matrix and the focusing operation or during the measurement of the matrix itself, the recorded information in the matrix will become partly inconsistent.

With the knowledge of such a transmission matrix, it should be noted that one is not limited to focusing on a single target and any intensity distribution on the targets can be generated, albeit with a lower contrast [Popoff 10b, Vellekoop 07].

We repeated the experiment using a scattering sample of ∼500 µm thick chicken breast tissue to demonstrate the validity of the technique when dealing with biological tissue. The results are presented in Fig. 2.6. In this experiment, the enhancement of the PA signal is lower compared to the previous one, which may be explained by the shorter decorrelation time of the fresh chicken sample compared to the optical diffuser.

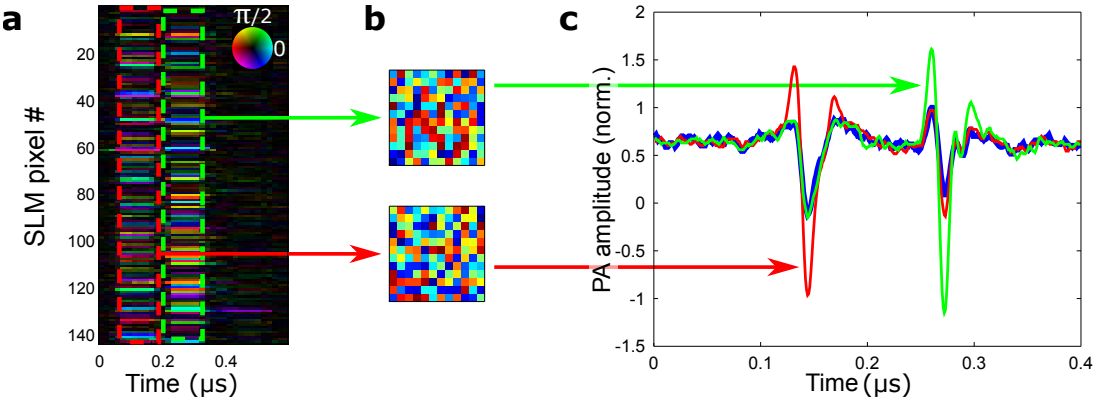

Figure 2.6 – Light focusing through biological tissue using the PATM. a) Measured transmission matrix through a chicken breast sample. Only two absorbing wires are in the focus of the transducer in this experiment. The red and green dotted rectangles highlight the matrix columns corresponding to two absorbing targets identified for focusing. b) The SLM phase masks for focusing on each of the absorbers are given by phase conjugating these transmission matrix columns. c) Measured photoacoustic signals when displaying either a flat phase on SLM (blue), the phase-pattern in (b) focusing on the first absorber (red), or the phase pattern in (b) focusing on the second absorber (green).

2.3.2 Retrieving scattering properties from the transmission matrix: the optical memory effect

It has been shown that the information encoded in the optical transmission (or in some cases reflection) matrix is much richer than the one required to focus light on a single or multiple targets. It can be for instance analyzed to separate single scattering from multiple scattering, as demonstrated in acoustics in [Aubry 09] or in optics [Kang 15]. The distribution of the singular values of the optical TM and the study of open and closed eigen channels are also of great interest [Goetschy 13, Popoff 14, Vellekoop 08b]. Moreover, the transmission matrix has been used to study the backscattering cone and spatial field correlations in mesoscopic physics [Mello 88, Sebbah 02]. Correlations in the matrix enable to retrieve another scattering property of the medium called the memory effect.

It has been already shown in the optical transmission matrix [Popoff 11b]. We experimentally demonstrate here that the same analysis can be carried out with the PATM to probe the scattering sample optical memory effect.

Principle

The memory effect denotes the fact that a multiply scattering sample of thickness L retains a range of isoplanatism: speckle patterns generated by plane waves at different incident angles θ_1, θ_2 are correlated as long as $\Delta\theta = \theta_1 - \theta_2$ is smaller than $\frac{\lambda}{2\pi L}$, where λ is the wavelength of the incident light [Freund 88]. This effect is also known in weakly aberrating samples as isoplanatism both in optics [Fried 82] and acoustics (see [Bossy 06] for instance in the context of PA imaging).

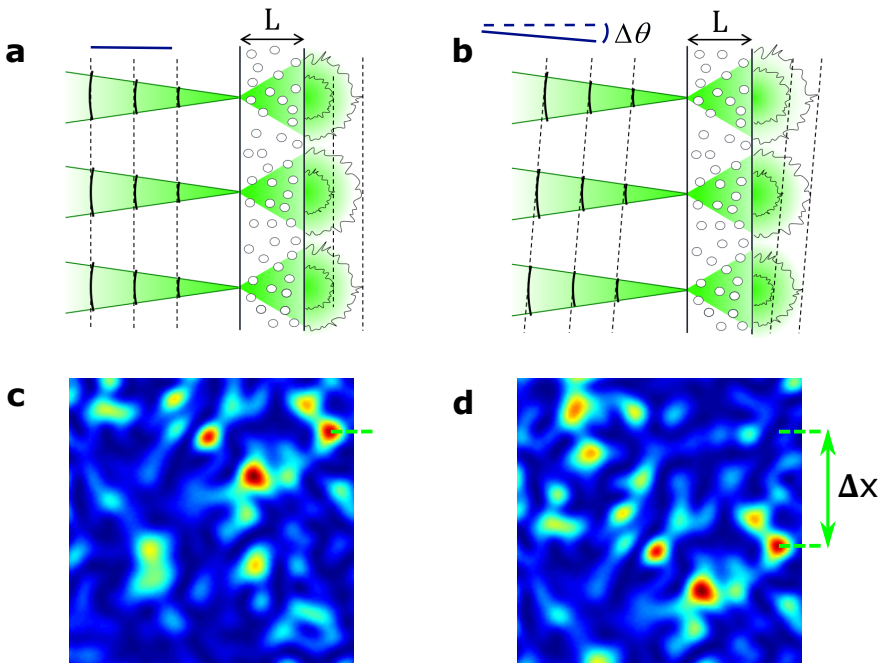

Figure 2.7 – Optical memory effect: principle. a) A plane wave illuminates a scattering layer of thickness L. It produces a specific phase pattern at the output of the layer. b) The incident plane wave is tilted by an angle $\Delta\theta \leq \frac{\lambda}{2\pi L}$. This tilt is preserved in the outgoing wavefront. c) Speckle pattern corresponding to outgoing wavefront in (a), as observed in far field. d) Speckle pattern corresponding to outgoing wavefront in (b), as observed in far field. It is strongly correlated to the speckle in (c), namely vertically translated, following the wavefront tilt in near-field.

Figure 2.7 illustrates this effect. Let us consider a plane wave impinging on the scattering medium. It produces a given phase pattern at the output of this medium (Fig. 2.7.a), leading to a specific speckle pattern in the far field after propagation in free space (Fig. 2.7.c). When the incident beam is tilted by $\Delta\theta$, this tilt is partially conserved at the output of the medium (Fig. 2.7.b), which leads to a shift of Δx of the speckle pattern in the far field (Fig. 2.7.d).

Results

In the measured PATM, as plotted in Fig. 2.4.c, each column i represents the SLM phase-pattern $\phi^{SLM,i}(x^{in}, z^{in})$ required to focus on a target at an axial distance $z_i^{out} = c_s\tau_i$ from the transducer, where x^{in} and z^{in} denote the spatial coordinates of the SLM pixels. If the different probed targets are within the sample memory effect range, the difference between each such two SLM phase patterns would be just the addition of a tilt, hence a linear phase-ramp (Fig. 2.8.b):

$$\phi^{SLM,i}(x^{in}, z^{in}) - \phi^{SLM,j}(x^{in}, z^{in}) = k_{ij,x}\ x^{in} + k_{ij,z}\ z^{in} + \phi_0 \tag{2.7}$$

where $\vec{k_{ij}} = (k_{ij,x}, k_{ij,z})$ is the wave-vector defining the additional required tilt. Thus, in the case of perfect correlations, the k-space representation of this difference between the input wavefronts, or similarly the transmission matrix columns, would be a delta-function at the relative tilt:

$$FT\left(e^{i\phi^{SLM,i}(x^{in},z^{in})}e^{-i\phi^{SLM,j}(x^{in},z^{in})}\right) \propto \delta(\vec{k} - \vec{k_{ij}}) \tag{2.8}$$

where FT stands for the Fourier Transform. In our experiment, where only angular correlations along the z direction can be probed, plotting the transmission matrix columns after subtraction of the first column phase would thus result in a diagonal matrix.
We performed this analysis on the experimental transmission matrix measured through a thin diffuser (Fig. 2.5) for a tilt along the z direction. The result are presented in Fig. 2.8. This reveals the k-space correlations of the transmission matrix columns, highlighting the memory effect expected from such a thin scatterer. The apparent wrapping of the large k-space components (k-space aliasing, or equivalently grating lobes) is a result of the low SLM-resolution used in this experiment (12x12 pixels).
As the output basis in the matrix presented in Fig. 2.8.c is the PA time-delay, which corresponds to vertical position, we are able to probe the memory effect only for a vertical tilt of the input beam, i.e. in k_z representation. The diagonal nature of the transmission matrix is characteristic of the memory effect, and denotes the fact that the scattering medium behaves the same for the different incident angles.

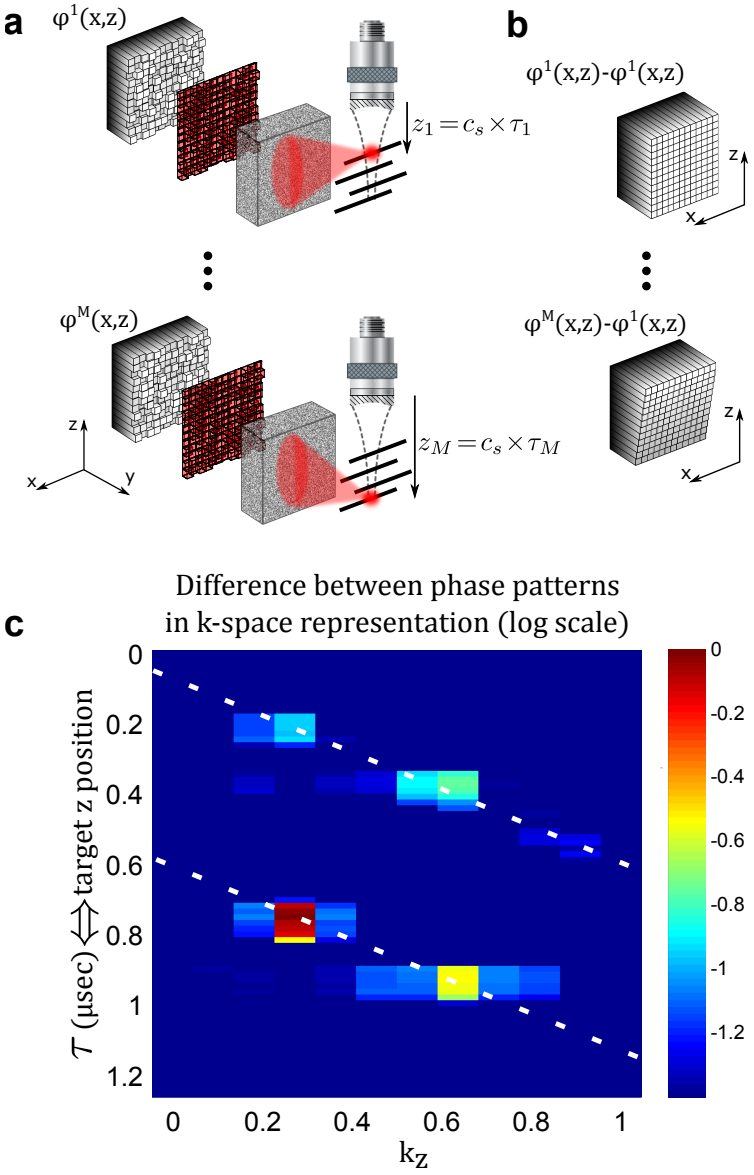

Figure 2.8 – Revealing the memory effect from the experimental photoacoustic transmission matrix. a) Each phase-conjugated m^{th} column of the PATM gives the SLM phase pattern required to focus on a target located at axial position z_m. In thin scattering samples, the angular memory effect for speckle correlations corresponds to a correlation between these transmission matrix columns. b) Within the memory effect range, two phase patterns focusing on two targets are related through a tilt, i.e. their phase difference is a shifted delta function in k-space representation. c) k-space representation of such phase difference analysis, performed on the experimental transmission matrix measured through a diffuser, revealing the memory effect correlations between the different targets expected for such a thin scatterer. Dashed lines represent the diagonal direction for a perfect memory effect and its k-space aliasing.

The information obtained through this analysis is equivalent to analyzing the electric field correlations between the fields propagating from these targets through the medium. This can be seen directly from Eq. (2.8) using the convolution theorem:

$$\begin{aligned} FT\left(e^{i\phi_i^{(SLM)}(x,z)}e^{-i\phi_j^{(SLM)}(x,z)}\right) &= FT\left(E_i(x,z)E_j^*(x,z)\right) \\ &= corr\left(\widetilde{E}_i(k_x,k_z)\widetilde{E}_j^*(k_x,k_z)\right) \end{aligned} \tag{2.9}$$

This memory effect is important not just because it is a mesoscopic property of the medium [Akkermans 07], but as it can serve to scan the focus obtained by wavefront-shaping [Hsieh 10a, Vellekoop 10b] and allow imaging within its range [Bertolotti 12, Katz 14, Katz 12]. However, it is beneficial as long as it enables to scan a given pattern over a distance larger than one speckle grain diameter. It is then mostly useful for thin scattering media. In biological tissue yet, a recent study showed that the memory effect range for chicken breast and rat brain samples was somehow larger, up to an order of magnitude, than what was expected with the knowledge of their thickness [Schott 15, Judkewitz 15]. This work holds the promise of potential use of memory effect-based imaging techniques at depth of a few hundred micrometers in biological tissue.

2.3.3 Targets localization using singular value decomposition

A powerful tool in the analysis of the scattering matrix is the singular value decomposition (SVD). Recently, SVD of the optical transmission matrix was used to identify transmission eigenchannels [Popoff 10b] and maximize energy transport in multiply-scattering samples [Kim 12]. SVD of the backscattering-matrix was also utilized to discriminate and selectively focus on individual nanoparticles through aberrating media [Popoff 11a], a result analogous to works done in ultrasound [Prada 94, Prada 96]. Here we show that, similarly, the SVD of the PATM enables the identification and discrimination of individual absorbing targets. It furthermore provides the wavefronts required for selective focusing without any a priori information on the targets' number or positions. To this end, we compute the SVD of the PATM measured through a diffuser. We present the results of this analysis in Fig. 2.9.

Performing a SVD of a matrix T consists of writing $T = U\Sigma V^*$, where Σ is a rectangular diagonal matrix containing the real positive singular values ℓ_i, in descending order, and U and V are unitary matrices whose columns corresponds to the output and input singular vectors, U_i and V_i, respectively. In the case of the PATM, each input singular vector V_i corresponds to the SLM phase-pattern for focusing on a target having the PA modulation intensity ℓ_i.

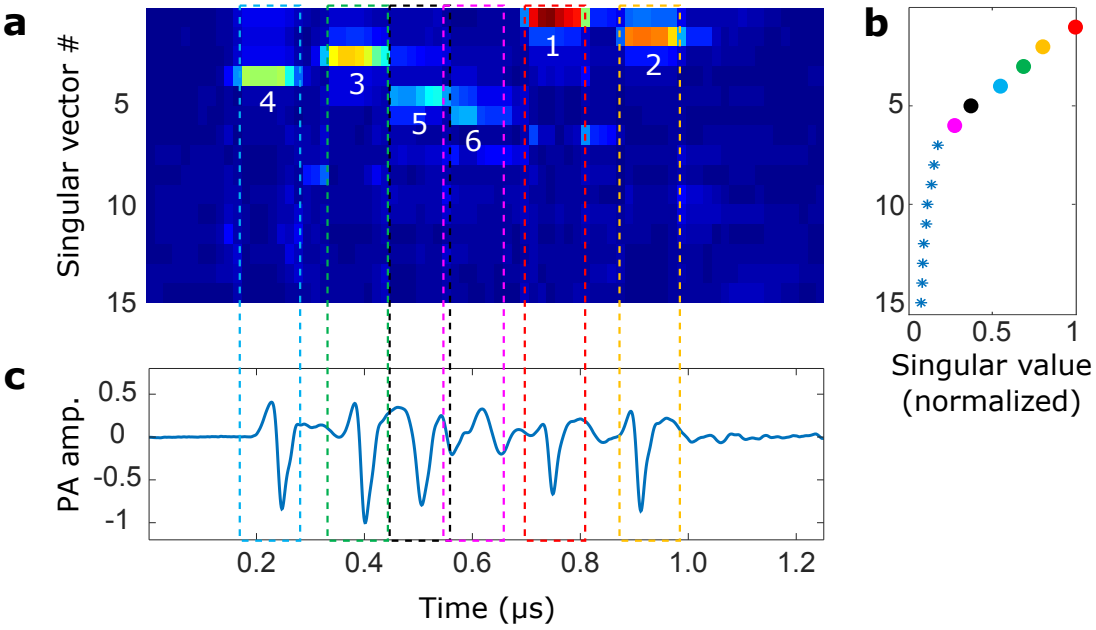

Figure 2.9 – Localizing absorbing targets by singular value decomposition of the PATM. a) First 15 output singular vectors U_i , weighted by their corresponding singular values ℓ_i. b) First 15 singular values ℓ_i. A few singular values (colored circles) rise above a continuum of background-noise singular values (blue stars). c) Photoacoustic time trace (averaged over several laser pulses) with flat SLM, showing an excellent correspondence between the output singular vectors in (a) and the time delays where absorbing targets can be visually identified.

The corresponding output singular vector U_i is the expected PA modulation temporal trace for this singular value, i.e. the corresponding absorber position (Fig. 2.9.a). Plotting the obtained singular values in descending order (Fig. 2.9.b), one can identify that their distribution exhibits two parts. A continuum of low singular values associated with background noise, and a few higher singular values, which are associated with strong absorbing targets (highlighted by colored circles in Fig. 2.9.b). Plotting the output singular vectors, U_i, which correspond to these singular values, reveals temporally localized PA responses for the large singular values (Fig. 2.9.a). This shows that the SVD can be used to give the positions of the absorbing targets within the limitation of the ultrasound resolution, i.e. one absorbing target per ultrasound resolution cell. In particular, it enables to clearly separate absorbers 5 and 6 in Fig. 2.9.a, which are not fully distinguishable on the PA trace Fig. 2.9.c. The two acoustic pulses indeed overlap with each other rebounds, but they are not modulated in the same manner. SVD of the PATM clearly reveals this aspect and enables to unambiguously separate them. Such an approach advantageously replaces the subjective imprecise visual inspection of the transmission matrix used to select the time-delays for focusing in Fig. 2.5. The corresponding input singular vectors V_i can be displayed on the SLM to guide light to these targets [Popoff 11a, Prada 94, Prada 96].

2.4 Photoacoustic Transmission Matrix with two-dimensional photoacoustic imaging setup

Up to this point, one-dimensional PA images were acquired using a single spherically focused ultrasonic transducer, thus limiting the applicability of the technique to a narrow field-of-view and requiring mechanical scanning to expand it. In this section, we present an extension of the PATM method to a two-dimensional PA imaging setup using a linear ultrasound array.
With two-dimensional PA images, the PATM describes the complex influence of the optical input modes (SLM pixels) on the acoustic output modes,i.e. the intersection between each acoustic resolution cell in the PA image and the absorbing structures. Light focusing is once again demonstrated here through scattering phantoms on a complex absorbing structure.

2.4.1 Experimental procedure

The illumination setup is very similar to the one described in section 2.2.1. The spatially-shaped pulse passes through a scattering sample (120 Grit ground glass diffuser, Thorlabs). This diffuser is a surface scatterer as well, and scatters mostly in the forward direction (output angle: +/- 10 degrees). In this study, we use a black leaf skeleton as the absorbing target (Fig. 2.11.a) [Jose 12, Huang 13]. This sample contains branching structures with multiple orientations and various spatial scales, ranging from 50 µm to 200 µm. The gel supporting the sample is weakly optically scattering, and does not affect significantly the incident speckle. The gel also mechanically mimics the speed of sound in biological tissue. This two-dimensional sample is located in the imaging plane and in the vicinity of the elevation focus of a linear ultrasound array (128 elements, 14.4 MHz center frequency and pulse-echo -6 dB bandwidth of 6.8 MHz, 0.1 mm pitch and elevation focus of 8 mm, Vermon), connected to a commercial ultrasound scanner (Aixplorer, Supersonic Imagine). According to Eq. 1.23, the corresponding imaging resolution is approximately: $\Delta x = 65$ µm, $\Delta z \simeq 220$ µm. After each laser shot, the photoacoustically-induced ultrasonic waves are measured simultaneously by all the elements of the array. The intensity fluctuations of the laser are monitored with a photodiode, and are used to normalize the measured photoacoustic signals. The acquired PA signals are averaged over 10 laser pulses to improve the SNR. The averaged signals are then filtered with a digital third-order Butterworth lowpass filter having a cutoff frequency of 25 MHz. The PA image is reconstructed with a standard backprojection algorithm [Xu 05] (see section 1.5.3), using a pixel size of 25 µm to match the sampling rate of the ultrasound scanner.

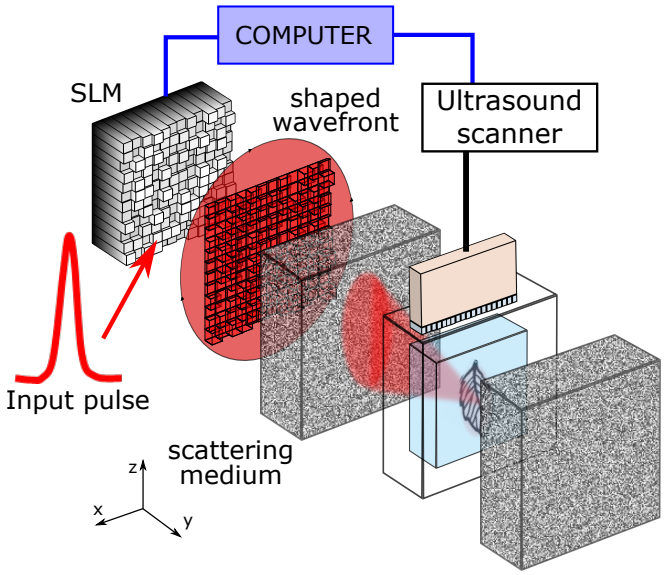

Figure 2.10 – PATM measurement using a two-dimensional photoacoustic imaging setup. A nanosecond laser pulse is shaped by an SLM before passing through a thin scattering sample and illuminating an absorbing structure. Photoacoustic signals are detected with an ultrasonic linear array, driven by an ultrasound scanner.

To acquire the PATM, we used the exact same procedure described in section 2.1. The influence of each of the controllable input modes (SLM pixels) on each of the PA image pixel is measured by varying the phase of each input mode (in the Hadamard basis) from 0 to 2π in 8 steps (compared to 16 in the previous section). A two-dimensional PA image is acquired for each input SLM phase pattern. When varying each SLM input pattern phase from 0 to 2π, the intensities values of the PA image pixels vary according to the cosine of the applied phase. The elements of the PATM are obtained directly by analyzing these cosine modulation phases and amplitudes. To improve the SNR and better match the acoustic resolution, we analyze the modulation of the maximum intensity values $V^k_{PA,n}(x,y)$ computed within 125×125 µm^2 areas, rather than on single pixels, which are considerably smaller:

$$V^k_{PA,n}(x,y) = max\left(Im^k_n(x \pm 2 \text{ pixels}, y \pm 2 \text{ pixels})\right)$$

where Im^k_n is the PA image measured while phase-shifting the n^{th} input mode on the SLM by ϕ^{SLM}_k, and (x,y) are the coordinates of the central pixel of the analyzed area (in pixel unit).
A typical PA image is presented in Fig. 2.11.b, and the corresponding envelope image is shown in Fig. 2.11.c, obtained by computing the modulus of the analytic signal representation of each column (z-axis) of Fig. 2.11.b. Here, these images were computed by averaging all the images acquired during the matrix measurement process, corresponding to the hundreds of speckle illuminations

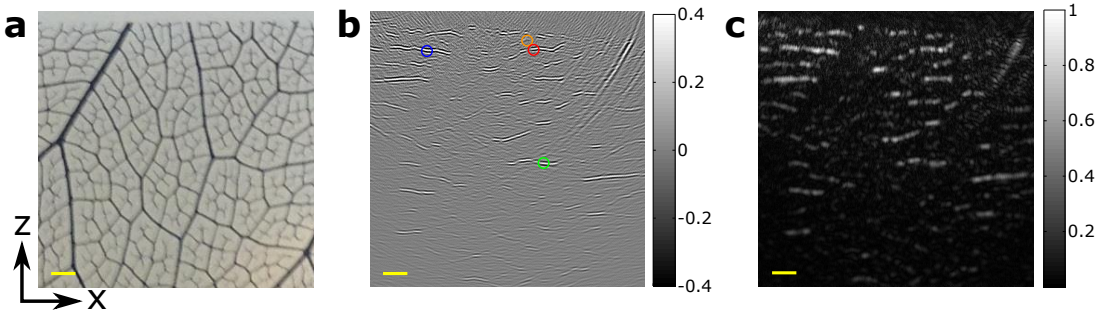

Figure 2.11 – Two-dimensional photoacoustic imaging. a) Reference photograph of the absorbing leaf skeleton embedded in an agarose gel block. b) Standard photoacoustic image similar to that obtained with uniform illumination. The colored circles indicate the position of the foci presented in the next figures. c) Envelope of the PA image in (b). Scale bars: 1 mm.

created by the successive SLM phase patterns. As speckle statistics ensures that the sum of many uncorrelated speckle patterns gives a uniform intensity image [Goodman 07], and thanks to the linearity of the image reconstruction algorithm (see section 1.5.3), this image shows the PA image that would be obtained under homogeneous illumination. From the photograph shown on Fig. 2.11.a, it is clear that Figs. 2.11.b and c only reveals the horizontal (x-axis) structures of the sample. This feature is a standard artefact in PA imaging, due to the finite aperture of the transducer array [Xu 04]: elongated absorbers emits acoustic energy mostly perpendicularly to their main orientation, and therefore only PA waves emitted from horizontal elements reach the ultrasound array. Imaging artefacts will be further developed in the fourth chapter.

2.4.2 Light focusing

We investigate here the light-focusing capability of this PATM at an arbitrary position on the absorbing structure. We apply the exact same transmission matrix columns phase conjugation technique than in section 2.3.1. The results of focusing on three arbitrary targets on the leaf skeleton fibers are shown in Fig. 2.12. Quantitatively, the signals of the reconstructed photoacoustic image were locally increased by a factor of 6.2 (red target, Fig. 2.12.b), 3.4 (blue target, Fig. 2.12.e), and 5.2 (green target, Fig. 2.12.h). This PA enhancement factor is defined as the ratio between the maxima over the targeted area (colored square, $125{\times}125$ µm^2) of the enhanced (when applying focusing pattern on the SLM) and mean (mimicking uniform illumination) PA images. These ratios are again within the order of magnitude of the expected enhancement of the optical intensity: $\eta = 0.5 \times N_{SLM}/N_{speckles}$.

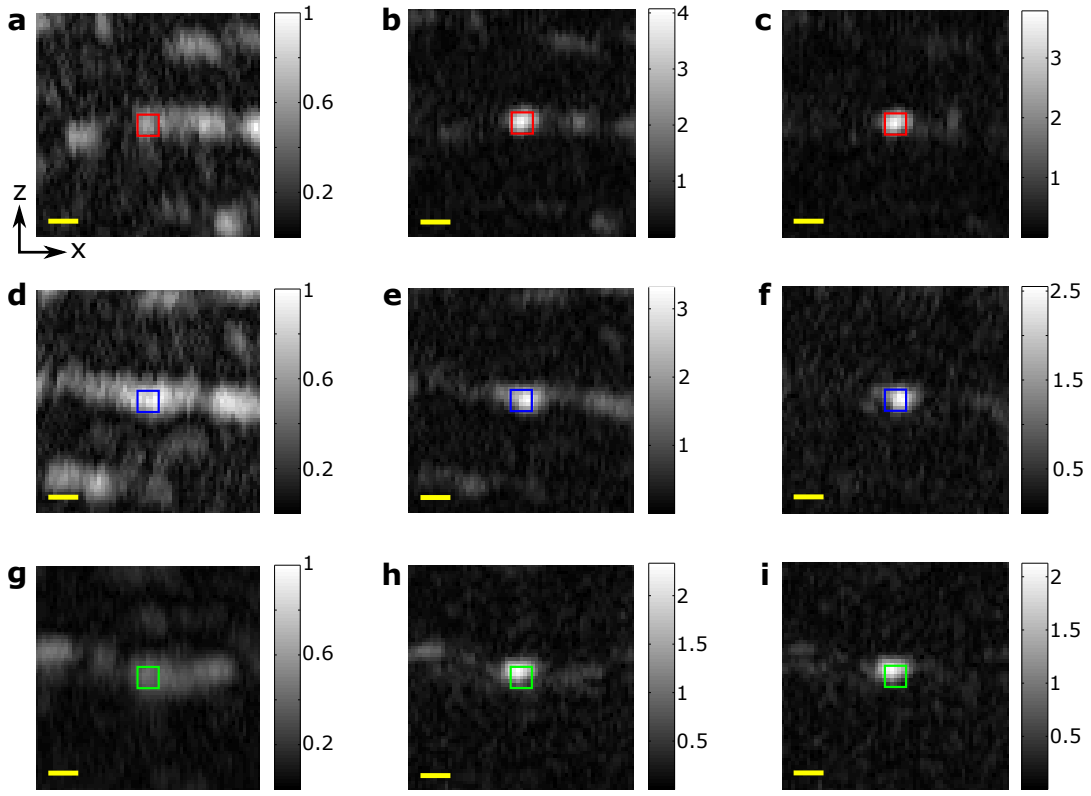

Figure 2.12 – Light focusing using the PATM with 2D photoacoustic imaging. a) Envelope of the mean photoacoustic image (zoom of Fig. 2.11.c). b) Envelope of the photoacoustic image when displaying the focusing phase pattern on the SLM. c) Envelope of the difference between the photoacoustic images corresponding to (b) and (a) (the difference is computed before the envelope). (d,e,f) and (g,h,i) are analog to (a,b,c) for different target positions. All photoacoustic images are normalized by the maximum value of Fig. 2.11.c. The colored squares indicate the areas over which the modulation of the photoacoustic signal was measured. The colors correspond to the positions marked on Fig. 2.11.b. Scale bars: 200 µm.

Here, the distance between the scattering sample and the absorbing structure yielded 25 µm diameter speckle grains on the absorbing structure. The size of the targeted acoustic resolution cells is 125×125 µm^2. $N_{speckle}$ is thus assessed to be around 25, leading to an expected optical enhancement factor around 3. We compute $N_{speckles}$ as a ratio of areas, because the speckle are elongated along the light propagation axis. Moreover, the elevation resolution of the transducer-array is not taken into account here because the absorbing sample is fully contained in the elevation focal zone. However this calculation should be also valid when considering a three-dimensional speckle in depth as previously mentioned.
The higher experimentally measured enhancement of the PA signal is attributed to the fact that absorbing targets are actually smaller than 125×125 µm^2 and are therefore illuminated by less speckle grains.

2.4.3 Light focusing on invisible structures

In the results presented in Fig. 2.12, we have selected noticeably bright points on the standard PA image as target points, meaning that focusing was obtained only on rather horizontal veins of the leaf skeleton. However, using the PATM, light focusing and control can be exerted on "invisible" vertical structures as well. This invisibility is due to the directionality of the ultrasonic waves emitted by elongated absorbers. When such an absorber is perpendicular to the detector surface, most of the emitted ultrasounds do not reach the detector, and the absorber cannot be reconstructed in the PA image. This imaging artefact will be further discussed in the fourth chapter of this thesis.
In Fig. 2.13, we demonstrate the focusing on one absorber portion that is invisible on Fig. 2.11.c. The underlying reason is that, even though the pixel values are close to the noise floor around the target point in the standard PA image (Fig. 2.13.b), the modulation of the PA signal can clearly be measured when shifting the phase of the SLM input modes, as illustrated in Fig. 2.13.b. We are thus able to focus at this location using the same phase-conjugation focusing procedure. The corresponding result is shown in Fig. 2.13.c,d.

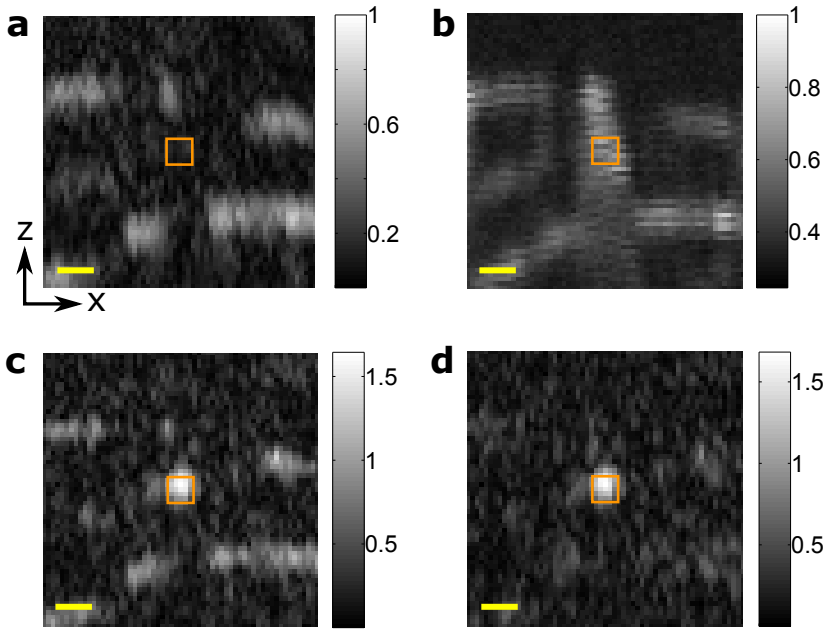

Figure 2.13 – Focusing on *invisible* regions: a) Envelope of the mean photoacoustic image (zoom of Fig. 2.11.c). b) Average of transmission matrix modulus over the input modes. c) Envelope of the photoacoustic image when displaying specific focusing phase pattern on the SLM. d) Envelope of the difference between the photoacoustic images in (c) and (b). Scale bars: 200 µm.

We shall see in the fourth chapter of this thesis that such modulation image enables to overcome usual artefacts of limited-view PA imaging.
Focusing on these structures might also be possible using the memory effect in the case of a thin diffuser after focusing on neighbouring visible target, as performed in [Vellekoop 10b] with fluorescence. Nonetheless, we emphasize here that despite a PA signal close to noise level due to limited-view detection, the local fluctuations of the PA signal are sufficient to retrieve the focusing phase mask. Focusing is thus enabled even on hidden target located far from standard visible structures, and thus out of reach of any focusing procedure using the memory effect along with optimization.

2.5 Discussion

We demonstrated a non-invasive approach able to optically interrogate a large number of absorbing targets and selectively focus light through (and potentially inside) scattering media, using alternatively two standard PA imaging setups. The advantage of the presented approach is its generality. In particular, we demonstrate that it can be performed regardless of the PA imaging system, using in turn a single ultrasonic transducer or a standard array of transducers, the latter enabling to control light focusing over a large field-of-view without any mechanical scanning process, by parallelizing the acquisition of the output modes. An additional advantage of this technique is its simple experimental implementation. It employs a standard PA imaging setup and does not require a reference arm, careful timing of acoustic and optical pulses, or precise positioning of the SLM as required in acousto-optics experiments (see for instance the experimental setups in [Judkewitz 13] and [Xu 11]).
While our proof-of-principle demonstrates focusing through scattering samples, the proposed approach could similarly be applied to focusing inside scattering media, provided that the modulation amplitude exceeds the noise threshold of the detection. Although the focusing dimensions reported here were limited by the PA imaging resolution, interestingly, in the case of an isolated small absorber, light could be concentrated onto the absorber, in principle down to the optical speckle-grain dimensions. Interestingly, all wavefront-shaping techniques can be seen fundamentally based on characterizing a transmission matrix. In both optimization [Kong 11] and acousto-optic tagging (TRUE) approaches [Xu 11], a single output mode is targeted and a single row ("vector") of the transmission matrix is acquired per acquisition sequence. TROVE has the additional advantages that it essentially measures a whole matrix and with optical resolution [Judkewitz 13]. In all these techniques, the acquisition time scales with the number of targets or resolution cells, while in the PATM approach presented in this chapter, the measurement time depends only on the number of input modes. It is

important to note that unlike acousto-optic techniques, photoacoustics requires the presence of an absorber. However, absorption is perhaps the most common optical contrast mechanism, it is present in all fluorescent markers [Razansky 09], and often also in unstained tissues. As such, it is the basis for the very large field of PA biomedical imaging [Wang 12, Xu 06, Zhang 06]. Although the PATM enables to deliver light only to locations where absorption is present, these are exactly the positions that are targeted by laser therapy [Hirsch 03] and fluorescence imaging techniques.
In addition, we have demonstrated the capability to focus on segments hidden in the conventional PA image, using the modulation image to select the target points. We note that the PATM method suits well the study of complex absorbing samples, as it enables a clear identification of the targets regardless of their orientation relatively to limited-view acquisition and allows to locally enhance PA signals. We used PA feedback to perform light focusing potentially at depth, but the method could also benefit the field of PA imaging: while PA imaging is now a mature technique for tissue imaging at large optical depths, it currently relies on diffuse homogeneous illumination. Our method enables to spatially tailor the illumination to the regions of interest, opening the possibility to reveal features at even larger depths and with reduced light exposure levels.

Several challenges emerge for practical application in deep tissue imaging (see Fig. 2.14). The first is related to the fast decorrelation of optical speckle patterns inside tissue (see Fig. 2.14.a). Acquisition time of the PATM should then be further reduced to allow light control in biological sample.
In this work, the matrix acquisition time was about a few tens of minutes. It was mainly limited by the repetition rate of the laser (10 Hz) and the signal to noise ratio. Using higher repetition rates lasers and fast SLMs with a higher optical energy damage threshold is expected to significantly reduce the acquisition time, potentially reaching the sub-second acquisition times of the optical transmission matrix. Because the total acquisition time is dictated by the number of measurements per input mode and the number of controlled input modes, a trade-off exist between the acquisition time and focusing efficiency. It should be however highlighted that only limited fluence can be used for tissue application. According to the European standard EN 60825-1, fluence should be maintained below 20 $mJ.cm^{-2}$ for nanosecond pulse. This will obviously limit the amount of PA signal that can be generated and should be taken into account. In this regard, the PATM could conversely be used to locally deliver a high fluence in depth, while remaining below the 20 $mJ.cm^{-2}$ threshold for most of the tissue. This could be for instance used to locally burn undesirable pieces of tissue, while preserving the surrounding.

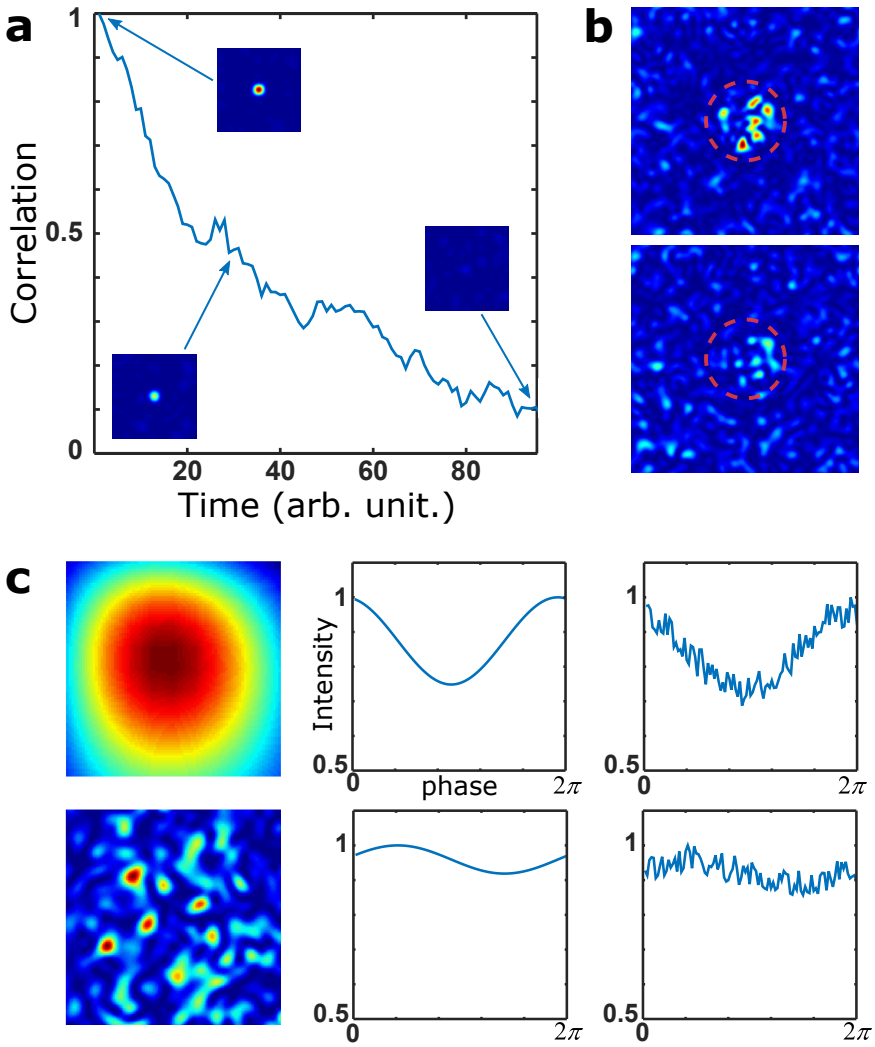

Figure 2.14 – Challenges to measure the photoacoustic transmission matrix deep inside tissue (simulations). a) Correlation of speckle patterns when measured through a decorrelating sample. Insets: the focusing phase mask is displayed on the SLM and the resulting speckle pattern is shown at different times, highlighting the decrease in the focusing efficiency. b) Speckle patterns after optimization of the total light intensity within the red dotted circle, using either 196 SLM pixels (top) or 98 SLM pixels (bottom). c) When integrating the light intensity (left) of one (top) or several speckle grains (bottom), the modulation of the total intensity (middle) is more or less contrasted. In the presence of noise (right), small modulations are barely measurable.

The second challenge is to bypass the large mismatch between the optical resolution (i.e. the speckle grain diameter) and the acoustic resolution. In order to focus with high efficiency inside scattering samples, one has to maintain a high ratio between the number of controlled degrees of freedom and the number of optical modes on each target within one acoustic resolution cell (see Fig. 2.14.b). Given the sub-micron diffraction-limited dimensions of optical modes inside tis-

sues, this goal can be met by the combined use of a high resolution SLM, a sparse distribution of absorption within the ultrasound resolution cell and a high-frequency and large aperture acoustic detection system to shrink down the acoustic resolution. However a smaller absorbing particle would emit less energy and in a higher frequency band. If one uses the exact same setup as described in section 2.2.1, the detected signal would be decreased both because of the lower amplitude of the acoustic signal emitted by the particle and because of the higher attenuation due to the limited bandwidth of the detection. The instrumentation should then be carefully adapted. Given a fixed number of speckle grains per acoustic resolution cell, i.e. a fixed expected enhancement ratio, the following challenge is to measure the small modulations of the PA signal from an acoustic resolution cell containing a large number of optical speckle grains (see Fig. 2.14.c). In our experiment, the SNR limits this number to approximately a hundred speckle grains per acoustic cell. In order to reduce the number of speckle grains per acoustic resolution cell, an approach involving high ultrasonic frequencies selection will be presented in the next chapter, and a few other solutions proposed in the literature will be reviewed in the conclusion of this thesis.

Chapter 3

Spectrally filtered photoacoustic feedback for iterative wavefront shaping

Contents

Light focusing via photoacoustic-guided wavefront shaping has been first demonstrated by Kong and colleagues in 2011 [Kong 11]. A photoacoustic signal generated by graphite particles was used to monitor the speckle field intensity behind a scattering layer. By iteratively optimizing the peak-to-peak amplitude of this signal, they were able to focus light, enhancing the photoacoustic signal by a factor ranging typically from 5 to 10. To better understand what limits this focusing efficiency, we shall first re-examine the all-optical experiment as described in [Vellekoop 07, Vellekoop 10a, Popoff 10b]. In these works, the entire speckle pattern can be imaged and resolved using a camera. When optimizing the intensity on a large area, the efficiency of the optimization process is driven by the number of speckle grains that are simultaneously enhanced [Vellekoop 07]. To quantify this efficiency, the enhancement factor η_{optic} is defined as the ratio between the mean intensity of the optimized area and the mean background intensity, which is close to the mean intensity before optimization (if the total number of speckle grains is large enough compared to the number of controllable degrees of freedom (SLM pixels) N_{SLM} [1]). It has been shown that this enhancement is given by:

$$\eta_{optic} \simeq 0.5 \times \frac{N_{SLM}}{N_{speckle\ grains}}, \tag{3.1}$$

where $N_{speckle\ grains}$ is the number of optical modes (speckle grains) whose total intensities are simultaneously optimized [Vellekoop 08c, Popoff 11b].
The total energy that can focused is limited by the number of SLM pixels: when simultaneously optimizing the light intensity of several speckle grains, this energy is spread over these grains (see Fig. 3.1). Hence, the larger the optimized area, the lower the enhancement. As long as the feedback signal is proportional to the sum of the light intensities of several speckle grains, it makes no difference if all the energy is concentrated within one single speckle grain or spread over several grains, provided that all speckle grains are similarly weighted.

[1] Let N be the total number of speckle grains and I the total intensity. The intensity per speckle grain in the initial image is therefore: $I_{init} = \frac{I}{N}$, assuming energy conservation. After optimization of one speckle grain intensity, considering that N_{SLM} degrees of freedom are available, the intensity of the targeted speckle grain is: $\frac{I}{N}N_{SLM}$. The intensity of the $N-1$ remaining grains is then: $\frac{1}{N-1}(I - \frac{I}{N}N_{SLM}) =\simeq \frac{I}{N} = I_{init}$ if $N_{SLM} \ll N$.

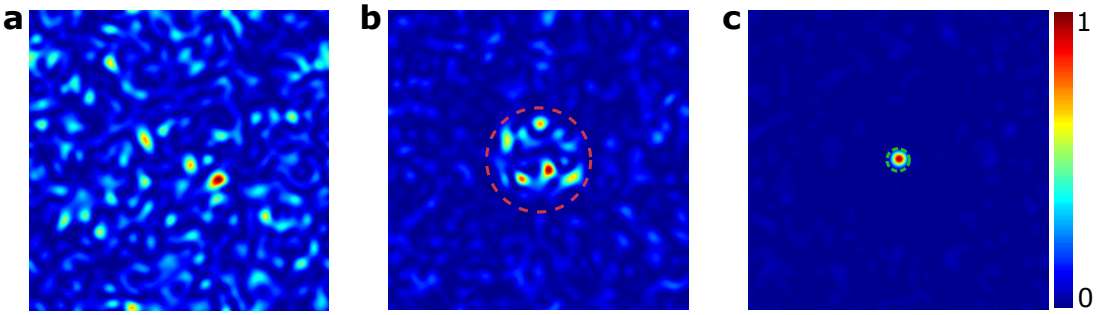

Figure 3.1 – Influence of the optimized area (simulations). a) Speckle pattern in the case of a flat input wavefront. b) Speckle pattern after optimization of the total intensity over the large area delimited with the red dotted line. Around 20 speckle grains are simultaneously optimized. c) Speckle pattern after optimization of the intensity over the small area delimited with the green dotted line.

This explains why the speckle grain resolution cannot be achieved by optimizing the light intensity over a large area, i.e. containing several speckle grains, as in [Vellekoop 08c, Xu 11] or in the second chapter of this thesis. When using a photoacoustic feedback signal in the optimization process, the optical speckle grains are usually smaller than the acoustic resolution, driven by the acoustic frequencies of the detected signal. Typical acoustic frequencies used in photoacoustic imaging are in the 10 MHz range, which gives a typical resolution on the order of 100 µm, whereas the diffraction-limited speckle grain width is on the order of 1 µm deep inside tissue. Considering this large mismatch between the optical and acoustic resolutions, the size of the optical focus after optimization is expected to be linked to the acoustic resolution. The optical intensity enhancement over the probed volume is expected to drop in proportion to the number of independent speckle grains contained in the acoustic focus.

One could use smaller absorbers in order to reduce the effective number of probed speckle grains, as the photoacoustic signal is both proportional to intensity and absorption. Sparse absorption distributions could also be obtained using contrast agents at rather low concentration. However, inside tissue, one will likely deal with extended absorbers (larger than the acoustic focus in at least one dimension), such as blood vessels [Zhang 09]. A second solution is to use non-linear PA signals, building on non-linear fluorescence optimization works [Katz 11, Katz 14, Lai 15]. Focusing light down to the single speckle grain becomes then advantageous in the optimization process. This approach will be described in detail in the conclusion of this manuscript.

Another straightforward strategy is to reduce the size of the acoustically probed volume. Photoacoustic signals are inherently broadband [Beard 11], and spectral information can be extracted if the signal is recorded with a broadband transducer [Omar 14].

When considering the full detection bandwidth, the dimensions of the focal region of a spherically-focused acoustic transducer are usually assessed using the center frequency f_c. Its transverse width (-3 dB) is then given by:

$$\varnothing_{acoustic} \simeq \frac{F c_s}{f_c D}, \tag{3.2}$$

where F is the focal length of the transducer, D its diameter and c_s the speed of sound in water. However, different ultrasonic frequencies probe different focal volumes: the higher the frequency, the smaller the volume. For each frequency component of the measured acoustic signal, the probed volume scales with the same equation. This has already been used in photoacoustic imaging to reveal structures at different levels of resolution [Omar 14].

In this chapter, we investigate the role of the frequency content of the photoacoustic feedback signal on the optical focusing capabilities of an iterative optimization wavefront shaping process. We specifically investigate the effect on the enhancement of the PA signal generated by an extended linear absorber and on the size of the resulting optical focus, considering the use of a single broadband high frequency spherically-focused ultrasonic transducer. We exploit such spectral information by performing several optimizations of different frequency bands of the photoacoustic spectrum. We show in particular that the optimization of the highest detectable frequencies leads to a tighter focus compared to the standard optimization of the peak-to-peak amplitude of the PA signal, which contains a very broadband information, and probes an ill-defined acoustic volume.

This chapter is adapted and extended from:
Chaigne, Gateau, Katz, Boccara, Gigan & Bossy, *Improving photoacoustic-guided optical focusing in scattering media by spectrally filtered detection*, Optics letters, 2014 [Chaigne 14b]

3.1 Experimental setup

The experimental setup is similar to the one described in section 2.2.1, and is presented in Fig. 3.2. Considering the center frequency of the transducer, the width (-3 dB) of the focal zone is equal to: $\varnothing_{acoustic} = \frac{F c_s}{f_c D} \simeq 110$ µm, where f_c=28 MHz is the center frequency of the transducer, F=8 mm is the focal length of the transducer, D=4 mm its diameter and c_s=1480 m.s^{-1} the speed of sound in water. As this transverse width is inversely proportional to the acoustic frequency [Kino 87], it can therefore be controlled by appropriate filtering of the acoustic signal. We chose to place the absorber (black nylon wire,

30 µm in diameter) along the y direction, perpendicular both to the laser beam propagation direction and the transducer axis, one portion lying in the middle of the acoustic focus (see Fig. 3.2). In this configuration, the efficient absorbing area is reduced if the width of the acoustic focal zone is narrowed.
In order to strengthen our proof of principle, we image the speckle pattern in the plane of the absorber to monitor the optical focal spot resulting from the optimization. We thus place a beam splitter right after the diffuser and image the corresponding plane on a CCD camera (Manta G-046B/C, Allied Vision Technologies) using a 4-f setup. The width of the speckle grain is set to 25 µm.

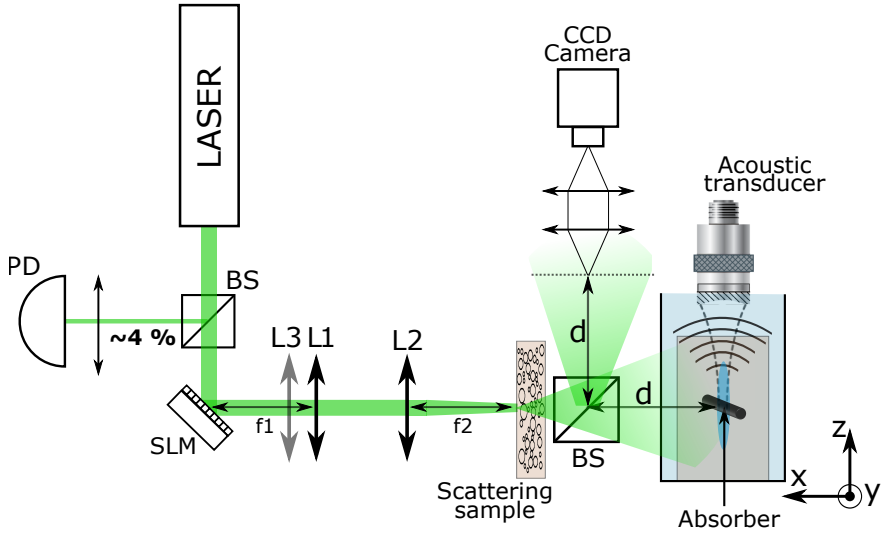

Figure 3.2 – Experimental setup. A nanosecond pulsed laser illuminates an SLM. The SLM is conjugated with the scattering sample. The scattered light illuminates a 30 µm diameter black nylon wire, located within the focal zone of a spherically-focused single element transducer. By inserting a beam-splitter between the scattering sample and the absorber, the speckle illuminating the wire is optically imaged using a CCD camera. PD: photodiode; L1, L2, L3: lenses; BS: beam-splitter.

For each laser pulse, the PA signal is amplified and measured by a computer-controlled oscilloscope, giving a temporal PA trace. The signal is normalized by the power of the laser pulse (monitored with a photodiode) to compensate for the pulse-to-pulse fluctuations of the laser. The Fourier transform of the signal is computed and the RMS (root mean square) value calculated in the frequency domain over a selected bandwidth (or alternatively the peak-to-peak value of the PA temporal signal) was used as the feedback value for the iterative optimization algorithm. We used different bandwidths: from 10 to 25 MHz, from 25 to 40 MHz, from 40 to 55 MHz, and from 55 to 70 MHz, where the SNR was sufficient to enable the optimization. This partitioning is arbitrary, and any band can be used as long as it contains sufficient energy to emerge from the background noise.

3.2 Optimization procedure

To focus light using PA feedback, we implemented the following iterative optimization method. We sequentially shift the phase of a set of wavefront patterns that form a basis of the optical input modes on the SLM. We use a Hadamard-based partition of the SLM pixels instead of the canonical one (i.e. pixel-by-pixel). This allows for a larger modulation of the feedback signal (half of the total number of SLM pixels are modulated at each step) and a faster convergence than the random partition introduced in [Vellekoop 08a] (see appendix A).
Hereafter we describe the n^{th} optimization iteration, illustrated in Fig. 3.3:

- Half of the SLM pixels are selected according to the n^{th} Hadamard vector: the phase of the SLM pixel i will be shifted during this step if the element of index i of the current Hadamard vector is equal to 1.

- the phase of the selected pixels is swept from 0 to 2π in 8 steps, modulating the speckle pattern that illuminates the absorbing sample. This results in a modulation of the measured PA feedback signal according to Eq. 2.3 of the second chapter. This modulation is analyzed according to equations 2.5 to extract its phase and amplitude.

- the phase that maximizes the feedback signal is then attributed to the SLM pixels, and these operations are iterated with the following Hadamard vectors.

Each of these iterations requires a minimum of 3 phase steps, according to Nyquist theorem. In a noisy environment, it is preferred to increase the sampling rate (8 phase steps here) to prevent large errors in the phase estimation. A similar way to reduce phase estimation errors is to average several PA signals for a given phase mask on the SLM. However, this is not fully equivalent in our situation because of temporal jitters of the PA signals. The average PA signal is then artificially low-pass filtered, which would strongly impairs our experiment since it heavily relies on the spectral content of this PA signal.
The phase of the SLM is updated after each iteration to steadily enhance the PA signal from the beginning of the optimization. It allows more accurate phase measurements since the PA signal quickly steps above the noise level. However, this leads to a slight phase drift of the reference field during the optimization (see Fig. 1.17.d). We then need to span the Hadamard basis several times to reach the optimal focusing phase pattern. Experimentally, we use 640 steps (four times the number of input modes) to ensure that the optimization properly converged.

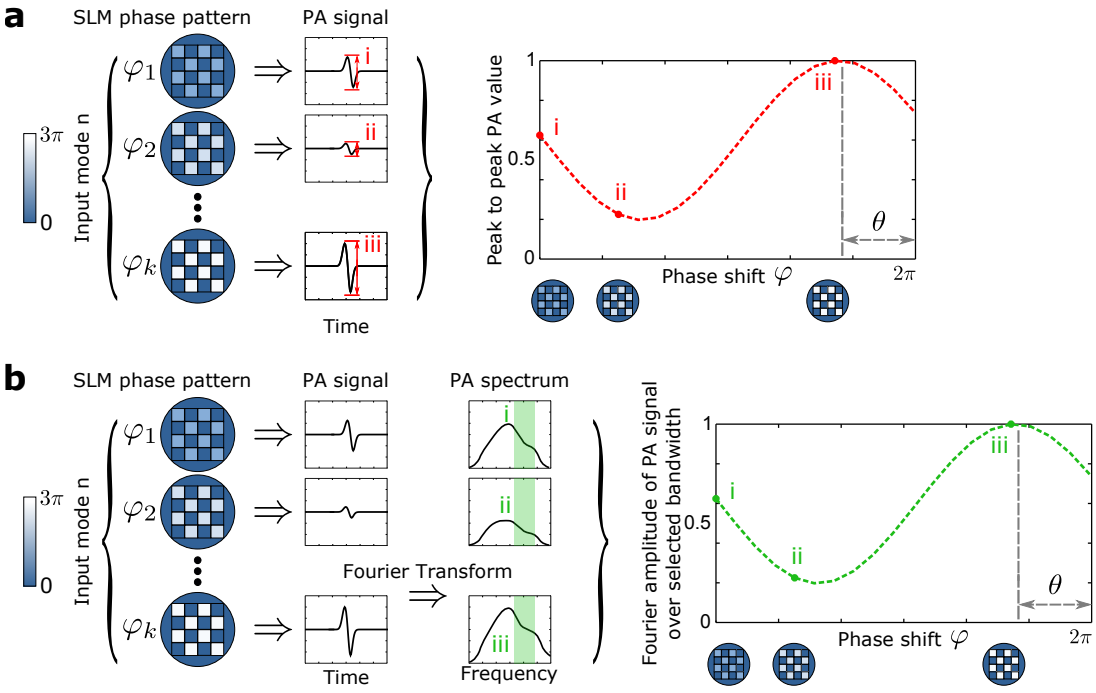

Figure 3.3 – Optimization of photoacoustic feedback signal: typical iteration. a) Optimization of peak-to-peak photoacoustic signal: the phase of each input mode is swept between 0 and 2π, resulting in a sinusoidal modulation of the peak-to-peak value of the photoacoustic feedback signal. This modulation is analyzed to extract the phase that maximizes the feedback signal. This step is iterated for every SLM input mode, which progressively enhances the light intensity on the absorbing target. b) Identical procedure, replacing the peak-to-peak PA signal by the RMS value over a specific frequency band.

3.3 Results and analysis

3.3.1 Photoacoustic signal enhancement

To experimentally demonstrate the influence of spectral filtering on the optimization performances, we optimized light delivery successively using four frequency bands: 10-25 MHz, 25-40 MHz, 40-55 MHz, and 55-70 MHz. Results are presented in Fig. 3.4, Fig. 3.5 and Fig. 3.6.

Fig. 3.4 shows the evolution of the PA enhancement ratio η_{PA}, defined as the ratio between the optimized feedback value and the feedback value that would be obtained under homogeneous illumination. To simulate this homogeneous illumination, we average the PA signals for 200 different positions of the diffuser, i.e. 200 different speckle patterns on the absorber. As in the previous chapter, this is made possible thanks to speckle statistics [Goodman 07] and to the linearity of the photoacoustic signal generation and detection (see section 1.5).

This normalization is quite crucial, as we cannot use the peak-to-background ratio usually measured in all-optical focusing experiments. We do not normalize the optimized signal by its initial value because it strongly depends on the initial speckle illuminating the absorber. It would therefore artificially influence the enhancement value regardless of the real focusing efficiency.
Each trace color in Fig. 3.4 corresponds to one given feedback signal. In Fig. 3.4.a, each graph corresponds to optimizations starting from one specific speckle pattern. Fig. 3.4.b shows the same traces averaged over five distinct optimizations, starting from 5 different initial speckle patterns. This allows us to smooth any influence of the initial speckle pattern, which could eventually affect the optimization process. For instance, if the absorber is initially illuminated by a dark speckle grain, the feedback signal to start with will be low and it will be hard for the optimization process to pass above the noise threshold, whereas if it starts from a higher feedback signal, it will be easier.

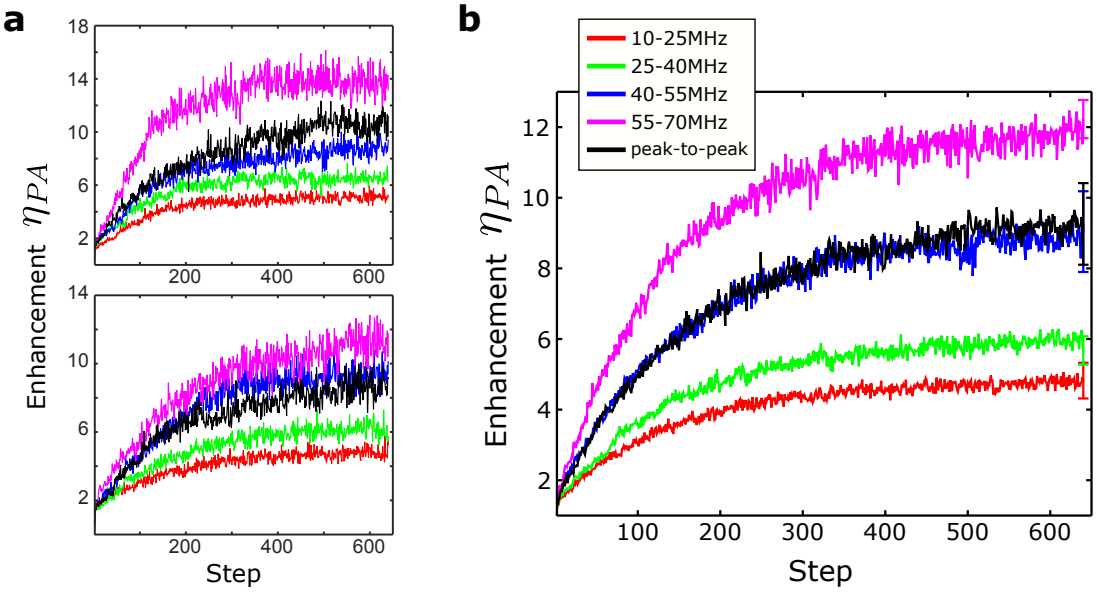

Figure 3.4 – Photoacoustic feedback optimization. a) Evolution of the photoacoustic feedback values (RMS value over selected band or peak-to-peak value) during their respective optimization: 10-25 MHz (red), 25-40 MHz (green), 40-55 MHz (blue) and 55-70 MHz (magenta), peak-to-peak (black). The two graphs correspond to optimizations starting from two distinct speckle patterns. The feedback values are normalized by their value under homogeneous illumination to compute the enhancement. b) Evolution of the photoacoustic feedback values, averaged over five different optimizations starting from distinct speckle patterns, including the ones in (a). The error bars (at the right end of each trace) are the corresponding standard deviations of the final values, estimated from the five optimizations.

We observe that the enhancement ratio η_{PA} increases with the frequency range used to compute the feedback signal. Indeed, in this chosen configuration, the number of speckle grains whose intensities are simultaneoulsy optimized decreases while increasing the optimized frequency range. These speckle grains are the ones contained in the absorber portion that is probed by the transducer. They have been adjusted to be larger than the absorber diameter in the x direction, because the absorber lies in the optical far field. Therefore this number corresponds here to a surface ratio, which gives in this specific geometry, using a linear absorber:

$$N_{speckle\ grains} = \frac{\varnothing_{acoustic} \cdot \varnothing_{wire}}{\varnothing^2_{speckle}} \tag{3.3}$$

Combining equations 3.2 and 3.3, the number of simultaneously enhanced output modes scales with the inverse of the optimized frequency: $N_{speckle\ grains} \propto f^{-1}$. This leads to $\eta_{PA} \propto f$, using Eq. 3.1, as qualitatively illustrated in Fig. 3.5.

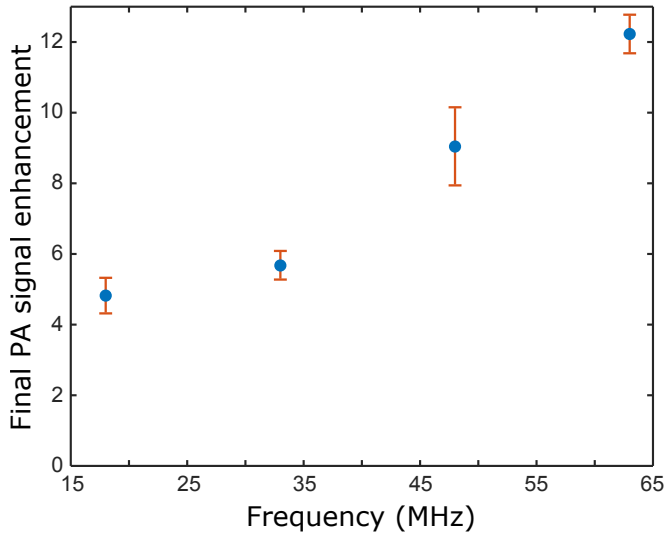

Figure 3.5 – Frequency dependence of the final PA signal enhancement: experimental results. Blue dots represent the averaged enhancements over the 5 different optimizations; orange bars represent the standard deviations over the different optimizations.

A large number of optimizations starting from different initial speckle patterns would be required to obtain a proper quantitative confirmation of this proportionality. The optimization of the high frequency components thus leads to a larger enhancement of the PA signal than the optimization of the low frequencies. In the second chapter as well as in [Kong 11, Caravaca-Aguirre 13], the feedback value was the peak-to-peak amplitude of the PA signal. We observe here that the optimization of the peak-to-peak leads to an enhancement smaller than the optimization of the 55-70 MHz frequency band, which suggest that in some cases this feedback value could be preferred.

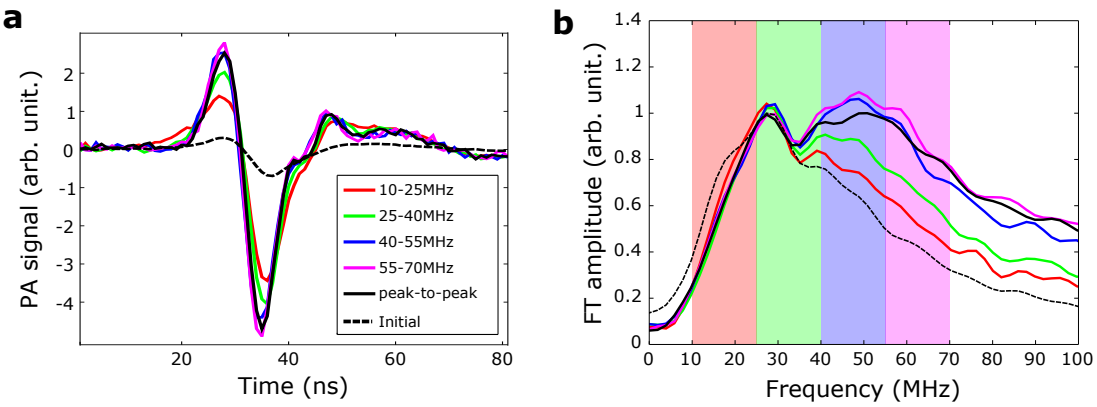

Figure 3.6 – Optimized photoacoustic signals. a) Final photoacoustic signals after optimization of the RMS value computed over each frequency band, or the peak-to-peak amplitude. b) Fourier amplitudes of the photoacoustic signals before and after each optimization. The initial signal is multiplied by 4.4 for comparison. The coloured stripes depict the four frequency bands that are used for the optimizations.

Fig. 3.6.a shows the initial and final PA signals after each frequency band optimization (averaged over the five realizations of the optimization). Fig. 3.6.b shows the corresponding final amplitudes summed over a frequency band (also averaged over the five realizations of the optimization). Although the PA signals after optimization of the 55-70 MHz band or peak-to-peak amplitude look similar, the difference on the Fourier amplitudes is more striking.
We observe that the optimization has two effects. The energy inside the whole spectrum increases, and it also tends to increase the high frequency part of the spectrum when optimizing RMS value on higher frequency bands.

3.3.2 Direct observation of light focusing

To confirm the spatial confinement of the optical focus when optimizing different frequency components of the PA signal, we imaged the speckle pattern on a CCD camera. Each image is individually normalized by the total energy of the corresponding laser pulse measured with the photodiode. Fig. 3.7 shows the final speckle patterns after the different optimizations. Each stripe (from 1 to 5) represents one realization of the optimization starting with a different initial speckle pattern, and each section (from a to d, and f) corresponds to each frequency range. As expected, high frequency optimization leads to a tighter focal spot than lower frequencies optimizations. The vertical confinement is due to the fact that the wire lies horizontally. Fig. 3.7.d and f shows that the optimizations of either the 55-70 MHz band or the peak-to-peak amplitude lead to similar widths of the focal spots. The mean full width at half maximum (FWHM)

(averaged over the five optimizations) is 66 µm for the optimization of the 55 to 70 MHz band, and 43 µm for the optimization of the peak-to-peak value. However, the peak-to-peak optimization focuses alternatively on one or another speckle grain, whereas the high frequencies optimization tends to always focus on the same grain. The FWHM of the sum of all five final speckle patterns (Fig. 3.7.e) is indeed 44 µm for the optimization of the 55 to 70 MHz band, but 111 µm for the optimization of the peak-to-peak value. The direct observation of the optical speckle pattern reveals the important influence of the feedback value.

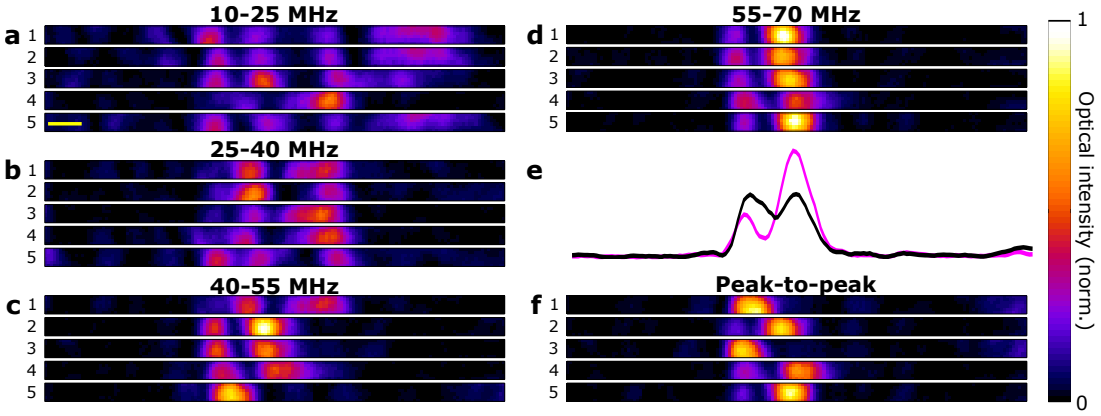

Figure 3.7 – Final speckle patterns monitored on the camera after optimization of RMS value over: a) 10-25 MHz, b) 25-40 MHz, c) 40-55 MHz, d) 55-70 MHz, or of peak-to-peak value f) of the photoacoustic signal. For each band, we performed the optimization starting from five different initial speckle patterns: each stripe (1 to 5) shows the final speckle pattern corresponding to the optimization starting from a different initial pattern. The images are normalized by the maximum final intensity among all final images. e) Horizontal cross sections of the final speckle pattern averaged over the five realizations, after optimization of the RMS value over the 55-70 MHz frequency band (magenta), or of the peak-to-peak amplitude (black) of the PA signal. scale bar in (a): 50 µm.

Although the final PA signals are quite similar for both optimizations, the final distribution of the optical intensity varies substantially. Furthermore, we study the evolution of the optical intensity during the optimization of each PA feedback signal. Fig. 3.8.a and b show the evolution of the *maximum* optical intensity during the different optimizations presented in Fig. 3.4.a or averaging over the five different optimizations as in Fig. 3.4.b, respectively.
These results demonstrate that the light intensity is indeed enhanced by optimizing different PA feedback values. The optical peak intensity enhancement approximately exhibits the same dependence in the feedback signal, as compared to the PA signal enhancement. However, there is no direct proportionality. The underlying reason is that the energy over a given bandwidth of the PA spectrum can be either enhanced by a global increase in the light intensity, or by a redistribution of the energy over the absorbing sample.

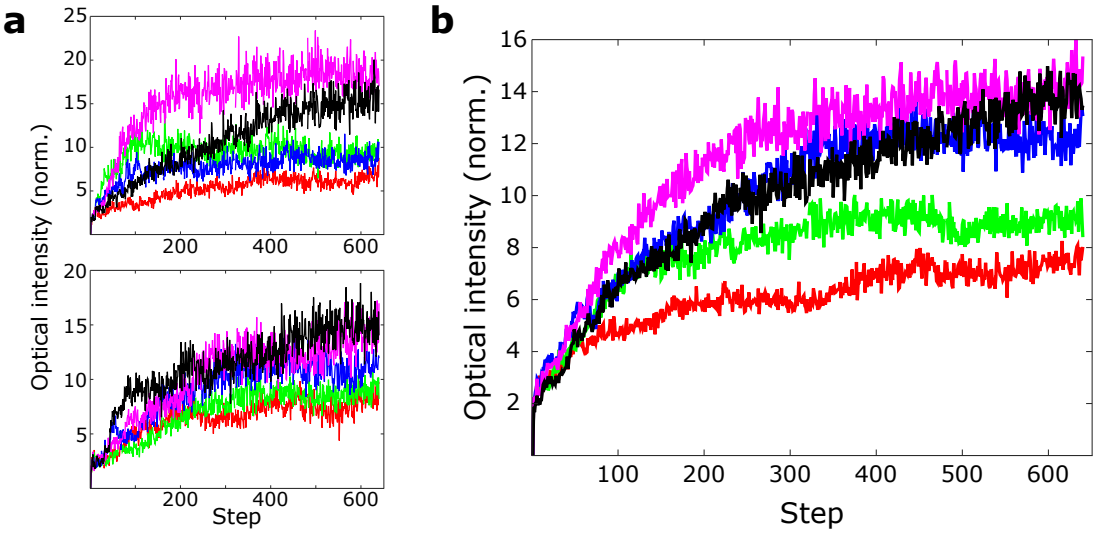

Figure 3.8 – Enhancement of the maximum optical intensity. a) Evolution of the maximum optical intensity during the optimization of the different PA feedback values. The color convention is identical to that in Fig. 3.4. The two graphs correspond to optimizations starting from two distinct speckle patterns. The intensities are normalized by the mean intensity of the initial speckle pattern. b) Evolution of the maximum optical intensity during optimizations of the filtered photoacoustic feedback values, averaged over five different optimizations starting from distinct speckle patterns, including the ones in (a).

In other words, for a given total light intensity, the high frequency component of the PA signal is larger for a tight focus than for an extended one. Although the optimization of the highest frequency band and of the peak-to-peak value reach similar maximum light intensities, as seen in Fig. 3.7.d and f, it should be noticed that the optimization of the high frequency component leads to a faster convergence, as demonstrated in Fig. 3.8.b. Finally, we emphasize that the focusing capabilities of the PA feedback optimization strongly depends on the initial speckle pattern, a fact that should be taken into account for any future application.

3.4 Limitations

3.4.1 Influence of the laser pulse duration

Considering the 30 µm diameter of the absorbing wire, the stress confinement characteristic time is here equal to $\tau_{ac} = \frac{D}{c_s} = \frac{30.10^{-6}}{1500} = 20$ ns, which prevent us from neglecting the laser pulse duration, equal to 8 ns in our case. According to section 1.5.1, when the laser pulse duration τ_p is comparable to τ_{ac}, the fre-

quency content of the PA signal is dictated by the laser pulse rather than by the size of the illuminated absorber. The peak frequency of the PA signal is then approximately given by $f_{max} \simeq 0.37 \frac{1}{\tau_p} \simeq 46$ MHz.
To further investigate the effect of laser pulse duration in our experiment, we simulate the optimization of spectrally filtered PA feedback signal. We numerically reproduce the experimental conditions and optimization procedure. The detailed description of the simulation can be found in appendix C. As we simulate a noise-free experiment, we can afford to use 10 µm diameter speckle grains, to fully appreciate the discrepancies in width of the final optical focus. Laser pulse durations of either 5 ns or 10 ns are simulated.
After optimization of either the 55-70 MHz frequency band or of the peak-to-peak signal, we obtain the final optical focal spots that are shown in Fig. 3.9. The pulse duration filters the PA signal, which strongly affects the optimization

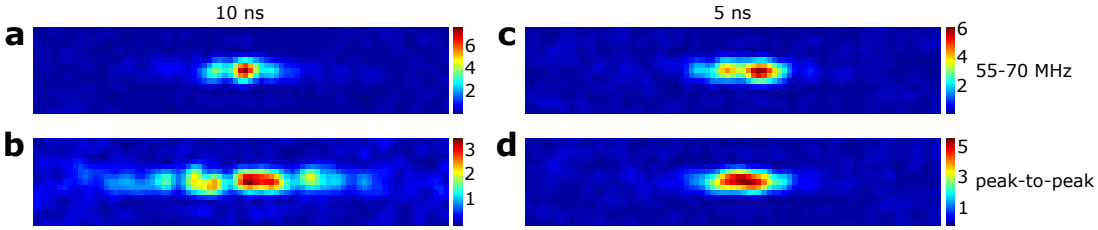

Figure 3.9 – Influence of the laser pulse duration (simulations). Final speckle patterns, averaged over 10 optimizations (starting from different speckle patterns) of: a) RMS value of the highest frequency band (55-70 MHz), with 10 ns pulse illumination. b) peak-to-peak value, with 10 ns pulse illumination. c) RMS value of the highest frequency band (55-70 MHz), with 5 ns pulse illumination. d) peak-to-peak value, with 5 ns pulse illumination. (optical intensity in arbitrary units)

of the peak-to-peak value. Optimizations using 5 ns pulses produces similar focal spots for both optimization, whereas in the case of 10 ns pulse, high frequency optimization leads to a very tight optical focus compared to the peak-to-peak optimization. This pulse duration indeed alters the dimensions of the area probed by the peak-to-peak signal, in particular because the peak frequency of the PA spectrum is lower when using longer pulses, whereas these dimensions are inherently fixed when optimizing the RMS value over a given bandwidth.
However, when using longer pulses with the same total energy, the energy over a high frequency band is obviously reduced, which might impede the efficiency of the optimization in the presence of noise.

3.4.2 How high? Inherent limitations due to noise

In this section, we evaluate the modulation amplitude of the PA feedback signal for a given detected acoustic frequency. The underlying question is: is it always advantageous to optimize frequencies as high as possible? Two counteracting effects indeed occur: by selecting high acoustic frequency, the modulation amplitude of the PA feedback signal will be more contrasted thanks to the reduced number of speckle grains inside the detection area, but the emitted PA signal will also be inherently lower, proportionally to the narrowing of the probed absorbing area. In addition, this signal will be also more filtered out by the transducer electric response.
The focused ultrasonic transducer detects roughly N speckle grains:

$$N \propto \left(\frac{\frac{1}{f_{us}}}{\lambda}\right)^2 = \left(\frac{1}{f_{us}\lambda}\right)^2$$

where f_{us} is the detected acoustic frequency and λ the optical wavelength.
This leads to a PA signal:

$$V_{PA} \propto I \cdot N \propto I \cdot \left(\frac{1}{f_{us}}\right)^2$$

where I is the optical intensity per speckle grain. When modulating the speckle figure, each speckle grain is sinusoidally modulated in respect to the SLM phase, with a randomly distributed phase shift. The resulting PA signal modulation is at first order proportional to the sum of all these contributions, as shown in Eq. 2.3 of the second chapter. As stated in section 2.1, it results in a modulation depth of the PA signal proportional to $I\ \sqrt{N}$. This modulation depth should be larger than the noise level in order to be detected:

$$\sigma < I\ \sqrt{N} \propto \frac{I}{f_{us}}$$

where σ denotes the noise threshold of the PA imaging system, expressed in equivalent optical intensity unit. This sets an upper limit for the detected acoustic frequency. Whenever this modulation is detectable, the mean PA signal be also be above the noise threshold, as $\sigma < I\ \sqrt{N} < I.N$. Furthermore, if f_{us} is low, then N becomes very large, and the detection will be limited by its dynamic range Δ, to be compared to the ratio between the relative modulation depth and the mean PA signal:

$$\Delta < \frac{I\ \sqrt{N}}{I\ N} = \frac{1}{\sqrt{N}} \propto f_{us}$$

which sets in turn a minimum frequency.

3.5 Conclusion

We have shown that focusing light through scattering media by optimizing the PA response of an elongated absorber relies on the frequency content of the PA feedback signal. This type of elongated absorbing structures is a relevant model as it mimics blood vessels, a major endogenous source of PA contrast in tissue [Zhang 09]. We experimentally confirm that the optimization of the high frequency components of the PA signal leads to a larger enhancement of the feedback signal than the optimization of the low frequency components or of the peak to peak amplitude of the signal. We relate this improvement to the reduction in the acoustic focal volume of the spherically-focused transducer as the frequency increases. We also confirmed that a tighter optical focal spot is obtained when optimizing these high frequencies by optically imaging the resulting speckle patterns. We emphasize that specific characteristics of the PA detection (compared to a direct optical detection) may affect the optimization process: the detected signal results from the coherent summation on the detector surface of the acoustic waves emitted by all absorbed speckle grain. Therefore, its frequency content depends on the source geometry, i.e. the spatial distribution of the illumination pattern. Moreover, the lateral detection profile of the transducer gives different weights to the speckle grains. This feature has been used in a recent work in order to reach sub-acoustic resolution focusing [Conkey 15]. In addition, limiting the signal bandwidth Δf affects also the axial resolution of the acoustic probing $\Delta z \propto c_s/\Delta f$, and would have to be taken into account in the case of densely packed absorbing targets in the axial direction. The illumination pulse duration is also numerically shown to influence the optimization process.
Despite these subtleties of photoacoustics, PA feedback optimization still exhibits a similar trend regarding the number of simultaneously optimized output modes compared to the all-optical optimization. Moreover, the optimization of spectrally filtered signals enables a precise control of the focal volume of the transducer. Indeed, the frequency weighting in the peak-to-peak value is expected to change during the optimization, dynamically varying the size of the focal spot, which is prevented in our approach. Our approach may become useful if one wants to achieve optical focusing inside scattering media, where the speckle grain size becomes indeed quickly small and diffraction limited. In such scenarios, one has to reduce the size of the acoustic focus as much as possible to get a measurable increase in the PA signal, using the smallest possible number of degrees of control (SLM pixels). The access to such spectrally controlled focus size does not have a direct counterpart in all-optical wavefront shaping experiments.

Chapter 4

Photoacoustic fluctuation imaging with multiple speckle illuminations: Enhanced visibility and Super-resolution imaging

Contents

The nanosecond pulsed lasers commonly used for PA imaging have a typical coherence length of a few millimeters. After a long enough propagation in tissue, the light coherence can be considered lost: the speckle vanishes and the illumination intensity locally homogenizes. Conventional deep tissue acoustic-resolution PA imaging usually assumes that the embedded absorbing structures are illuminated with an incoherent diffusive halo. When considering small fields of view, this illumination can be considered homogeneous. The assumption of uniform illumination is a strong requirement for quantitative PA image reconstruction. It has also been shown to be responsible for the absence of *acoustic* speckle in photoacoustic images [Guo 09].
On the contrary, when using coherent light, the optical speckle contrast is preserved at depth. This contrast can be only reduced because of cross-polarized speckles. A modulation of the incident wavefront thus results in a modulation of the PA signal generated by the illuminated absorbers. We have shown in the previous chapters that by analyzing this modulation, coherent light could be controlled and focused on a particular absorbing target.
Spatial and temporal fluctuations of the PA signal can actually be harnessed in a less controlled way. Successive uncorrelated speckle illuminations, inducing fluctuations in the PA signal, are shown in this chapter to make up for several inherent limitations of acoustic emission and detection. This dynamic speckle illumination has already proved very useful in optical microscopy for optical sectioning [Ventalon 06], and has also been exploited as a structured illumination source to overcome the optical diffraction limit [Mudry 12]. Here we show that such an illumination engineering is also relevant in PA imaging, for which most efforts are usually geared toward acoustic detection.

In the first section, we describe common imaging artefacts arising from limited bandwidth and limited aperture of ultrasonic detection systems. We show in the second section that under some assumptions, the PA imaging process can be written as a convolution of the absorbing object with a given point spread function (PSF). We specifically show that the information gathered with the multiple speckle illumination scheme is retrieved by computing the variance of the PA images set. We then address the visibility problem, by exploiting optical speckle patterns as a structured illumination, effectively breaking the homogeneity of absorbing objects. We finally show that multiple speckle illuminations can also enhance the imaging resolution beyond the acoustic diffraction limit.

This chapter is adapted and extended from:
Gateau, Chaigne, Katz, Gigan & Bossy, *Improving visibility in photoacoustic imaging using dynamic speckle illumination*, Optics letters, 2013 [Gateau 13]
Chaigne, Gateau, Allain, Katz, Gigan, Sentenac & Bossy, *Super-resolution photoacoustic fluctuation imaging with multiple speckle illumination*, Optica, in press [Chaigne 15]

4.1 Fundamental limitations of ultrasonic detection

Any acoustic detector suffers from inherent limitations, among which we find finite bandwidth and finite aperture. These two features cause visibility artefacts in the PA images and limit their spatial imaging resolution. In this section, we describe these limitations and analyze their effects on PA imaging capabilities.

4.1.1 Limited visibility

Under uniform and instantaneous illumination, every point of an absorbing structure emits strongly correlated ultrasonic waves. This correlation (both in phase and amplitude) is due to the simultaneous positive pressure rises at the locations of all absorbers, and leads to destructive interferences, which in turn are responsible for two effects: directivity of the ultrasonic emission for elongated structures and prominent boundary build-up for large structures, as illustrated in Fig. 4.1. This has been demonstrated to explain the lack of acoustic speckle artefacts in PA imaging [Guo 09]. This coherent summation of positive and negative pressures results in visibility issues when imaging homogeneous structures [Beard 11]. These artefacts are illustrated in Fig. 4.2. In Fig. 4.2.a, we consider a large absorbing sphere, so that the central frequency of the emitted ultrasonic pulse is no longer contained within the transducer bandwidth. The resulting PA image will then be mainly dominated by the boundaries, which emit higher ultrasonic frequencies and do not average to zero within the bandwidth of the detector.

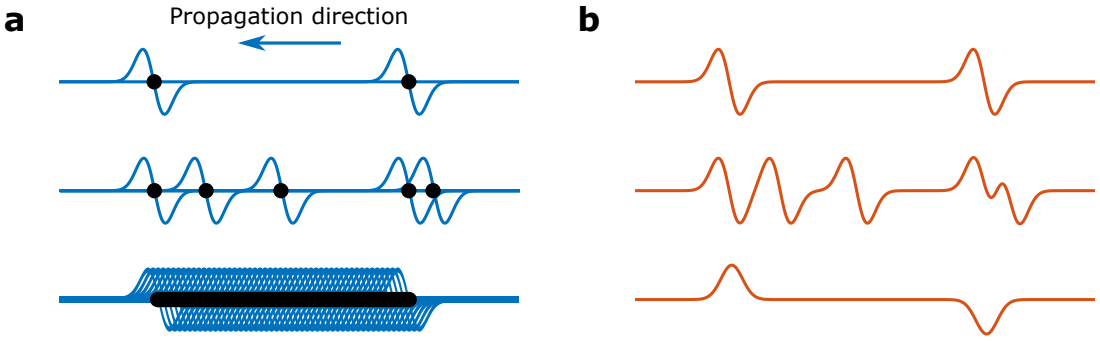

Figure 4.1 – Correlations between emitted ultrasonic waves. a) Black dots represent individual absorbers. Blue lines depict the emitted pressure waves toward the left: each absorber emits one pulse. b) Coherent summation of these pressure waves, as would be detected by an ultrasonic transducer. When imaging an elongated absorber, seen as a collection of packed individual absorbers, only the two tips are visible.

In Fig. 4.2.b, we consider an elongated cylindrical absorber, perpendicularly oriented with respect to the detector surface. Due to the coherent summation of amplitudes, the emission is mostly radial. Therefore, if the detector aperture does not cover a large enough solid angle, most of the emitted waves will not be detected. As a result, only the tips of the absorber will be visible on the PA image.

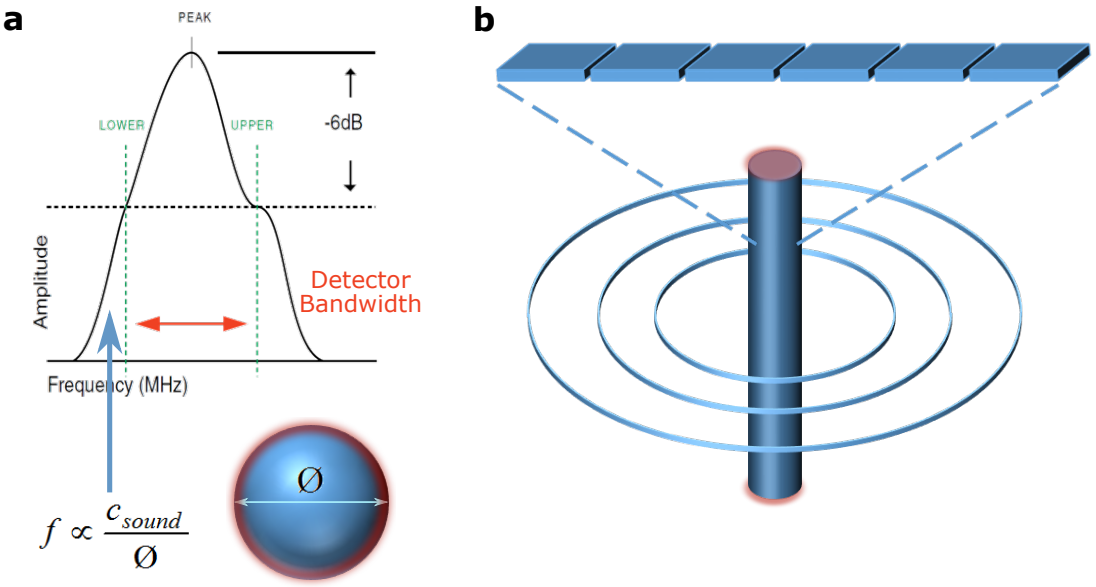

Figure 4.2 – PA imaging visibility problems due to: a) Limited bandwidth: a large absorbing structure emits low ultrasonic frequencies, which might not lie within the bandwidth of the detector. As a result, the object is invisible, except its boundaries (blurry red) that will radiate higher frequencies towards the detector. b) Limited aperture: an elongated structure will mostly radiate cylindrical ultrasonic waves, which cannot reach the detector if perpendicularly arranged with respect to the object. The object will then be invisible, except its tips (blurry red) that will emit spherical waves.

4.1.2 Limited resolution

The resolution of a PA imaging system is inherently limited by acoustic diffraction in deep tissue. We consider here a linear cylindrically focused ultrasonic array. The spatial resolution in the imaging plane (axial: Δz, lateral: Δx) is given by :

$$\Delta z = \frac{c_s}{\Delta f}$$

$$\Delta x = \frac{c_s F}{f D}$$

where c_s is the speed of sound in water, Δf the bandwidth of the array, F the distance to the array surface, f the center frequency of the detector, and D its length. In the transverse direction orthogonal to the probe (y-axis), the resolution is given by the cylindrical focus of the array elements, and is typically about a few millimeters. It should be noticed that the resolution is not constant throughout the imaging plane and is degraded when approaching the boundaries of the field-of-view. It indeed relies on the distance F, as well as on the distance to the central axis of the probe. Objects that are not seen with the same numerical aperture will not be seen with the same resolution. Moreover, if the object is not centered with respect to the array, it will be seen with more elements on one side than on the other, which will result in an asymmetrical reconstruction. Reconstruction algorithms accounting for this issue can be used, which basically weight the signals received at different locations. This apodization usually results in a homogenized though degraded resolution. In the following, we will limit ourselves to small fields of view, centered with respect to the array.

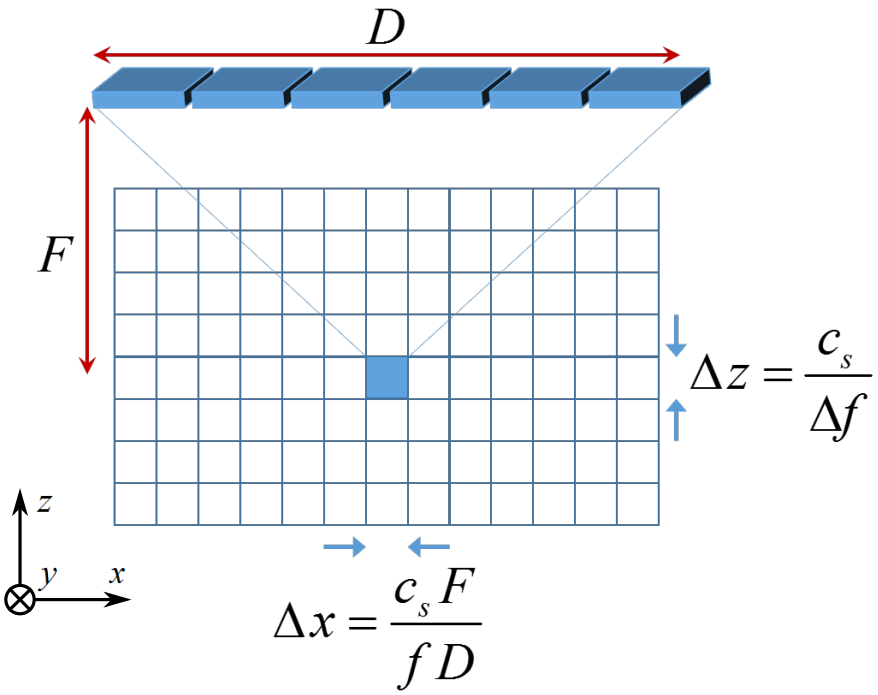

Figure 4.3 – Diffraction limited acoustic resolution. Detector geometry and bandwidth dictate the resolution of the acoustic imaging system.

Until now, most of the effort was deployed to improve ultrasonic detection in order to correct for these flaws. To compensate for the limited aperture, tomographic approaches involving mechanical scanning of the probe have been developed [Gateau 15, Laufer 09, Razansky 11].

Hemispherical probes have been engineered as well, mostly for mammography applications [Kruger 10]. Regarding bandwidth limitations, most acoustic transducers have a bandwidth comparable to their center frequency (usually expressed as a percentage of this center frequency). It is quite challenging to design ultrasonic probes with more than 100% bandwidth, and the ultrasonic probe is usually chosen based on the prior knowledge of the characteristic size of the structure to image. Even in the case of a very large bandwidth probe, appropriate filtering should be applied to separate different size scales [Omar 14].
All these approaches are assuming an incoherent illumination scheme, which corresponds to a locally uniform light intensity distribution. When using coherent light though, multiple speckle illuminations can be produced after light propagation in the scattering tissue, yielding a temporally and spatially fluctuating PA excitation and subsequent emission. Here we show that a simple modification of the illumination scheme can strongly improve these intrinsic weaknesses of ultrasonic detection.

4.2 Principle of photoacoustic fluctuation imaging

4.2.1 Experimental setup

The setup that will be used for all experiments of this chapter is illustrated in Fig. 4.4.a. The beam of a nanosecond pulsed laser (section 4.3: Quantel Brilliant, 532 nm wavelength, 4 ns duration pulse, 10 Hz repetition rate; section 4.4: Continuum Surelite II-10, 532 nm wavelength, 8 ns pulse duration, 10 Hz repetition rate) is focused on a ground glass diffuser (Thorlabs, 220 grit), which can be rotated to generate the varying speckle illumination. The scattered light illuminates a 2D absorbing sample embedded in an agarose gel block. The optical speckle grain size on the target plane can be controlled by adjusting the distance to the diffuser (see section 2.2.1 and appendix B). The absorbing sample is placed in the imaging plane of a linear ultrasound array (section 4.3: Vermon, 20 MHz center frequency, >50% bandwidth, 128 elements cylindrically focused at 8 mm, 80 µm pitch; section 4.4: Vermon, 4 MHz center frequency, >60% bandwidth, 128 elements cylindrically focused at 11 mm, elevation focus: 60 mm, 0.33 mm pitch), connected to an ultrasound scanner (Aixplorer, Supersonic Imagine, 128-channel simultaneous acquisition at 60 MS/s). The phantom is immersed in water to ensure acoustic coupling.

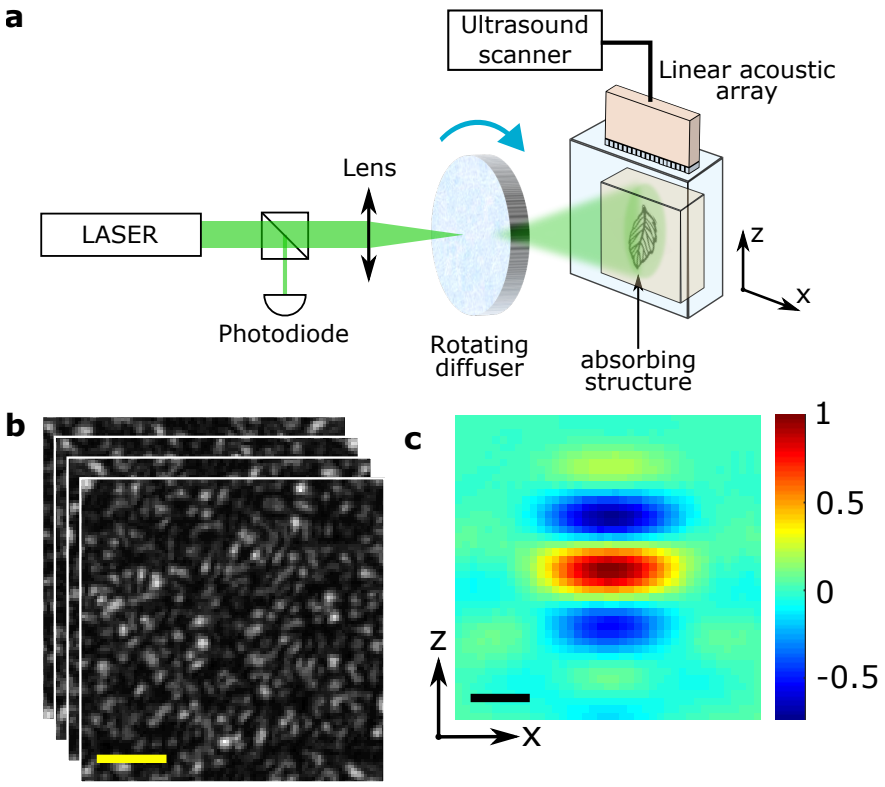

Figure 4.4 – Experimental setup. a) A nanosecond laser pulse is focused on a rotating diffuser. The resulting speckle pattern illuminates an absorbing structure, generating ultrasounds that are detected with a linear ultrasonic array. b) Typical speckle patterns. The speckle grain size is here ∼30 µm, but it varies from one experiment to another.). c) Typical point spread function of the photoacoustic imaging setup using the 4 MHz linear array (envelope FWHM: 360 ± 25 µm in the lateral (x) direction and 450 ± 25 µm in the axial (z) direction). Scale bars: 200 µm.

The intensity of the laser pulses is monitored with a photodiode to compensate for the laser pulse-to-pulse energy fluctuations. In addition, for each speckle illumination (i.e. each diffuser position), the PA signals are averaged over n laser pulses to improve the SNR (section 4.3: n=1; section 4.4: n=25). The signals are then filtered between with a 3^{rd} order Butterworth filter for noise removal outside of the array bandwidth (section 4.3: between 500 kHz and 25 MHz; section 4.4: between 1 MHz and 8 MHz). PA images are reconstructed on a grid of pixels (section 4.3: 20 µm in x-axis and 6 µm in z-axis; section 4.4: 25×25 µm^2) with a conventional back-projection algorithm based on summing values of the PA signals taken at appropriate retarded times.

4.2.2 Photoacoustic imaging as a convolution process

We consider PA images reconstructed from a set of PA signals measured with an ultrasound array. In this section, we show that under appropriate assumptions the reconstructed PA quantity $A(\mathbf{r})$ may be written as a convolution.
In its simplest form, the generation and propagation of PA pressure waves $p(\mathbf{r}, t)$, generated by a distribution $\mu_a(\mathbf{r})$ of optical absorption illuminated by a pulsed light with intensity $I(\mathbf{r}) \cdot f(t)$, may be described in a homogeneous acoustic medium (with speed of sound c_s and Grüneisen coefficient Γ) by the following equation:

$$\left[\frac{\partial^2}{\partial t^2} - c_s^2 \nabla^2\right] p(\mathbf{r}, t) = \Gamma \mu_a(\mathbf{r}) I(\mathbf{r}) \frac{\partial f(t)}{\partial t} \tag{4.1}$$

Eq. 4.1 shows that for a given temporal light pulse shape $f(t)$, the pressure field is *linearly* related to the distribution $\mu_a(\mathbf{r})I(\mathbf{r})$ of optical absorption times the optical intensity pattern. When using a conventional delay-and-sum back-projection algorithm, the reconstructed images remain *linearly* related to $\mu_a(\mathbf{r})I(\mathbf{r})$. Moreover, if this linear reconstruction process may also be considered as translation-invariant, i.e. a spatial translation of the object simply translates the reconstructed object, then the reconstruction process may be written as a convolution. The reconstructed PA quantity $A(\mathbf{r})$ may then be written as a convolution:

$$A(\mathbf{r}) = \int_{\substack{imaging \\ plane}} \mu_a(\mathbf{r}') \cdot I(\mathbf{r}')\ h(\mathbf{r} - \mathbf{r}')\ d\mathbf{r}' = [\mu_a(\mathbf{r}) \cdot I(\mathbf{r})] * h(\mathbf{r}) \tag{4.2}$$

where h is the PSF corresponding to the conventional PA imaging process.
Since PA signals are measured on some boundary around the region to be imaged, translation invariance cannot be strictly verified. Fig. 4.5 shows the spatial variations of the PSF of a simulated typical two-dimensional PA imaging system. However for a small enough field-of-view, it is reasonable to assume that the reconstruction process is translation-invariant: each point of this small field-of-view is reconstructed with the same PSF[1].

[1] We can actually use the only linearity assumption, and use space dependent PSF to write:

$$A(\mathbf{r}) = \int_{\substack{imaging \\ plane}} \mu_a(\mathbf{r}') \cdot I(\mathbf{r}')\ h(\mathbf{r}, \mathbf{r}')\ d\mathbf{r}'$$

$h(\mathbf{r}, \mathbf{r}')$ actually denotes here the Green function of the system, which provides the pressure field at $\mathbf{r}$ resulting from a point source at $\mathbf{r}'$. The following fluctuation imaging results can also be derived in this framework. We cannot however use deconvolution in this context, but it still provides resolution and visibility enhancement.

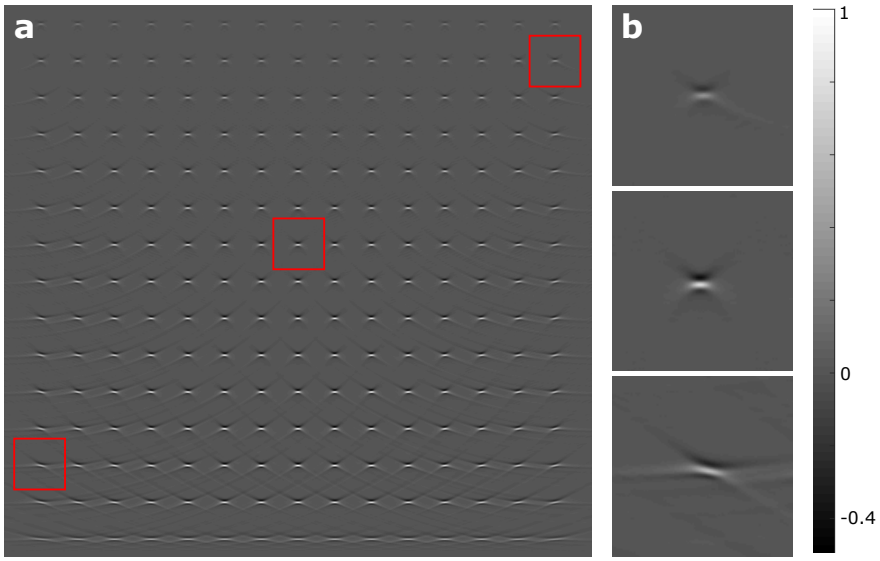

Figure 4.5 – Spatially dependent PSF of a two-dimensional photoacoustic imaging system (simulations[2]). a) Photoacoustic image of a collection of 10 µm beads, 2 mm apart from each other, reconstructed on a large field-of-view (0-32 mm (x-axis), 0-30 mm (z-axis)). The simulated detector is located at the top of the field-of-view, its length is equal to 32 mm. b) Zoomed images on 3 particular locations in the field-of-view (red frames on a), clearly highlighting the non translation invariance of the PSF on a large field-of-view.

Let us now consider that the region of interest is successively illuminated by many different speckle patterns $I_k(\mathbf{r})$ with mean $\langle I(\mathbf{r})\rangle = I_0$, as sketched in Fig. 4.6. The mean PA image is estimated from averaging the PA images obtained with many uncorrelated speckle illuminations:

$$\langle A\rangle(\mathbf{r}) = I_0 \cdot [\mu_a(\mathbf{r}) * h(\mathbf{r})] \tag{4.3}$$

This mean PA image is therefore similar to the image that would be obtained under homogeneous illumination. As a consequence, it will exhibit visibility limitations, as sketched in Fig. 4.6.b. Moreover, the resolution of the reconstructed mean image $\langle A\rangle(\mathbf{r})$ is dictated by the spatial frequency content of $h(\mathbf{r})$, limited by both bandwidth and aperture of the detector.

[2] The beamforming algorithm is summing over the derivative of the acoustic signals, and dynamically maintain a constant angular aperture as much as possible. Boundary effects are attenuated by apodizing with a Hamming window. The array elements have a finite size and the attenuation of ultrasounds is not taken into account here.

4.2.3 Variance image as a convolution with the squared point spread function

In Fig. 4.6.a yet, we observe that some PA signals originating from central parts of the elongated object are actually detected, and that the signals fluctuate when changing the speckle realisation. By computing these fluctuations, we show that we can bypass these destructive interferences arising from correlations in the PA emission.

We specifically compute the variance of the set of PA images obtained under

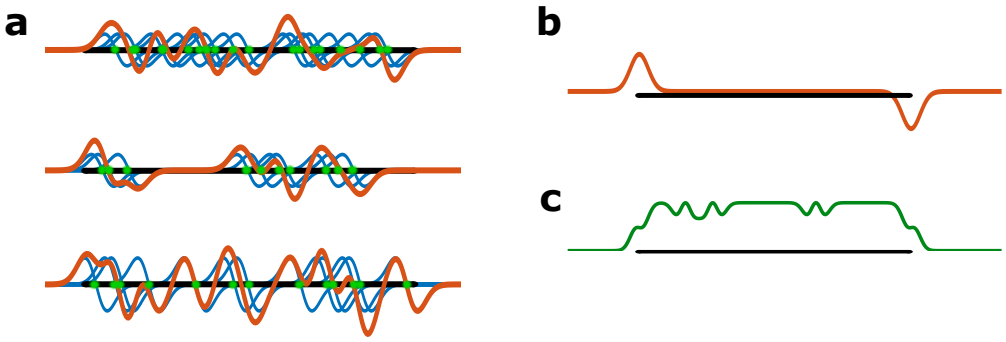

Figure 4.6 – Principle of variance imaging. a) Elongated absorber illuminated by 3 different speckle patterns. The black thick line represents the absorber. The green dots depict the bright speckle grains. The blue lines depict the emitted pressure waves in one given direction: each part of the absorber illuminated by a single speckle grain emits one pulse. The orange line is the coherent summation of these pressure waves, resulting in either destructive or constructive interferences. b) Coherent sum of all PA signals obtained with many uncorrelated speckle illuminations. We thus retrieve the PA signal that would be detected if the illumination was homogeneous. c) Variance of the same data set.

the successive speckle illuminations. Under the assumption that the optical speckle size is much smaller than that of $h(\mathbf{r})$, the variance image $\sigma^2[A](\mathbf{r})$ for uncorrelated speckles is given by:

$$\sigma^2[A](\mathbf{r}) = \iint C(\mathbf{r}', \mathbf{r}'')\mu_a(\mathbf{r}')\mu_a(\mathbf{r}'')h(\mathbf{r}-\mathbf{r}')h(\mathbf{r}-\mathbf{r}'')d\mathbf{r}'d\mathbf{r}''$$

where

$$C(\mathbf{r}', \mathbf{r}'') = \langle I(\mathbf{r}') \cdot I(\mathbf{r}'')\rangle - \langle I(\mathbf{r}')\rangle \cdot \langle I(\mathbf{r}'')\rangle$$

is the autocovariance of the intensity fluctuations of the speckle patterns.

Under the common assumption that the speckle is wide-sense stationary[3], the autocovariance function C is a function of one single variable $\mathbf{r} = \mathbf{r}' - \mathbf{r}''$ [Goodman 07, section 4.4.1]. This function $C(\mathbf{r})$ is sharply peaked around its center, and its characteristic length is by definition the speckle grain size (see appendix B). If the speckle grains are small enough compared to the PSF, $C(\mathbf{r}'-\mathbf{r}'')$ may be considered proportional to a delta function $\delta(\mathbf{r}' - \mathbf{r}'')$ in the double integral above, yielding the following convolution expression:

$$\sigma^2[A](\mathbf{r}) \propto \int \mu_a^2(\mathbf{r}')h^2(\mathbf{r} - \mathbf{r}')d\mathbf{r}' = \mu_a^2(\mathbf{r}) * h^2(\mathbf{r}) \tag{4.4}$$

The variance image appears as the convolution of the squared object by the squared PSF. As this squared PSF is no longer bipolar, there are no more destructive interferences to fade out the signal generated by the extended absorber, as shown in Fig. 4.6.c. In section 4.3, we experimentally demonstrate that PA fluctuation imaging enables to enhance the visibility of a PA imaging system.
As the squared PSF has a higher frequency content than the PSF itself, the variance image is expected to have a higher resolution as compared to the mean image. In section 4.4, we experimentally demonstrate that PA fluctuation imaging allows as well to enhance the resolution of PA imaging beyond the acoustic resolution.

4.3 Visibility enhancement using multiple speckle illumination

In this section[4], we investigate the operation of a high frequency and limited-view PA system with dynamic optical speckle illumination of homogeneously absorbing structures. The final images are obtained by computing the local fluctuations of the PA signal under different speckle illuminations.

4.3.1 Experimental results

We test our method using two absorbing samples that mimic the artefacts described in section 4.1: limited view (Fig. 4.7) and boundary build-up due to limited bandwidth (Fig. 4.8). For the first phantom, we use a 30 µm diameter black-colored nylon suture thread (NYL02DS, 10/0, Vetsuture) arranged in a

[3] The spatial fluctuations of the speckle intensity are described by the same statistics than the fluctuations of the intensity of one given speckle grain over several uncorrelated speckle patterns.

[4] All experiments in this section were carried out by Jérôme Gateau.

two-loop knot, which we embed in agarose gel (see Fig. 4.7.a). The second phantom is made of a cylindrical ink inclusion of 5 mm in diameter in agarose gel (see Fig. 4.8.a). In each experiment, we acquire 500 different PA images, each one corresponding to one specific speckle illumination. The images are normalized by the maximum value over the entire data set before further calculations. We first consider a speckle grain width of about ∼6.5 µm. We average the 500 images on a per-pixel basis and assess the fluctuations by computing the standard deviation of the image set. To extract the envelope of the PA images, we compute the modulus of the analytic signal representation (Hilbert transform) of each column (z-axis). When applied, this step is performed at the very end of the entire image processing.

Overcoming limited-view acoustic detection

Fig. 4.7.a shows a picture of the first absorbing sample. Fig. 4.7.b-g show the corresponding PA images obtained under different illuminations. Detection is performed here using a linear array located at the top of the presented field-of-view. The black thread was oriented in such a way to highlight the limited-view issue when using uniform illumination.
Fig. 4.7.b shows the mean PA image, mimicking the image that would be obtained under uniform illumination. It appears clearly that we are only able to image the top and bottom portions of the wire, which are approximately parallel to the array surface. The image obtained with one speckle illumination show that the previously "hidden" portions of the thread now appear with a granular structure, as if they were formed of discrete absorbers rather than of a continuous one (see Fig. 4.7.c). This phenomenon can be explained by the heterogeneous spatial distribution of light intensity, which breaks the amplitude correlation among the ultrasound waves generated by each point-like absorber throughout the structure. However, segments that are visible in the mean image are still largely predominant.
Fig. 4.7.f shows the difference between two PA images obtained with two distinct speckle illuminations. Previously hidden vertical structures also appear grainy, however all portions of the thread now appear with a comparable contrast. Fig. 4.7.g shows the standard deviation of the 500 PA images obtained with different speckle illuminations. The continuity of the absorbing structure is restored, and the complex shape of the structure is fully retrieved. This effect results from the quasi-omnidirectional radiation patterns of high-frequency photoacoustic waves under speckle illumination.

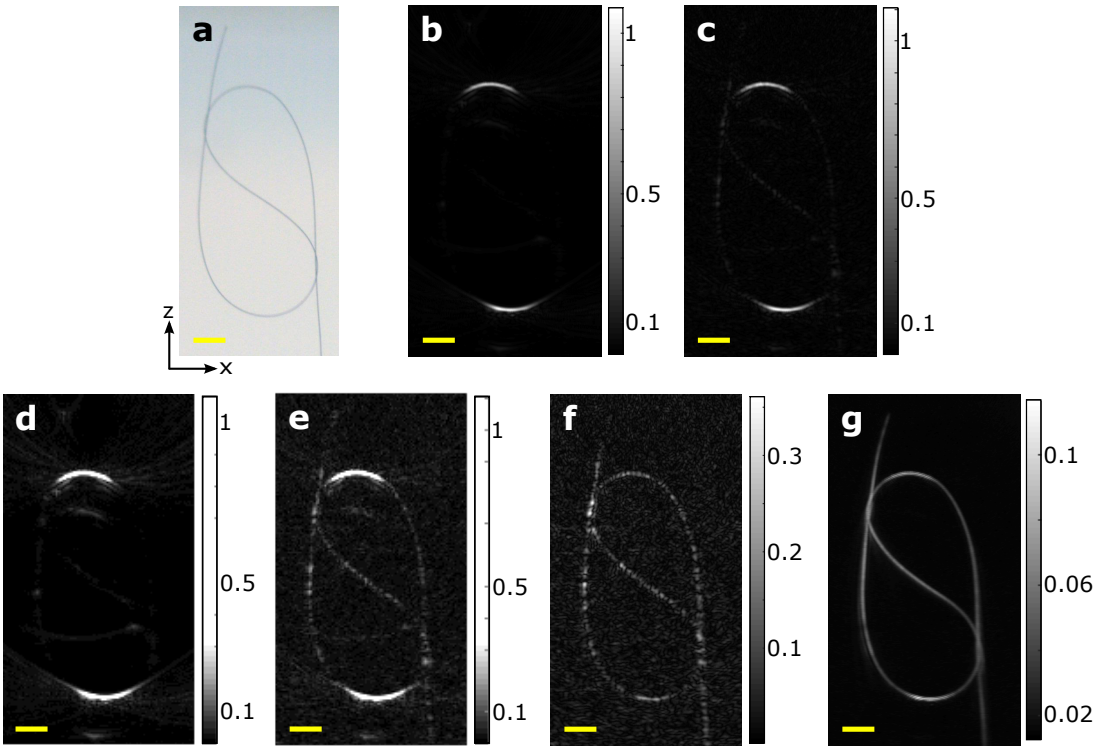

Figure 4.7 – Speckle illumination to overcome photoacoustic emission directivity. a) Picture of the absorbing sample. b) Mean photoacoustic image (envelope), obtained by averaging 500 photoacoustic images with different speckle illuminations, hence mimicking homogeneous illumination. c) Single photoacoustic image of the thread illuminated by one specific speckle pattern (envelope). d-e) Same as (b-c), with increased contrast and saturation for visual comparison. f) Difference between two photoacoustic images obtained with two uncorrelated speckle patterns (envelope). g) Standard deviation, computed over the same set of 500 images. Scale bars: 1 mm.

Overcoming boundary build-up due to limited bandwidth

Fig. 4.8.a shows a picture of the second phantom. Because of its shape, size and homogenous absorption, this ink inclusion is expected to mostly emit ultrasound frequencies in the sub-megahertz range when uniformly illuminated [Diebold 94]. Such frequencies cannot be recorded efficiently with the high-frequency piezoelectric transducer used in the setup. Therefore, the inner absorption could not be visualized on the mean image (see Fig. 4.8.b). Only the edges facing towards the detector and a few sparse absorbers, most probably dust particles or large ink particles were visible. The side edges could not be reconstructed because of the limited aperture of the array along the x-axis. Fig. 4.8.c shows the PA image obtained under one specific speckle illumination. We observe that the object is partly revealed, with a granular aspect and prominent boundaries. We finally assess the fluctuations of each pixel by computing the standard deviation over

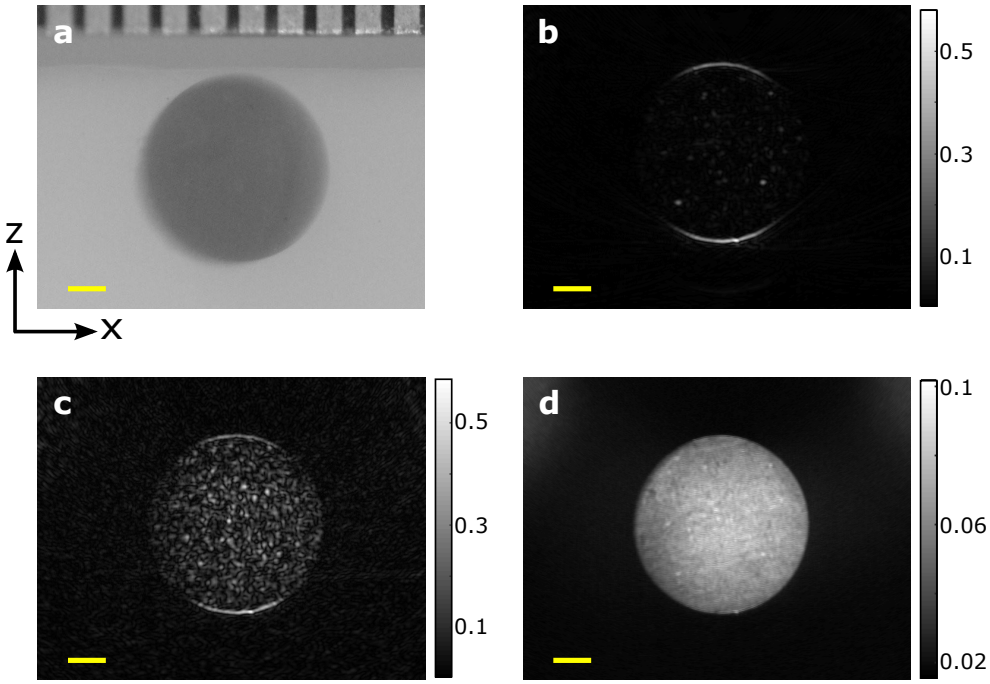

Figure 4.8 – Speckle illumination to overcome boundary build-up. a) Picture of the absorbing sample. b) Mean photoacoustic image (envelope), obtained by averaging 500 photoacoustic images with different speckle illuminations, hence mimicking homogeneous illumination. c) Single photoacoustic image of the thread illuminated by one specific speckle pattern (envelope). d) Standard deviation, computed over the same set of 500 images. Scale bars: 1 mm.

500 different speckle illuminations (Fig. 4.8.d). It clearly shows that the absorbing inclusion can be imaged and appears with a uniform brightness, closely reproducing its absorption profile.

We emphasize that the speckle grain itself does not generate acoustic frequencies contained within the bandwidth of the ultrasonic array. The grain width is approximately equal to 6 µm, and the stress confinement regime is not valid anymore for such a small absorber. The frequency content of the PA signal is then given the laser pulse duration (see section 1.5.1), giving rise to acoustic frequencies of the order of 90 MHz for a pulse duration of 4 ns, which lies far beyond the upper cut frequency of the detector. The speckle pattern observed in Fig. 4.8.c is then not the direct visualization of the optical speckle illumination, but actually of the acoustic speckle resulting from such spatially fluctuating illumination. Nonetheless, we clearly see that the successive speckle illuminations generate fluctuations in the PA emission, which enables to reveal the full absorbing object.

For the reconstruction of each absorbing structure, we used 500 PA images. This could potentially affect the performances of any PA imaging system aiming at real time imaging. However, very few PA images under uncorrelated speckle illuminations are required if one only wants to retrieve structural information. Fig. 4.9 shows the standard deviation images for both samples, using only 10 speckle patterns. Other fluctuation estimators can be used. The Gini mean deviation has been considered because it is not defined in terms of a specific measure of central tendency [Jasso 79].

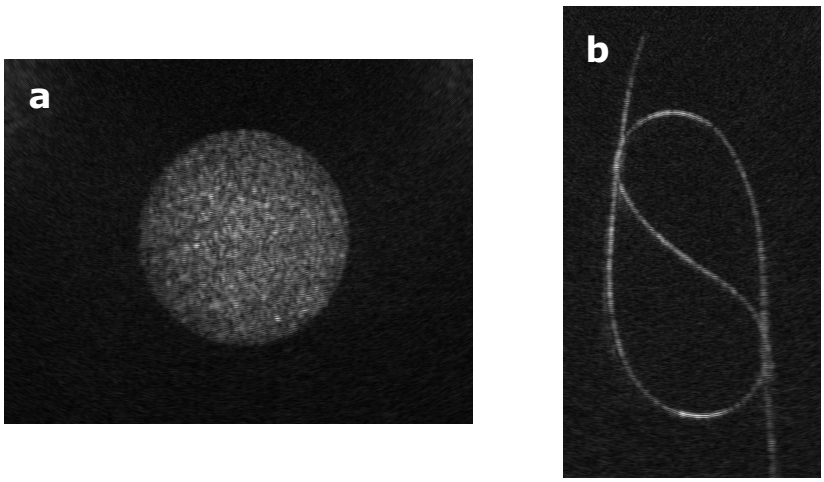

Figure 4.9 – Fluctuation imaging using very few (10) photoacoustic images with different speckle illuminations. a) Standard deviation of 10 photoacoustic images of the ink inclusion, measured under uncorrelated speckle illuminations. b) Standard deviation of 10 photoacoustic images of the wire, measured under uncorrelated speckle illuminations.

Fluctuation amplitude vs speckle grain size

As introduced in section 2.1, the contrast of these fluctuations is varying as $\frac{1}{\sqrt{N}}$, with N the number of speckle grains contained within the acoustic resolution cell [Goodman 07, section 4.6.1]. For a fixed mean PA signal, the standard deviation should then be proportional to the speckle grain diameter, since $N \propto \frac{1}{(\varnothing_{speckle})^2}$:

$$\frac{\sigma[A](\mathbf{r})}{\langle A \rangle(\mathbf{r})} \propto \frac{1}{\sqrt{N}} \propto \varnothing_{speckle} \tag{4.5}$$

In order to study this dependence, we repeat the experiment with the first phantom and five different speckle grain sizes, with 200 images for as many uncorrelated speckle illuminations. This size is adjusted by varying the distance between

the diffuser and the absorbing sample. The laser power is also adjusted to maintain a similar signal-to-noise ratio (SNR) in all experiments. We therefore obtain one mean PA image and one standard deviation image for each speckle grain diameter.

We then compute the ratio between the standard deviation image and the mean image corresponding to a given grain diameter, for pixels having a value above a given threshold (see Fig. 4.10.d,e). This enables to only select the pixels that actually correspond to the absorbing structure and that contribute to the mean PA signal, regardless of visibility issue. We finally average the obtained ratios for each speckle grain diameter, and plot the resulting fluctuation contrast as a function of speckle grain diameter as measured with a CCD camera. Fig. 4.10.a illustrates the results, confirming that fluctuations of the PA signal linearly increase with the speckle grain size.

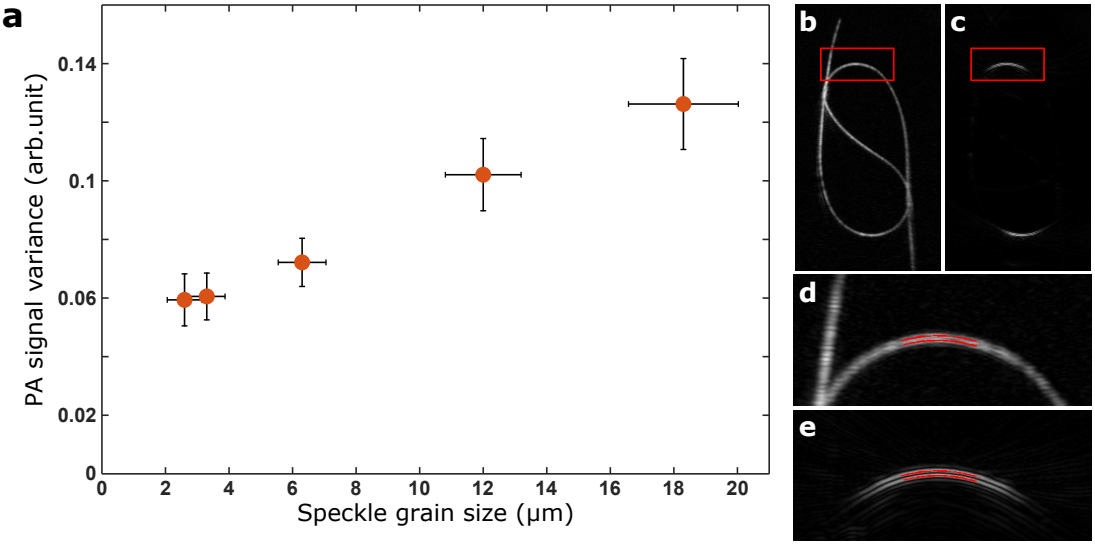

Figure 4.10 – Photoacoustic signal fluctuations as a function of speckle grain size. a) Fluctuation contrast as a function of speckle grain diameter. The vertical error bars represent the standard deviation of the measured contrast on the different pixels shown in red in (d) and (e). The horizontal error bars represent the estimated precision on the speckle diameter as measured on the CCD camera. b) Photoacoustic standard deviation image using the largest speckle grain diameter. c) Photoacoustic mean image using the largest speckle grain diameter. The red frames depict the region which is zoomed in (d) and (e). d) Zoom on the photoacoustic standard deviation image. e) Zoom on the photoacoustic mean image. The red pixels indicate the pixels that are used to compute the fluctuation contrast. The corresponding pixel values are greater than 3 times the standard deviation of the pixel values over the zoomed mean image.

4.3.2 Fluctuation imaging using the photoacoustic transmission matrix

At this stage, it should be noted that the measurement of the photacoustic transmission matrix inherently involves multiple speckle illuminations. Its analysis allows then to reveal structures that are hidden in conventional PA images, as illustrated in Fig. 4.11. As the speckle patterns are not entirely uncorrelated when considering a given input mode, we do not directly compute the variance of the PA images set. We instead average the modulation amplitudes (corresponding to the successive input modes) at each pixel of the PA image. More specifically, the modulus of the transmission matrix elements are averaged over the input modes: $I_m =< |t^{PA}_{mn}| >_n$, where I is the image displayed on Fig. 4.11.c, and T^{PA} the photoacoustic transmission matrix. The index m corresponds to a given pixel of the PA image and the index n corresponds to the input mode. We thus obtain a modulation image revealing all segments of the leaf skeleton independently of their orientation. We emphasize that the image of Fig. 4.11.c is obtained without any additional measurement, all the information being contained in the transmission-matrix.

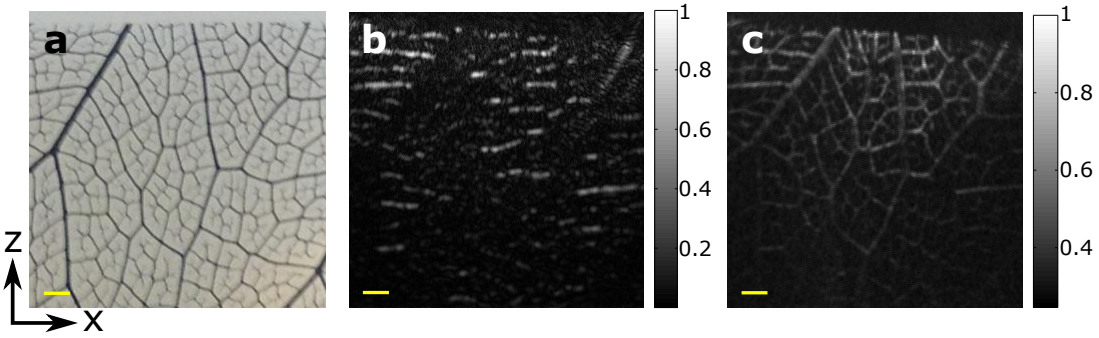

Figure 4.11 – Improved photoacoustic imaging using the transmission matrix. a) Reference photograph of an absorbing leaf skeleton embedded in an agarose gel block. (b) Mean photoacoustic image (envelope), averaged over all the photoacoustic images measured during the PATM measurement, similar to that obtained with uniform illumination. c) Modulation image: the value of each pixel gives the mean modulation depth of the photoacoustic signals (modulus of the transmission matrix), averaged over all input modes. Scale bars: 1 mm.

4.4 Fluctuation imaging for super resolution

In deep tissue PA imaging, the spatial resolution is inherently limited by the acoustic wavelength. Ultimately, the ultrasound resolution in biological soft

tissue imaging is limited by ultrasound attenuation, which typically increases linearly with frequency. As a result, resolution is often traded-off for penetration depth, leading to a depth-to-resolution ratio around 200 in practice [Beard 11, Wang 12]. As an illustration, axial resolution down to ∼5 µm and lateral resolution down to ∼20 µm have been reached with high frequency acoustic detectors at depth up to 5 mm [Omar 14].
In this section, we show that the conventional acoustic-diffraction limit in PA imaging may be overcome by exploiting the exact same PA signal fluctuations introduced in the previous sections. This idea originates from the super-resolution optical fluctuation imaging (SOFI) technique developed for fluorescence microscopy [Dertinger 09]. SOFI is based on the idea that a higher-order statistical analysis of *temporal* fluctuations caused by fluorescence blinking provides a way to resolve fluorophores located within a same diffraction spot. Apart from the origin of the fluctuations, Eq. 4.4 is strictly equivalent to the expression found for the second-order analysis in SOFI [Dertinger 09].
We specifically demonstrate that the analysis of second-order fluctuations of the PA images enables resolving optically absorbing structures beyond the acoustic diffraction limit, with a unidimensional resolution enhancement of about $\sqrt{2} \simeq 1.4$. To fully exploit the highest spatial frequencies available, we implement a deconvolution approach, which results in an effective resolution enhancement of about 1.8 in the lateral direction.

4.4.1 Measurements, signal processing and phantom design

The experimental setup used is described in the previous section and shown in Fig. 4.4.a. We additionally record triggering signals corresponding to the laser pulse emission and the ultrasound scanner acquisition start. These data are necessary to correct the signals for jitters induced by hardware biases. Special care is indeed taken to reduce sources of fluctuations other than the multiple speckle illumination between PA acquisitions. For each sample, a set of PA images was reconstructed for 100 uncorrelated speckle patterns, obtained by rotating the diffuser. The mean and variance images were then computed on a per-pixel basis. For sake of clarity, Eq. 4.4 was written for a noise free situation. In practice, variance between images is also induced by the residual measurement noise and possible triggering-induced temporal jitters, even after the compensation for pulse-to-pulse fluctuations. However, because the deterministic fluctuations from multiple speckle illumination and these other sources of fluctuations are independent, the total variance is given by the sum of the variance of interest (from multiple speckle variations) and the undesirable variance.

Under this assumption, the total measured variance may be written as:

$$\sigma^2[A](\mathbf{r}) \propto \mu_a^2(\mathbf{r}) * h^2(\mathbf{r}) + \epsilon \tag{4.6}$$

The undesirable variance term ϵ is estimated from 100 PA images obtained with a single speckle realisation (static diffuser). It is then subtracted to the previous variance image to obtain an estimate of the variance due solely to multiple speckle illumination. Because only statistical estimation may be produced from a finite set of images, a residual fluctuation necessarily remains present, which can be considered as noise on the variance image.
We design three successive absorbing phantoms using black polyethylene beads (Cospheric, 50 µm and 100 µm in diameter) as isotropic emitters. Estimates of the PSF $h(\mathbf{r})$ are measured using isolated 50 µm diameter microspheres, while ordered patterns to be imaged are formed using 100 µm diameter microspheres. The first sample is made by randomly dispersing beads on the gel block while stiffening. To precisely control the relative position of the beads in the second and third samples, melted gel is first poured on a mold drilled with micrometer precision (Mini Mill, Minitech). The beads are then manually placed in the molded holes of the solidified gel. For each experiment, the absorbing phantom is located 5 cm away from the diffuser, leading to a measured speckle grain size of $\sim$ 30 µm.

4.4.2 Experimental demonstration of super-resolution

As a first demonstration of the resolution enhancement enabled by our approach, Fig. 4.12 shows the mean (conventional) PA image (Fig. 4.12.b) and the variance image (Fig. 4.12.c) obtained with a set of randomly distributed 100 µm diameter absorbing beads (Fig. 4.12.a). It is difficult if not impossible (for instance in the case of the pair pointed out by the red arrow) to unambiguously identify individual beads on the conventional PA image. Individual contributions of each bead clearly overlap because of insufficient resolution. On the opposite, the variance image allows a clear identification of each bead. The dimensions on the images of an isolated 100 µm bead (measured with their envelopes) are 340/414 µm in the lateral/axial directions on the mean image and 246/292 µm on the variance image (insets in Fig. 4.12.b and c), much larger than the diameter of the bead. These images are therefore good approximations of the PSF $h(\mathbf{r})$ and its square $h^2(\mathbf{r})$, and indicates a resolution enhancement factor of about 1.4 in both directions for the variance image as compared to the mean image. As shown in particular with the pair indicated by the arrow on Fig. 4.12.a, the variance image resembles the convolution of the sample with the squared PSF $h^2(\mathbf{r})$, as expected from absorbers distant from more than the speckle grain size and illuminated by multiple independent speckle realisations.

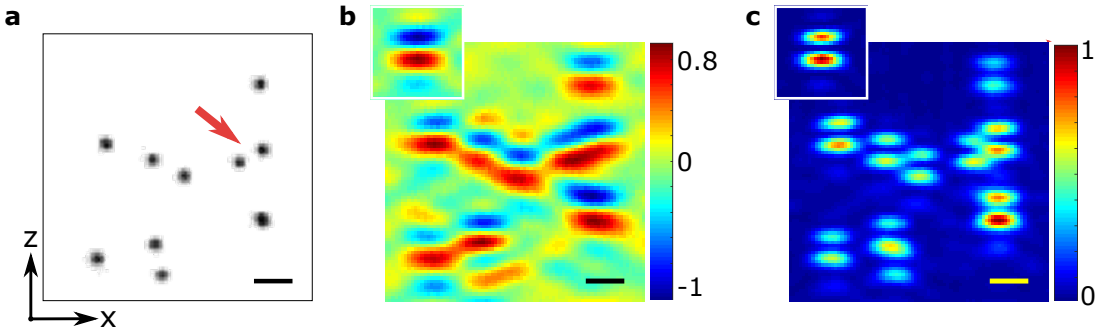

Figure 4.12 – Super-resolution fluctuation photoacoustic imaging. a) Photograph of the first absorbing sample (randomly positioned 100 µm-diameter beads) b) Mean photoacoustic image, averaged over 100 speckle realisations, mimicking uniform illumination. Inset: mean photoacoustic image of a single isolated bead. c) Variance image over 100 speckle realisations. Inset: variance image of a single isolated bead. Scale bars: 300 µm.

The results shown in Fig. 4.12 are a direct illustration of the principle of SOFI applied to PA imaging with multiple speckle illuminations as a fluctuation source. We analyze the higher fluctuation orders in Fig. 4.13. Fig. 4.13.b specifically shows the 4^{th} order cumulant[5]: this image can be shown to only involve the 4^{th} power of the PSF, which would not be the case with the 4^{th} order moment, as stated in [Dertinger 09]. We present in Fig. 4.13.c the cross-sections of the mean, square root of variance and 4^{th} root of 4^{th} order cumulant images along the red dotted line displayed in Fig. 4.13.a. These results clearly demonstrate that, similarly to SOFI imaging, the higher the fluctuation order, the better the resolution. A few problems arise though. First, as the beads do not all have the same absorption, they do not generate PA signals of strictly equal amplitudes. This effect is amplified when analyzing high order fluctuations, and we observe that one bead on the left already prevails in the 4^{th} order cumulant image, as compared to the variance image. Another issue is that the number of uncorrelated speckle illuminations required to compute the high fluctuation orders quickly grows, which limits the practical implementation of the technique [Dertinger 09].

Both Fig. 4.12 and Fig. 4.13 emphasize the bipolarity and anisotropy of the PSF commonly encountered in PA imaging. As a consequence, the PA images appear quite different from the original sample. Moreover, it is known that non-deconvolved images do generally not reflect the highest spatial frequency content available. It was for instance pointed out in the original SOFI paper that a simple deconvolution of the conventional optical image led to a resolution similar to that of the variance image [Dertinger 09]. We illustrate this result in Fig. 4.14.

[5] The 4^{th} order cumulant of the images set is equal to: $\kappa_4 = \langle (A - \langle A \rangle)^4 \rangle - 3\sigma^2[A]$

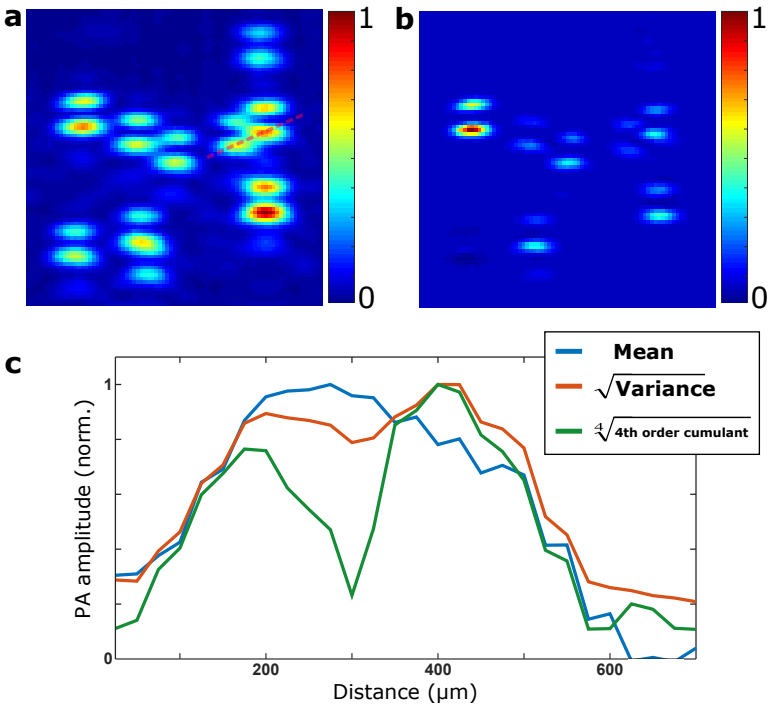

Figure 4.13 – 4^{th} order fluctuations analysis. a) Variance image, computed over 100 photoacoustic images with different speckle realisations. b) 4th order cumulant of the same images set. c) Cross sections along the dotted red line in (a), of the mean image (blue), of the standard deviation image (red), and of the 4^{th} root of 4^{th} order cumulant image (green).

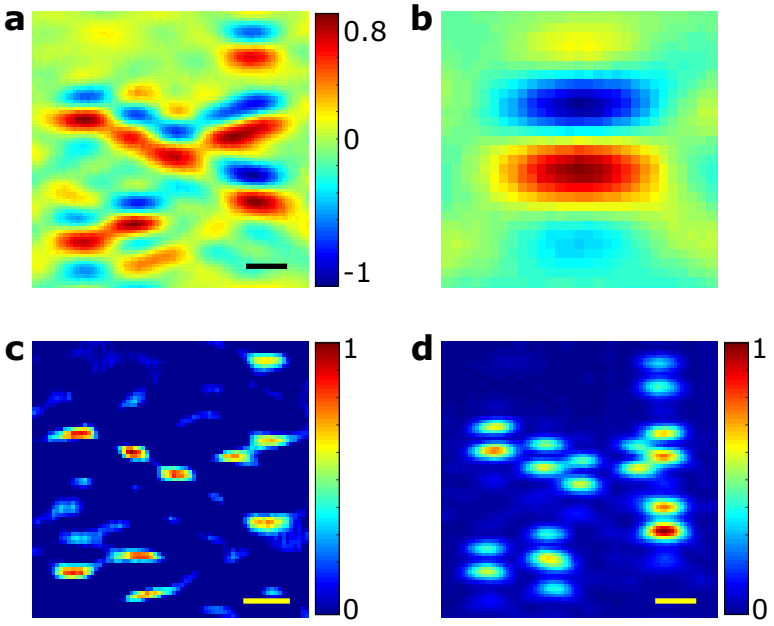

Figure 4.14 – Comparison between variance image and deconvolved mean image. a) Mean photoacoustic image. b) Image of an isolated 100 μm bead, used as PSF for deconvolution of (a). c) Deconvolved mean image (parameters, which will be further described in the next section: N=200, $\alpha = 4.5$). d) Variance image. Scale bars: 300 μm.

4.4.3 Deconvolution approach for ultimate resolution enhancement

To further demonstrate the performances of our approach, we introduce a deconvolution approach to remove the peculiar side lobes of the PA PSF and to fully exploit the maximum available frequency content. We therefore design the phantom shown in Fig. 4.18.a. Pairs of 100 µm diameter beads are positioned along the z and x-axis. The distances between beads (center to center) are: 120 µm, 140 µm and 200 µm along the z direction (from top to bottom), and 250 µm, 200 µm and 160 µm along the x direction (from left to right).

Point spread function analysis

The PSF of the imaging setup is measured by concentrating light on a single 50 µm diameter bead located in the vicinity of the structured 100 µm bead pattern (see Fig. 2.a). This ensures that the 50 µm microsphere is the only PA source. The diffuser is removed from the light path during this step.
Fig. 4.15 shows the PSF (Fig. 4.15.a) as estimated from one of the 50 µm diameter beads of the second sample, its envelope (Fig. 4.15.b), the squared PSF (Fig. 4.15.c) and the square of the PSF envelope (Fig. 4.15.d). The conventional resolution of the imaging system (when using uniform illumination) is given by the FWHM of the envelope of the PSF, while the resolution of the variance image is obtained by the FWHM of the squared envelope of the PSF. The corresponding dimensions are 360/468 µm in the lateral (x-axis)/axial (z-axis) directions on the PSF and 261/338 µm on the squared PSF, resulting in an expected resolution enhancement of about 1.4, which is similar to the factor $\sqrt{2}$ that would be obtained with a regular gaussian PSF [Dertinger 09]. However, it is worth noting that the anisotropy and bipolarity of the PSF are singular features of limited-view and limited-bandwidth PA imaging, and do not have their counterpart in regular all-optical imaging.
Since the squared PSF is sharper than the PSF itself, it should lead to a higher measurable frequency content in the fluctuation image. The spatial frequency content of the PSF and the squared PSF of the PA imaging setup are shown in Fig. 4.16. We observe that for a given noise level, higher spatial frequencies are measurable with the squared PSF, hence on the variance image.
To confirm the spatial invariance of the PSF across the field-of-view, as required by the convolution modeling of the imaging system, PSFs are reconstructed for 4 different locations in the field-of-view. The corresponding results are summarized in Fig. 4.17. With our current ultrasonic detection and the back-projection algorithm, we show that this approach is valid at least for a 3 mm×3 mm field-of-view.

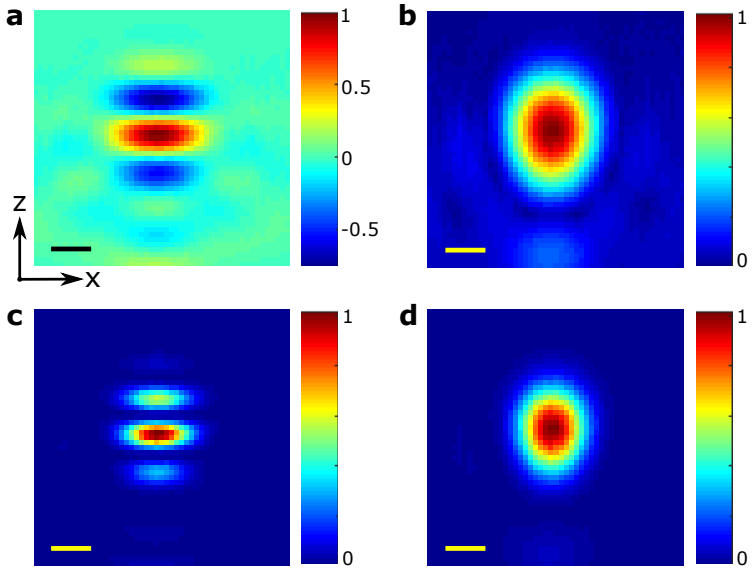

Figure 4.15 – Point spread function of the photoacoustic imaging system. a) PSF $h(\mathbf{r})$ measured with the second sample. b) Envelope of $h(\mathbf{r})$ (modulus of the Hilbert transform along the axial dimension). c) Squared PSF $h^2(\mathbf{r})$. d) Square of the PSF envelope.
Scale bars: 200 µm.

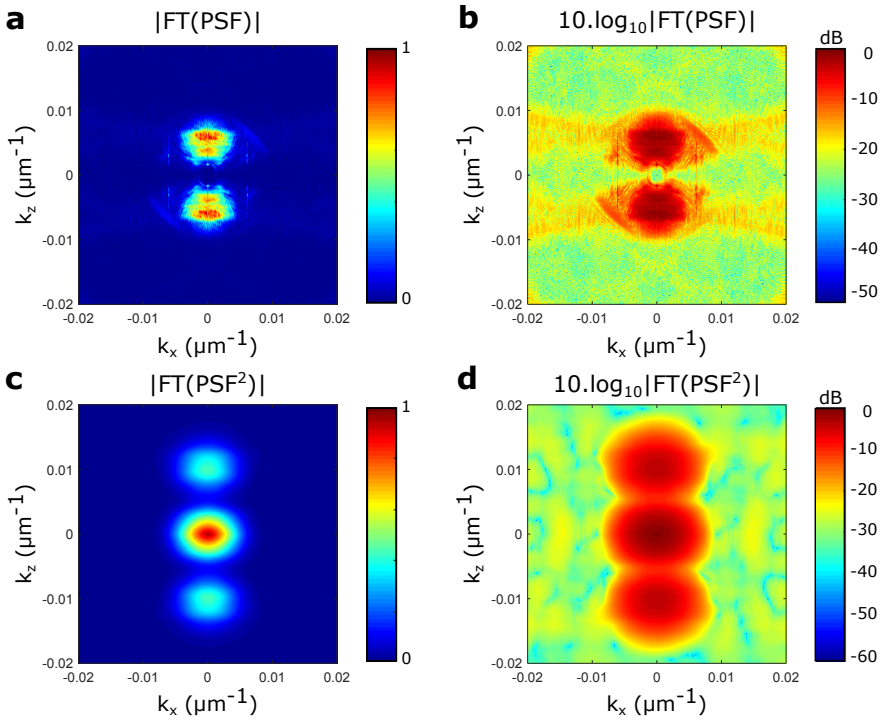

Figure 4.16 – Spatial frequency content of the photoacoustic point spread function. a) Two-dimensional spatial Fourier Transform (magnitude) of the PSF. b) Same as (a) with logarithmic scale. c) Two-dimensional spatial Fourier Transform (magnitude) of the squared PSF. d) Same as (c) with logarithmic scale.

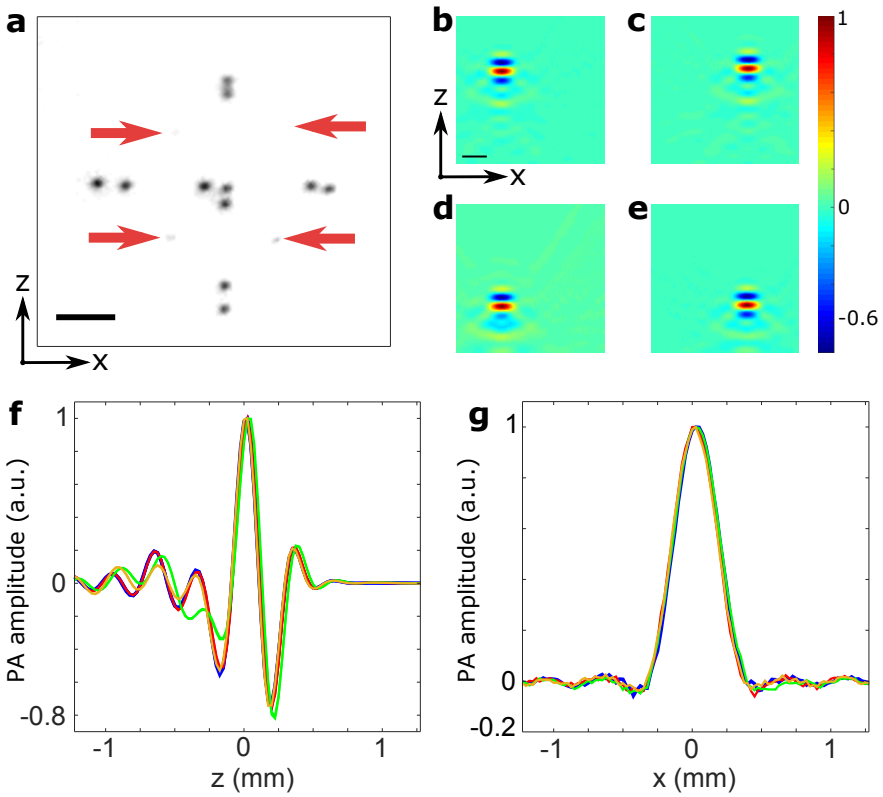

Figure 4.17 – Spatial invariance of the PSF. a) Photograph of the second absorbing sample. The red arrows indicate the locations of the 50 µm-diameter beads used to measure the PSF of the photoacoustic imaging system. b-e) PSF of the photoacoustic imaging setup, recorded at these 4 different locations: (b) Top left, (c) Top right, (d) Bottom left, (e) Bottom right. f) Axial cross-sections of the 4 different PSFs (along z direction): top left (blue), top right (red), bottom left (green), bottom right (yellow). g) Transverse cross-sections of the 4 different PSFs (along x direction). Scale bars: 500 µm.

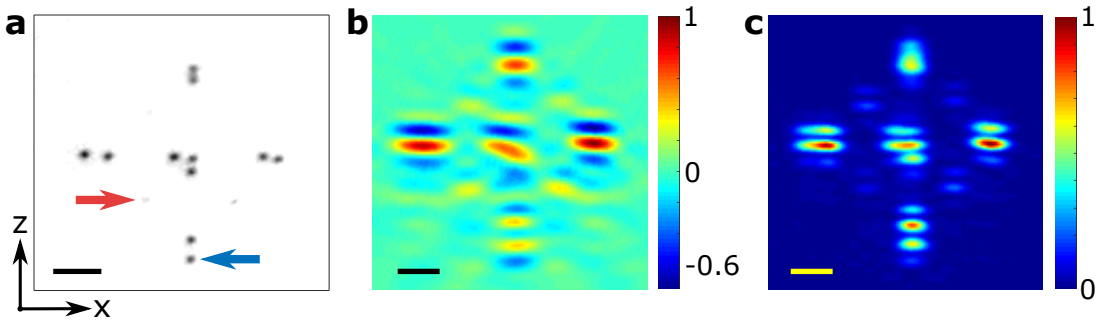

Figure 4.18 – Fluctuation photoacoustic images. a) Photograph of the second absorbing sample: red and blue arrows indicate respectively 50 µm and 100 µm-diameter beads. b) Mean photoacoustic image over 100 speckle realisations, mimicking uniform illumination. c) Square root of the variance image over 100 speckle realisations. Scale bars: 500 µm.

Raw fluctuation imaging

Figures 4.18.b and 4.18.c show that none of the pairs could be resolved on neither the mean nor the variance image, in agreement with the PSF dimensions reported above, and therefore no obvious resolution enhancement can be seen from the comparison of the two images. In order to perform the deconvolution of the images shown in Fig. 4.18 from the knowledge of the PSF (for the mean image) and its square (for the variance image), we use the estimate of the PSF $h(\mathbf{r})$, measured with an isolated 50 µm diameter bead, as pointed out by the red arrow in Fig. 4.18.a.

Deconvolution procedure

Image deconvolution is based on the convolution theorem, which establishes a direct correspondence between convolution in the direct space and pointwise product in the Fourier space:

$$\mathrm{FT}\,(\mathrm{Image}) = \mathrm{FT}\,(\mathrm{Object} * \mathrm{PSF}) = \mathrm{FT}\,(\mathrm{Object}) \cdot \mathrm{FT}\,(\mathrm{PSF})$$

The object can then be retrieved by computing:

$$\mathrm{Object} = \mathrm{FT}^{-1}\left(\mathrm{FT}\,(\mathrm{Image}) \cdot \mathrm{FT}\,(\mathrm{PSF})^{-1}\right) \tag{4.7}$$

In an ideal noise-free situation, deconvolution of an image should retrieve the absorbing object with no resolution limit. However, in the presence of noise, spatial frequencies are accurately measured up to a certain limit set by the SNR, as illustrated in Fig. 4.16. An inversion strategy that allow accounting for the presence of noise in the measurement should therefore be carried out to perform the deconvolution. When FT (PSF) approaches zero, its inverse diverges, and the presence of noise will highly impede the reconstruction accuracy. The inversion should then be carefully regularized. Although we will not use this specific algorithm in the following, we depict the Gerchberg-Papoulis deconvolution algorithm in Fig. 4.19 in order to provide the reader with an intuitive approach of the deconvolution that can be performed. In our experiment, image deconvolution is performed based on Eq. 4.3 and Eq. 4.4 to retrieve the absorption distribution $\mu_a(\mathbf{r})$. The mean and variance images are deconvolved respectively by $h(\mathbf{r})$ and $h^2(\mathbf{r})$ [6].

[6] The deconvolution algorithms have been designed and written by Marc Allain and Anne Sentenac from Institut Fresnel in Marseille (France).

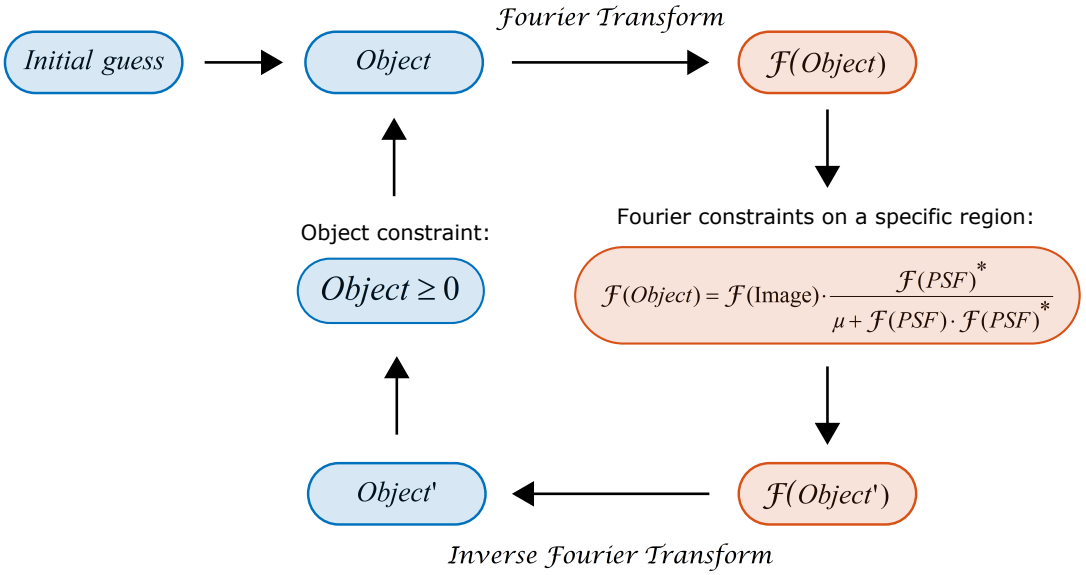

Figure 4.19 – Gerchberg-Papoulis algorithm for image deconvolution with positivity constraint. Typical iteration: the object (initialized with a prior guess) is Fourier transformed. We then apply some constraint in the Fourier space based on Eq. 4.7, on a given spatial frequency domain $([0, k_x^{max}], [0, k_z^{max}])$ for which the SNR is estimated to be high enough. The parameter μ regularizes the inversion. We then perform an inverse Fourier Transform and obtain an "updated" object. We now apply a positivity constraint, as the object is an absorption distribution. This loop is then iterated several times until the process converges. Here, the tuning parameters are μ, k_x^{max}, k_z^{max}, and the number of iterations.

Retrieving $\mu_a^2(\mathbf{r})$ from measurements of the variance image modeled as

$$\widehat{\sigma^2[A]}(\mathbf{r}) = h^2(\mathbf{r}) * \mu_a^2(\mathbf{r}) + \varepsilon$$

(with ε accounting for the experimental noise) is carried out by the minimization of the following constrained least-square functional:

$$J(x) := ||h^2 * x - \widehat{\sigma^2[A]}\ ||^2 + \alpha||x||^2 \quad \text{subject to} \quad x \geq 0 \tag{4.8}$$

with $||\cdot||$ the Euclidian norm over the image space, and $\alpha \geq 0$ a regularization parameter. The constrained minimizer $\widehat{x}_\alpha$ provides a regularized solution to the deconvolution problem, which in turn defines an estimation of the absorption distribution: $\widehat{\mu_a}_\alpha = \sqrt{\widehat{x}_\alpha}$. For accurate comparison, the exact same approach is applied to retrieve an estimation of μ_a from the measurement of the mean image. In practice, the minimization of the functional above required adjusting the regularization parameter α in order to obtain a fair resolution *v.s.* noise tradeoff [Bertero 98, Sec. 5.6], and choosing $N_{\text{iterations}}$ in the numerical method used to perform the minimization.

From a practical viewpoint, an iterative minimization algorithm is required for the numerical evaluation of $\widehat{x}_\alpha$. Since J is a strictly convex functional if $\alpha > 0$, its global minimizer $\widehat{x}_\alpha$ is asymptotically reached by any locally convergent iteration, whatever the initial-guess of the algorithm. For this constrained optimization task, a natural candidate is the standard projected-gradient (PG) since its computational burden is very low. The PG is however rather slow to converge and the FISTA iteration [Beck 09] that achieves a faster convergence is presently considered as a popular alternative and will be used in the following (see appendix D for details).

Deconvolution results

We finally demonstrate that the variance image contains sub-acoustic diffraction information thanks to the higher-frequency content of $h^2(\mathbf{r})$ as compared to $h(\mathbf{r})$, which we now fully exploit thanks to deconvolution.
Deconvolved images are shown in Fig. 4.20. The deconvolved variance image is square rooted to retrieve the absorption distribution $\widehat{\mu_{a_\alpha}}$, in order to be comparable to the deconvolved mean images. The absorbers appear much sharper on the deconvolved variance image (Fig. 4.20.b) as compared to the mean image. Except for the upper pair (120 µm apart axially center to center, for which the beads are nearly touching), almost every pair is resolved on the variance image. On the deconvolved mean image, only the axial pair separated by 200 µm is resolved. Cross-sections along both directions are shown respectively on Fig. 4.20.c and d. These cross-sections show the maximum amplitude projection of the PA image along a ±100 µm band around the white dashed lines plotted in Fig. 4.20.a.
Beads with centers 160 µm apart laterally (respectively 140 µm apart axially) are resolved on the deconvolved variances images, whereas the resolution of the variance image is about 250 µm laterally (resp. about 290 µm axially). The lateral pair 250 µm apart is not resolved in the deconvolved mean image, while the lateral pair 140 µm apart is resolved on the deconvolved variance image. This results in an effective resolution enhancement of at least 1.8. This resolution enhancement is higher than the value of 1.4 derived directly from the FWHM of the PSF $h(\mathbf{r})$ and its square $h^2(\mathbf{r})$.
The underlying reason is that the best achievable resolution not only strongly dependent on the shape of the spatial frequency spectrum of $h(\mathbf{r})$ and $h^2(\mathbf{r})$, but is also fundamentally related to the level at which this spectrum of h or h^2 enters the noise level. As seen in Fig. 4.16, the frequency spectrum of $h^2(\mathbf{r})$ extends further than that of the $h(\mathbf{r})$, with a factor close to 2 in the axial dimension.

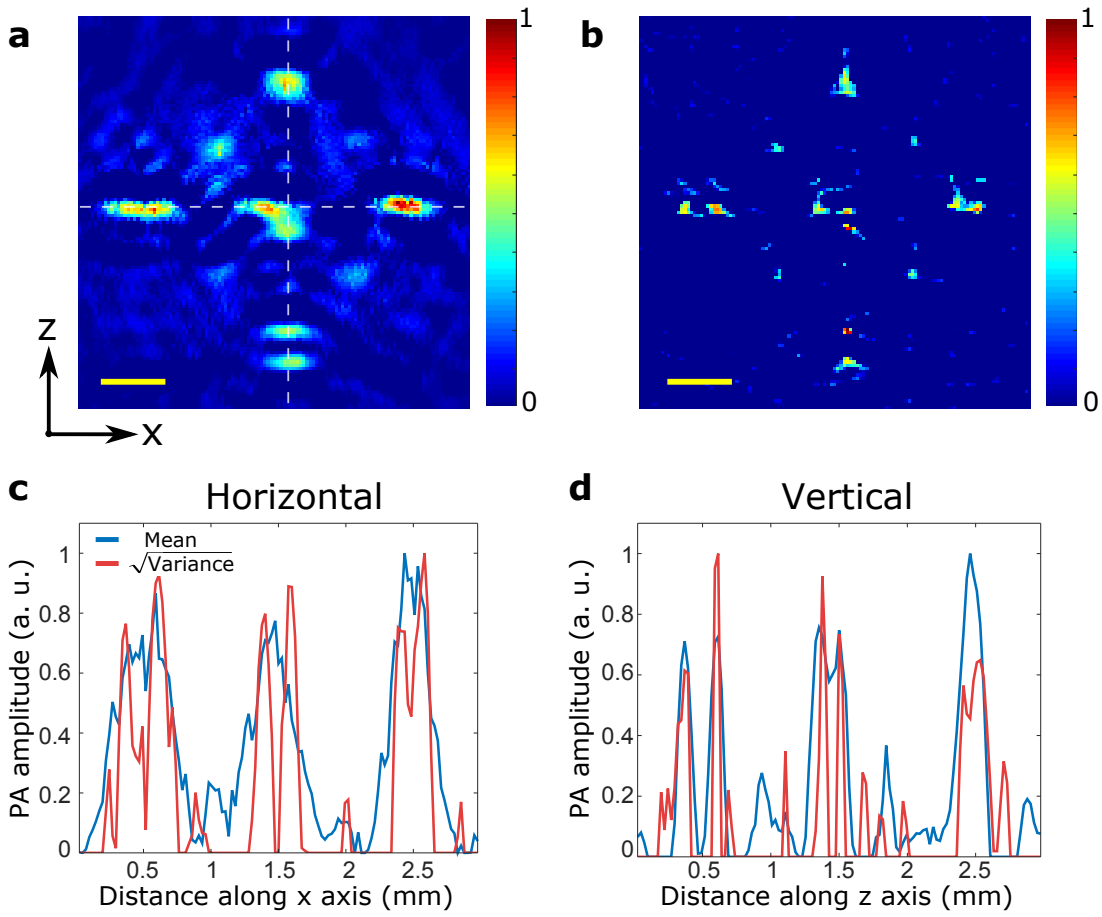

Figure 4.20 – Super-resolution using speckle-induced fluctuation photoacoustic imaging and image deconvolution. a) Mean image deconvolved by the PSF. White dashed lines indicates the cross-section directions. b) Square root of the deconvolved variance image (by the squared PSF). c) Horizontal cross-sections, blue curve: deconvolved mean image, red curve: square root of deconvolved variance image. d) Vertical cross-sections, blue curve: deconvolved mean image, red curve: square root of deconvolved variance image. Scale bars: 500 µm.

The results shown here were independent of the particular PSF (among the 4 displayed in Fig. 4.17) used to perform the deconvolutions, thus validating our assumption that the reconstruction process may be written as a convolution. A slight difference in the PSF shape would results in additional artefacts in the deconvolved image, for instance some rebounds around the reconstructed objects located far from the position where the PSF is measured.

The effect of the PSF anisotropy is further illustrated with the deconvolved images shown in Fig. 4.21. We design a third sample made of 100 µm diameter beads distributed on a quarter circle (center-to-center distance of about 150 µm). Not a single bead can be resolved on the deconvolved mean image (Fig. 4.21.a).

In contrast, the 6 beads can easily be distinguished on the deconvolved variance image (Fig. 4.21.b). The deconvolved images remain anisotropic, as the spatial extent of the PSF in the Fourier space is limited mostly by the temporal frequency bandwidth in the axial direction whereas it is additionally limited by diffraction in the lateral direction. The last two beads on the right are still distinguishable but tend to smear, according to the lower resolution in the lateral x direction. Because of the PSF anisotropy (a consequence of the limited view), we observe that the resolution strongly depends on the angle of the beads pair with respect to the probe surface.

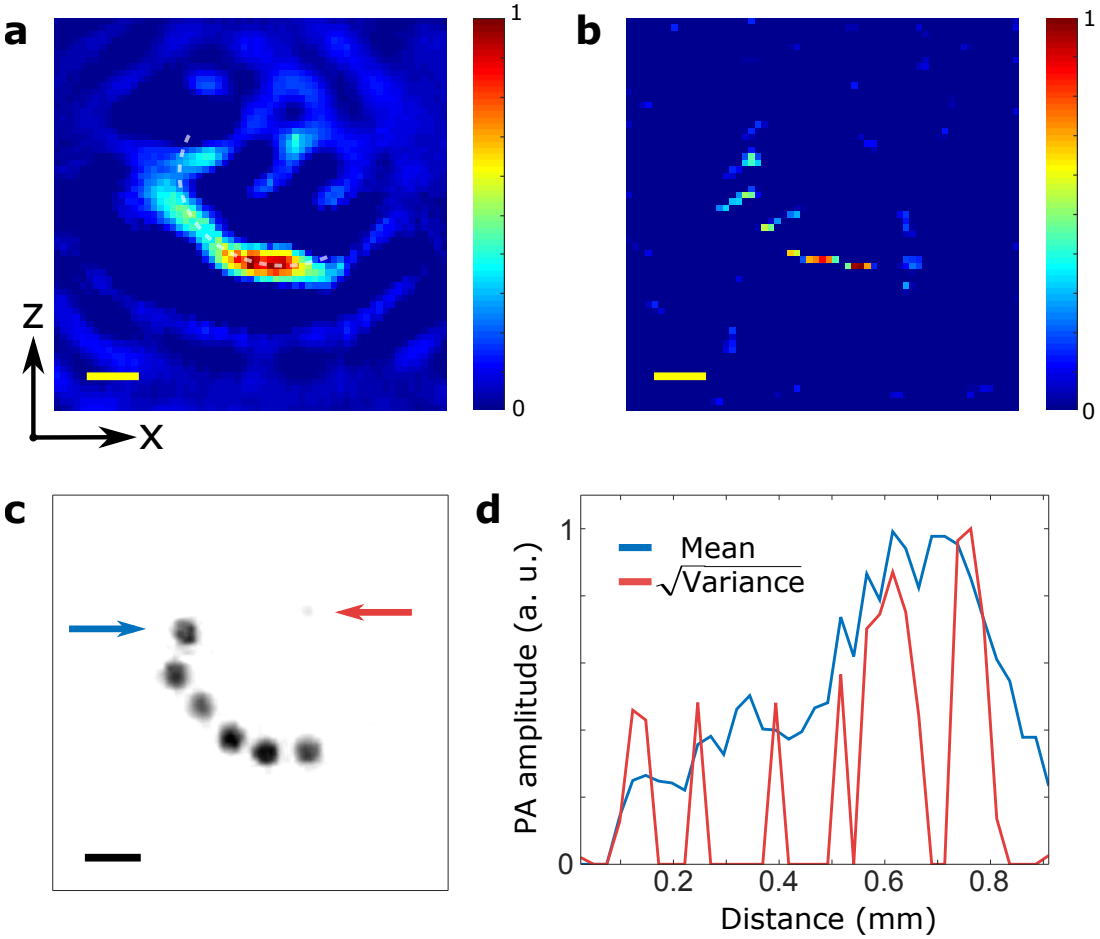

Figure 4.21 – Angular dependence of the PA imaging resolution. a) Mean image deconvolved by the PSF; white dashed lines indicates the cross-section direction. b) Square root of the variance image deconvolved by the squared PSF. c) photograph of the absorbing sample, red and blue arrows indicate respectively 50 µm and 100 µm diameter beads. d) Cross-sections along the beads positions, blue curve: mean image, red curve: square root of variance image. Scale bars: 200 µm.

Deconvolution parameters

According to standard inversion theory [Vogel 02], the regularization parameter should be adjusted so that a trade-off is reached between two opposite behaviors. Whereas an over-estimated parameter α restricts too much the spectral bandwidth of the inverted data, leading to an over-smoothed reconstruction, an under-estimated parameter α inverts some spectral components dominated by noise, leading to unstable reconstructions. In our work, this trade-off is obtained *visually* from reconstructions obtained with various values of the parameter α. In practice, this tuning-step is indeed rather simple as the solution changes smoothly with α (this is a direct consequence of the strict convexity of the criterion). Let us finally note that this optimal tuning is expected to depend both on the square of the PSF $h^2(\mathbf{r})$ and on the noise level in the data to be inverted.
We would like to stress that the same strategy was adopted for the tuning of the regularization parameter in the deconvolution of the mean image. Doing so, the mean and variance images were processed with equivalent care, such that each image exhibits the best accessible resolution. In practice, the parameters used to produce the images shown in the main manuscript were the following:

- for fig 4 (second sample), $\alpha = 10^5$, $N_{\text{iterations}} = 800$.
- for fig 5 (third sample), $\alpha = 10^6$, $N_{\text{iterations}} = 600$.

For each figure, the same parameters were used for the deconvolution of the mean image by the PSF $h(\mathbf{r})$ and the variance image by the square of the PSF $h^2(\mathbf{r})$. The parameters are however different for the two samples, in particular because the PSF was recorded independently for each figure to be sure to obtain the experimental PSF in the vicinity of the object of interest.

4.4.4 Discussion

We showed that speckle-induced PA fluctuation imaging can separate small absorbers unresolved under conventional uniform illumination. This super-resolution PA imaging method does not require optical focusing, and could therefore be readily applied beyond the ballistic regime. Super resolution PA microscopy was reported in previous studies, but it relied on non-linear absorption mechanisms and on light focusing, a situation which cannot be translated to deep tissue PA imaging [Rao 11, Wang 14b].
The common approach to obtain high resolution at depth in PA imaging was to date to improve the acoustic detection by employing higher frequencies and increasing the detection aperture. Here, we demonstrated that additional efforts

can be deployed towards the illumination, in order to induce fluctuations in the PA signal, which enable to separate discrete absorbers below the acoustic diffraction limit. Variance images were shown to provide a resolution enhancement of about 1.4 in both directions as compared to the conventional mean image. Image deconvolution was additionally applied to fully exploit the highest available spatial frequency content in each type of image, limited by the available SNR.
Deconvolution has already been considered in PA imaging, as part of the reconstruction algorithm [Zhang 10] and to compensate for smearing induced by the spatial impulse response of the finite-size detectors [Roitner 14]. However, no super-resolution was yet demonstrated , since there were no physical mechanisms extending the high spatial frequency information. Our approach goes beyond previous works by considering fluctuations in PA images as a signal that reveal higher spatial frequencies above the noise level.
The deconvolution approach was implemented with absorbers of size similar to that of the absorbers used to measure the PSF. As an immediate drawback, deconvolution was unable to restore the actual size of the absorbers, which lead on the deconvolved image to reconstructed beads smaller than their real size. Nonetheless, this method showed a very good sub-acoustic resolution performance, which was the objective of our work. Although the beads were expected to be almost equally absorbing, a difference in the reconstructed amplitudes was noticed. The proposed method was therefore not shown to be quantitative, which could be attributed to the non-linear deconvolution scheme. Further work should be carried out to investigate the possibility to retrieve quantitative absorption information.

4.5 Conclusion

We introduced speckle-induced PA fluctuation imaging, an original method to compensate for partial visibility and to overcome the ultrasound diffraction limit in deep tissue PA imaging. Specifically, we have shown that the non-conventional use of coherent illumination first enables to bypass directivity of the PA emission of elongated absorbing structures. It also enables to image large absorbing objects that radiate low ultrasonic frequencies lying outside the bandwidth of the ultrasonic detector. Finally, we demonstrated the resolution enhancement provided by the analysis of the fluctuations of the PA signal under temporally and spatially fluctuating illumination. The full spatial frequency content was revealed using a deconvolution approach. For these proofs of principle, the speckle illuminations were generated by a rotating scattering layer placed at a given distance from the absorbing sample to control of the speckle grain size. However, for biological applications, tissue-induced temporal decorrelation of speckle patterns could even be exploited as a source of fluctuating illumination. The

natural temporal decorrelation of perfused tissues is indeed of the order of a few milliseconds [Jang 15].
For deep tissue applications, the coherence length of the laser should be longer than the scattering induced optical path-length differences. Path-length differences larger than the laser coherence length may reduce the speckle contrast, and therefore the amplitude of the PA signal fluctuations. In addition, the speckle grain size is expected to decrease towards the quasi-constant value of $\lambda/2$ within depths of the order of the transport mean free path [Pierrat 05]. The contrast of the fluctuations of the PA signal is then expected to be very dim when using low medical ultrasound frequencies. Therefore, higher acoustic resolution may compensate for small optical speckle grain size at depth in tissue. Photoacoustic systems operating at a low-pass cut-off frequency of 125 MHz and reaching depths of at least 5 mm have been developed [Omar 13, Omar 14]. Dynamic coherent illumination could be suited for this mesoscopic system. Additionally, other sources of variability should be minimized, such as detection noise and hardware-induced jitters, to detect small fluctuations in pixel values.
Our proof-of-concept experiments were carried out at low medical ultrasound frequency to simplify the controlled fabrication of absorbing samples. However, the approach could be scaled down using high frequency detectors, and could also be extended to 3D PA imaging. The super-resolution method could also be extended to fluctuation of the absorption induced by blinking or switchable contrast agents [Ng 14].

Conclusion

In this thesis we investigated the control of scattered coherent light by combining optical wavefront shaping with photoacoustic imaging to non-invasively probe the scattered light intensity through (and potentially *inside*) a scattering medium. In addition, we showed that coherent light could significantly improve photoacoustic imaging, by removing artefacts and enhancing the resolution beyond the acoustic diffraction limit. To conclude, we would like to put our work into perspective, and compare it to recent related works carried out by other research groups. In the first chapter, we emphasized the limitations of high resolution optical imaging in biological tissue. Due to light scattering by refractive index fluctuations, diffraction-limited focusing of light is prevented deep inside tissue, typically at depth larger than 1 mm. We described potential approaches to overcome this limitation. Inspired from adaptive optics that compensate for large scale refractive index aberrations, complex wavefront shaping holds much promise for scattered light control. This strategy has been long thought to be irrelevant in the multiple scattering regime, as it would require to control a tremendous number of optical modes to perfectly compensate for the very complex distortions of the wavefront. We highlighted that light focusing can nonetheless be performed through scattering media, using only a reasonable number of controllable degrees of freedom.

To focus light deep inside tissue, wavefront shaping techniques require a precise measurement of the light intensity at the targeted location, which cannot be performed using a conventional camera as the direct optical access is obstructed. In the second chapter, we showed that photoacoustic imaging can be used to non-invasively monitor the scattered light intensity, enabling the measurement of a so-called photoacoustic transmission matrix. The knowledge of this matrix allows to focus light through a scattering layer, enhancing the local photoacoustic signal by a factor depending on the number of SLM pixels. This enhancement factor is about 10 in our experiments. In parallel, the photoacoustic signal enhancement has been shown to improve the contrast of photoacoustic images, since higher light intensities can be delivered on the absorbing sample [Caravaca-Aguirre 13], with potential extrapolation to three-dimensional photoacoustic imaging [Deán-Ben 15b] and flowmetry applications [Tay 14b].

However, photoacoustic-guided wavefront shaping has only been demonstrated through scattering layers, although photoacoustic imaging could be used to probe light intensity deep inside soft tissue. In the specific configuration of an absorbing sample located a few centimeters away from the diffuser, the speckle grain size can be enlarged to reduce the total number of such grains contained within a single acoustic resolution cell. The modulation of the photoacoustic signal can then easily be detected, enabling an accurate measurement of the photoacoustic transmission matrix. Deep inside tissue though, the speckle grain size is $\sim \lambda/2$, i.e. a few hundreds of nanometers, which should be compared to the few tens of micrometers of acoustic resolution for a typical high frequency ultrasonic detector. These specific dimensions lead to a humongous number of speckle grains on the order of several tens of thousands within an acoustic resolution cell. We emphasized that thorough investigations should be carried out to establish whether the number of independent speckle grains can be computed as a surface ratio or as a volume ratio. In any case, the resulting modulation of the photoacoustic signal would therefore be very faint, which would strongly impede the light focusing process.

Several strategies have been studied to overcome this limitation. In the third chapter of this thesis, we took advantage of the broadband frequency content of the measured photoacoustic signal. By filtering the high ultrasonic frequencies of the optimized feedback signal, a smaller focal volume can be probed, thus reducing the number of simultaneously optimized speckle grains. We showed that the photoacoustic signal enhancement was then larger than when optimizing the peak-to-peak photoacoustic signal. We also verified that the focus was tighter when using this high acoustic frequency optimization. The focusing improvement was quite moderate, but this study appeared to be very useful for the global understanding of the specificities of photoacoustic feedback.

For a similar purpose, Conkey and coworkers demonstrated that the gaussian sensitivity profile of a spherically-focused transducer could reduce the effective optimized area, as it attributes more weight to the speckle grains located nearby the transducer axis [Conkey 15]. However, this weighting turns out to be quickly insufficient as soon as the acoustic focus diameter is at least 5 times larger than the speckle grain diameter, since the gaussian profile is quite flat on the center. This feature still reduces the effective number of probed speckle grains by one order of magnitude. Non-linear photoacoustic signal optimization can also be carried out to focus light down to a single speckle grain. It has been demonstrated by Lai and coworkers [Lai 15], and is based on the same principle described for non-linear fluorescence in [Katz 11]. The non-linear photoacoustic generation was performed by firing two successive nanosecond pulses, which can be shown to generate a PA signal related to the squared light intensity through thermal interaction. In order to sense the effect of the first laser pulse, the second one should illuminate the sample within the thermal confinement time on the scale of a single speckle grain. In their experiment, Lai and coworkers used

5 µm-diameter speckle grains, which gives a thermal confinement time of about 200 µs, for a laser pulse separation of 40 µs. Inside tissue however, the speckle grain diameter is at least ten times smaller, leading to a thermal confinement time of 2 µs. This delay is far from being achievable through the only repetition rate of a typical nanosecond laser, but it could eventually be obtained using a (very) long fiber delay line, of about 600 m. Alternatively, photoacoustic contrast agents like gold nanoparticles could also be used for non-linear photoacoustic signal generation [Zharov 11].
Assuming that one is able to obtain a sharp focus deep inside tissue, it would still require to be scanned to build an image. The photoacoustic transmission matrix approach is well suited for such task, but it only allows to focus on absorbing structures. To scan the focus at will deep inside tissue, the memory effect could be employed, as previously demonstrated for fluorescence [Vellekoop 10b]. This effect could be used to scan a focus over a typical distance of a few speckle grain diameters even when considering relatively thick biological samples, based on recent results assessing the speckle correlation range inside forward scattering samples [Schott 15, Judkewitz 15].
Finally, we showed in the fourth chapter that photoacoustic imaging could also be improved in terms of visibility and resolution using multiple speckle illumination. Sub-acoustic resolution photoacoustic images in deep tissue could thus be obtained without focusing light. The main limitation remains the large mismatch between the optical and acoustic resolution, strongly impairing the contrast of the photoacoustic signal fluctuations.

Although we performed proof-of-principle experiments in this thesis, namely using static thin surface diffusers and artificially enlarged speckle grains, we would like to stress that this approach could potentially be used for real tissue applications. To convince the reader, we would like to give a few orders of magnitude. Let us consider a nanosecond pulsed laser, of typical wavelength $\lambda \sim 1$ µm, and a high frequency acoustic detector that can detect up to 100 MHz, thus reaching a typical resolution of 15 µm. This leads to a total number of independent speckle grains equal to $\left(\frac{15}{0.5}\right)^2 = 900$. The modulation contrast of the photoacoustic signal is then equal to $1/\sqrt{3 \times 900} \simeq 0.02$, about one order of magnitude lower than the modulation contrast measured in our experiments. The additional factor $1/\sqrt{3}$ arises from the superposition of three independent speckles corresponding to the three orthogonal polarizations. While this modulation contrast is quite low, it is definitely not out of reach of current acoustic transducers, provided some low noise amplification. Most of the commercially available detectors are optimized for conventional ultrasound imaging, i.e. for both emission and reception. By optimizing the probe for detection, additional sensitivity could be easily obtained.
The coherence length ℓ_c of the laser source should also be taken into account [Goodman 05]. Considering a sample of thickness $d \gg \ell^*$, the typical path

length is of the order of d^2/ℓ^* in the multiple scattering regime. The coherence length of the source should therefore be larger than this path length: $\ell_c \gg \frac{d^2}{\ell^*}$. Considering a thickness of about 3 cm in tissue, the required coherence length is of the order of $\ell_c \sim \frac{(3\text{ cm})^2}{1\text{ mm}} \sim 1$ m. The corresponding minimum pulse duration is then $\tau_p = \ell_c/c \sim 3$ ns. Shorter laser pulses would inevitably degrade the speckle contrast in depth. The nanosecond laser sources that we used (pulse duration ∼5 ns) actually have a much shorter coherence length of the order of a few millimeters. However, it can be improved using a seeded nanosecond pulsed laser [Bjorkholm 69], whose long coherence length still provides speckle formation after several centimeters of propagation in scattering tissue. Alternatively, PA imaging could be performed using intensity-modulated continuous-wave laser to preserve coherence properties [Maslov 08].
Finally, one should be able to run the optimization or measure the photoacoustic transmission matrix before the tissue decorrelates. MEMS and DMDs micromirrors are the two most promising technologies for high speed wavefront shaping, with typical refresh rate of the order of 10 kHz. Although DMDs can only perform binary amplitude modulation, millions of pixels are available compared to the typical thousand pixels of MEMS, at a relatively low cost [Akbulut 11, Conkey 12b, Tay 14b]. The other main limitation for speed requirement is the pulse repetition rate of the laser. The nanosecond pulsed lasers that we used are limited to 10 Hz, but repetition rate of a few kHz can be achieved by some commercially available sources, with comparable average power (cobolt.se, Tor series). As the energy per pulse is consequently lower, it will require a very sensitive, low noise acoustic detection to fully benefit from the high repetition rate. Regarding iterative light focusing, genetic optimization could also be considered, as it is very efficient in a noisy environment and in the presence of speckle decorrelation [Conkey 12a].

Among several potential applications, we would like to mention neuronal imaging. Photoacoustic functional brain imaging has been recently demonstrated, using either blood-oxygen-level-dependent signal contrast [Nasiriavanaki 14] or calcium indicators [Sela 15]. This imaging modality enables to simultaneously image three-dimensional millimeter-scale fields-of-view at video rate, which is currently of great interest in neuroscience [Prevedel 14]. The typical resolution is however on the order of 100 µm and one additional order of magnitude is necessary to achieve single-neuron resolution. The proposed techniques could therefore be applied to provide this resolution enhancement, especially since there is no direct requirement for optical diffraction-limited focusing. Similar techniques could also be applied for specific neuronal photoactivation in deep tissue, for which targeted focusing on single neuron is required [Boyden 05, Papagiakoumou 10].

Appendices

Appendix A

Comparison between random and Hadamard-based partitions for light intensity optimization in the presence of noise: simulations

The basic procedure to focus light through a scattering medium by optimizing of the light intensity of one or several speckle grains is described in section 1.4.2. In essence, the phases of each pixel of the SLM are successively modulated between 0 and 2π, resulting in a sinusoidal modulation of the light intensity of the targeted speckle grain. After each step, the phase of the selected pixel is set as to maximize this intensity. In an ideal noise-free situation, this modulation can always be measured and the optimization procedure easily converges, i.e. reaches the maximum enhancement of the light intensity (Eq. 1.5). In a noisy environment however, this modulation can be too faint to be properly measured. In this case, an alternative method is to simultaneously shift the phases of one half of the SLM pixels in respect to the other at each step. These pixels are usually selected using a random partition [Vellekoop 08a]. However, the number of iterations that are required to converge is larger than the number of SLM pixels N_{SLM}. The SLM phase patterns are indeed highly correlated as the same SLM pixels are shifted for several steps, which is not the case when using the canonical basis (used to span the SLM pixel by pixel).
In this appendix, we introduce the Hadamard basis to form partitions of the SLM pixels with less correlations. Three SLM pixels partitions are illustrated in Fig. A.1: canonical, random, and Hadamard-based. We highlight the fact the SLM patterns used in the proposed methods are not identical to the Hadamard vectors used in the second chapter. In section 2.1 specifically, SLM phase pat-

terns were exactly equal to the phases of Hadamard vectors: one half of the pixels were phase shifted by π as compared to the other half. An additional phase shift was then applied to every pixel, in order to measure the transmission matrix coefficients. Here we use the Hadamard vectors only to select the one half of the pixels that will be phase shifted during the optimization step. Moreover, we emphasize that these partitions are not properly defined mathematical bases, but rather selection patterns.

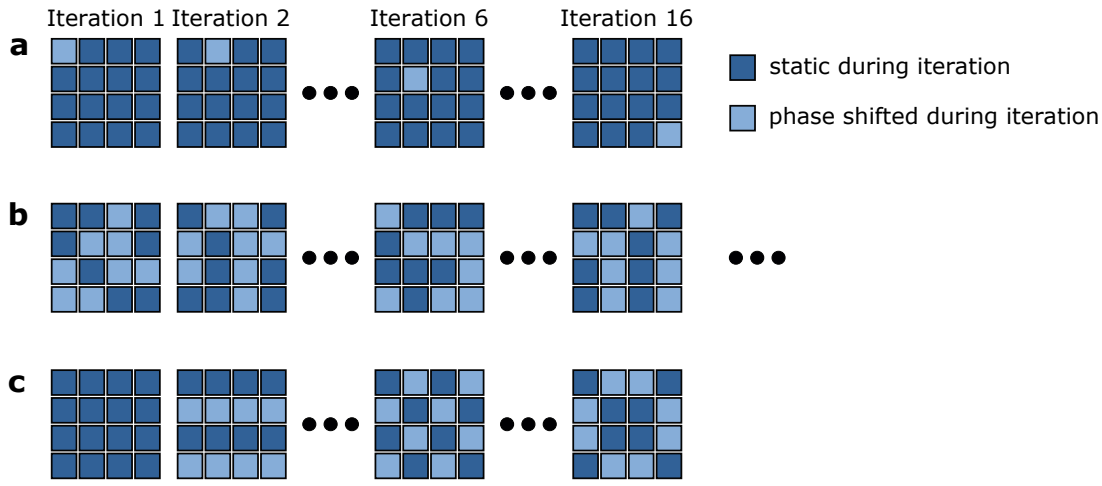

Figure A.1 – SLM partitions for iterative light focusing. a) Canonical partition: one single pixel is modulated at each step. b) Random partition: at each iteration, one randomly selected half of the pixels is modulated. c) Hadamard partition: at each iteration, one half of the pixels is selected based on one Hadamard vector and is modulated.

We simulate the optimization of one single speckle grain intensity to compare the performances of the different pixels partitions. Light scattering is simulated by generating a random phase mask and a gaussian intensity profile. The speckle grain size can be adjusted by tuning the width of this gaussian profile. The speckle pattern is generated by computing the Fourier transform of this complex mask, simulating light propagation in the far-field or equivalently through a lens. The phase control is simulated by applying additional phase shifts on the different pixels of the phase mask. Here the simulated SLM contains $N_{SLM} = 12 \times 12 = 144$ pixels, one pixel of the SLM controls several pixels of the random phase mask, which contains 24×24 pixels. The optimization procedure is then identical to the experimental one, as described in section 1.4.2, performing $4 \times 144 = 576$ steps to observe the convergence of the optimization. We simulate three levels of noise, by adding gaussian distributed random values to the intensity feedback. The gaussian distribution of these values is centered around the mean speckle intensity I_0 and the standard deviation σ is alternatively equal to 0, I_0 and $1.5 \times I_0$. We average 10 different runs of each optimization using different initial random phase masks. Results are presented in Fig. A.2.

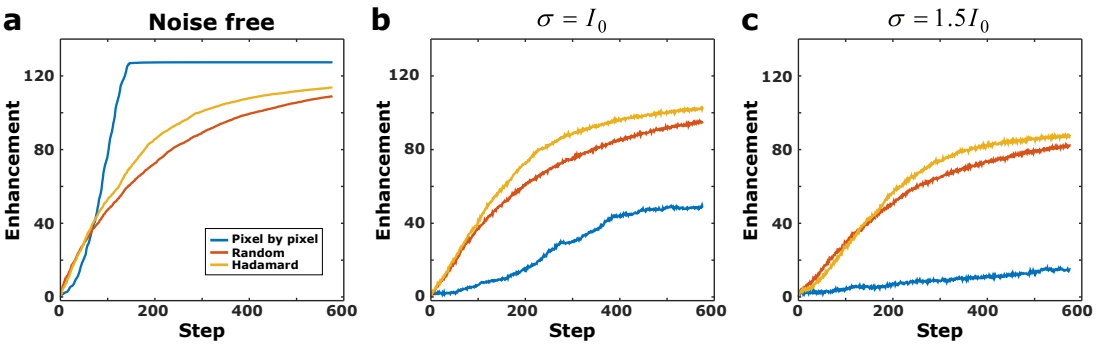

Figure A.2 – Optimization performances of three partition methods: canonical (blue), random (red) and Hadamard-based (yellow).

In the ideal case (Fig. A.2.a), the maximum enhancement (limited by the number of SLM pixels) is first reached by the optimization using the canonical partition, after exactly $N_{SLM} = 144$ iterations. However, this optimization method is very sensitive to noise, as shown in Fig. A.2.b,c. We observe that both random and Hadamard-based partitions are very robust in the presence of noise, but the latter converges faster.

Appendix B

Definition of speckle grain diameter

In this appendix, we consider a fully developed speckle propagating in free space in the z direction. In all experiments of this thesis, the speckle grain diameter (namely its transverse dimension in the xy plane) is assessed by computing the normalized autocovariance C of the speckle intensity pattern (as measured in one given xy plane):

$$C(\mathbf{r}', \mathbf{r}'') = \frac{\langle I(\mathbf{r}') \cdot I(\mathbf{r}'') \rangle - \langle I(\mathbf{r}') \rangle \cdot \langle I(\mathbf{r}'') \rangle}{\langle I(\mathbf{r}') \rangle \cdot \langle I(\mathbf{r}'') \rangle}$$

Thanks to the wide-sense stationarity of the speckle, C actually depends only on the one variable $\mathbf{r} = \mathbf{r}' - \mathbf{r}''$: $C(\mathbf{r}', \mathbf{r}'') = C(\mathbf{r}) = C(x, y)$. According to [Goodman 07], the area of a single speckle grain is measured by computing the equivalent area of this normalized autocovariance function of the speckle intensity:

$$A = \iint_{-\infty}^{+\infty} C(x, y) dx \; dy.$$

The speckle grain diameter is then defined as $\sqrt{A}$. Experimentally, we rather compute the FWHM of C, which is allowed in the case where this width does not depend on a particular direction. If we roughly approximate its profile with a 2D gaussian function $e^{\frac{-(x^2+y^2)}{2\sigma^2}}$, we obtain:

$$\sqrt{A} = \sqrt{2\pi\sigma^2} = \sqrt{2\pi}\sigma$$

$$\text{FWHM} = 2\sqrt{2\ln 2}\sigma = 2\sqrt{\frac{\ln 2}{\pi}} \times \sqrt{A} \simeq 0.9\sqrt{A}$$

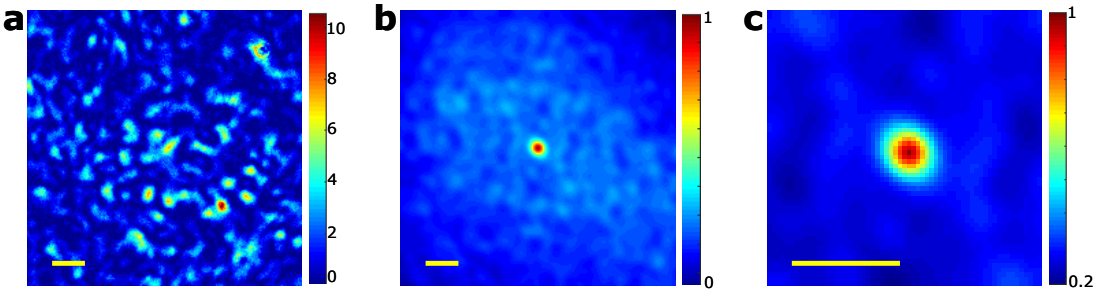

Figure B.1 – Speckle pattern autocovariance. a) Typical speckle pattern generated by light scattering through an engineered diffuser, as measured by a CCD camera located ~ 5 cm away from the diffuser. b) Autocovariance image of (a), normalized by its peak. c) Zoom on (b): the speckle pattern autocovariance is sharply peaked but its peak still exhibit a finite width. Scale bars: 200 µm.

Moreover, this width can be considered to be larger than the actual speckle grain diameter: for instance, the autocovariance of a gaussian function has a FWHM larger by a factor of $\sqrt{2}$ than the FWHM of the gaussian function itself. In the end, we compute the speckle grain diameter as: $L_{speckle} = \frac{1}{\sqrt{2}}\text{FWHM}$.

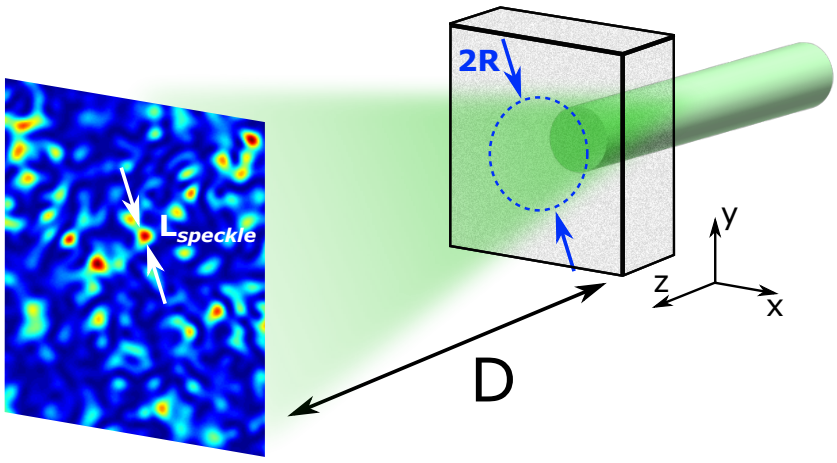

Figure B.2 – Influence of the experimental parameters on the speckle grain size.

In order to relate this speckle grain diameter to experimental parameters, let us consider the following configuration: a collimated laser beam of wavelength λ is illuminating a static scattering sample. The scattering light creates an intensity profile $I_{scat}(x, y)$ at the output of the sample, which in turn generates a speckle pattern after free space propagation over a distance D (see Fig. B.2). The area

of a single speckle grain can be shown to be:

$$A = (\lambda D)^2 \frac{\iint_{-\infty}^{+\infty} I_{scat}^2(x,y)dx\ dy}{\left(\iint_{-\infty}^{+\infty} I_{scat}(x,y)dx\ dy\right)^2}$$

The speckle grain diameter can finally be written as: $L_{speckle} = \frac{1}{\sqrt{2}}\sqrt{A} \propto \frac{\lambda D}{\sqrt{2}}$. When considering for instance I_{scat} as a uniform circular intensity distribution of radius R, this results writes:

$$A = \frac{(\lambda D)^2}{\pi R^2}$$
$$L_{speckle} = \frac{1}{\sqrt{2}}\frac{\lambda D}{\sqrt{\pi} R} \simeq \frac{0.56\lambda D}{R}$$

In the propagation direction z, the typical speckle grain dimension is $\sim 7\lambda\left(\frac{z}{D}\right)^2$. For further details, see section 4.4 of reference [Goodman 07].

Appendix C

Simulations: photoacoustic emission by an cylindrical absorber under speckle illumination, detected by a spherically-focused transducer

In the section 3.4.1, we simulated the optimization of a PA signal generated by an elongated absorber illuminated by a speckle pattern[1]. The speckle generation and the wavefront control are performed as described in appendix A. We describe here the method used to simulate the PA emission by a cylindrical absorber and the detection by a spherically-focused transducer.
The diameter of the transducer is D=4 mm, and its focal length is equal to F=8 mm, leading to a f-number of $\frac{1}{NA} = \frac{F}{D} = 2$. The transducer surface is spatially discretized using a spatial sampling of $3\frac{c_s}{f_{max}}$, where c_s=1500 m.s^{-1} is the sound speed in water and f_{max}=100 MHz is the maximum detectable acoustic frequency. The cylindrical absorber is built by packing point-like emitters separated by 1 µm. Its length is equal to 1 mm. As we simulate an emitter with the acoustic properties of water, we use an effective diameter equal to $\varnothing_{wire}\frac{c_{water}}{c_{nylon}} = 30\frac{1500}{2600} \simeq 17$ µm to simulate the generation of the same acoustic frequencies as in the experiment, where c_{water} and c_{nylon} are the speeds of sound respectively in water and nylon. The same scaling is applied to the speckle grain size.

[1] This simulation has been developed by Jérôme Gateau.

The goal is to compute a 4D matrix, whose first dimension contains the temporal acoustic signal emitted by a point-like absorber whose coordinates are described by the three remaining dimensions of the matrix, as detected by all the discretized elements of the transducer. Thanks to the geometry of the problem, we only compute the PA signals a quarter of the transducer surface, and build the remaining parts using symmetries. For each point-like absorber, we compute the temporal acoustic signal as received by each point-like element of the transducer, i.e. with different temporal delays depending on the relative distance to the emitter. We specifically compute the photoacoustic signal generated by a gaussian pulse excitation of finite duration (5 or 10 ns in section 3.4.1) (see section 1.5 and [Diebold 91]). We then coherently sum these signals to obtain the total acoustic signal emitted by a point-like absorber, as measured by the entire transducer. The PA signal emitted under uniform illumination can then be computed by coherently summing all of these individual signals. To simulate the speckle illumination, we weight the signals emitted at different positions depending on the speckle pattern, and compute the total PA signal by coherently summing the weighted signals. The speckle pattern is here invariant in the light propagation direction (y direction in Fig. C.1).

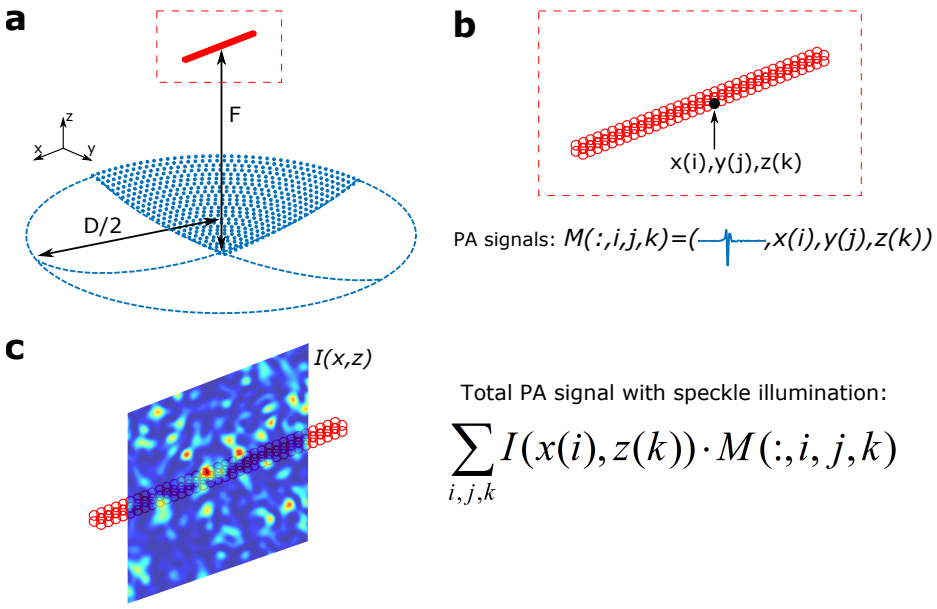

Figure C.1 – Simulation of PA emission and detection of a cylindrical absorber with a spherically-focused single element transducer, using speckle illumination. a) Discretization of the transducer surface (blue dots) and of the absorber (red dots). The dashed blue lines represent the portions of the transducer surface that are built by symmetry. The spatial sampling rates for discretization and the size scale have been reduced for figure readability. b) For each point-like absorber contained in the cylindrical structure, the PA signal measured by the full transducer is computed and stored in the matrix M. c) The signals in M are weighted by the speckle local intensities, and then coherently summed.

Appendix D

FISTA algorithm for image deconvolution

As introduced in the main manuscript, deconvolution of the variance image was performed by minimizing the following constrained least-square functional:

$$J(x) := ||h^2 * x - \widehat{\sigma^2[A]}||^2 + \alpha||x||^2 \quad \text{subject to} \quad x \geq 0 \tag{D.1}$$

In comparison to the standard projected-gradient algorithm [Bertsekas 99], the FISTA method [Beck 09] only requires the additional storage of an auxiliary component $y^{(k)}$. Let $x^{(0)}$ be an initial-guess and $y^{(0)} = x^{(0)}$, the FISTA update for $k = 0, 1, \cdots$ is:

$$\left\{ \begin{array}{rcl} x^{(k+1)} & = & \mathcal{P}_+ \left(y^{(k)} - \theta g(y^{(k)}) \right) \\ y^{(k+1)} & = & x^{(k+1)} + \frac{k-1}{k+2} \left(x^{(k+1)} - x^{(k)} \right) \end{array} \right. \tag{D.2}$$

with $\theta > 0$, $\mathcal{P}_+$ the projection operator over $\mathbb{R}_+$, and g the gradient of the penalized least-square functional above that reads

$$g(x) \; = \; 2 \left(h^2 \right)^\dagger * \left(h^2 * x - \widehat{v} \right) + \alpha x \tag{D.3}$$

where $h^\dagger$ stands for the adjoint of the operator h. It is worth noting that all the convolution operations that appear above can be computed efficiently in the Fourier domain *via* the fast Fourier transform (FFT) and appropriate boundary conditions [Bertero 05]. Finally, the global convergence of Eq. D.2 is granted provided that the constant step-size θ is adjusted within the interval $(0, \overline{\theta})$ with

$$\overline{\theta} \equiv 1 / \max_{\omega} (|\widetilde{h}(\omega)|^2 + \mu)$$

where $\widetilde{h}(\omega)$ stands for the Fourier transform of h.

Bibliography

[Akbulut 11] Duygu Akbulut, Thomas J Huisman, Elbert G van Putten, Willem L Vos & Allard P Mosk. *Focusing light through random photonic media by binary amplitude modulation.* Optics express, vol. 19, no. 5, pages 4017–4029, 2011. 136

[Akkermans 07] Eric Akkermans & Gilles Montambaux. Mesoscopic physics of electrons and photons. Cambridge University Press, 2007. 71

[Aubry 09] Alexandre Aubry & Arnaud Derode. *Random matrix theory applied to acoustic backscattering and imaging in complex media.* Physical review letters, vol. 102, no. 8, page 084301, 2009. 67

[Aviles-Espinosa 11] Rodrigo Aviles-Espinosa, Jordi Andilla, Rafael Porcar-Guezenec, Omar E Olarte, Marta Nieto, Xavier Levecq, David Artigas & Pablo Loza-Alvarez. *Measurement and correction of in vivo sample aberrations employing a nonlinear guide-star in two-photon excited fluorescence microscopy.* Biomedical optics express, vol. 2, no. 11, pages 3135–3149, 2011. 26

[Babcock 53] Horace W Babcock. *The possibility of compensating astronomical seeing.* Publications of the Astronomical Society of the Pacific, pages 229–236, 1953. 25

[Beard 11] Paul Beard. *Biomedical photoacoustic imaging.* Interface focus, vol. 1, no. 4, pages 602–631, 2011. 22, 42, 54, 55, 85, 103, 118

[Beck 09] Amir Beck & Marc Teboulle. *A fast iterative shrinkage-thresholding algorithm for linear inverse problems.* SIAM journal on imaging sciences, vol. 2, no. 1, pages 183–202, 2009. 127, 149

[Bell 80] Alexander Graham Bell. *On the production and reproduction of sound by light.* American Journal of Science, no. 118, pages 305–324, 1880. 43

[Bertero 98] Mario Bertero & Patrizia Boccacci. Introduction to inverse problems in imaging. CRC press, 1998. 126

[Bertero 05] M Bertero & P Boccacci. *A simple method for the reduction of boundary effects in the Richardson-Lucy approach to image deconvolution.* Astronomy & Astrophysics, vol. 437, no. 1, pages 369–374, 2005. 149

[Bertolotti 12] Jacopo Bertolotti, Elbert G van Putten, Christian Blum, Ad Lagendijk, Willem L Vos & Allard P Mosk. *Non-invasive imaging through opaque scattering layers.* Nature, vol. 491, no. 7423, pages 232–234, 2012. 71

[Bertsekas 99] Dimitri P. Bertsekas. Nonlinear programming. Athena Scientific, Belmont, MA, USA, 2nd edition, 1999. 149

[Betzig 06] Eric Betzig, George H Patterson, Rachid Sougrat, O Wolf Lindwasser, Scott Olenych, Juan S Bonifacino, Michael W Davidson, Jennifer Lippincott-Schwartz & Harald F Hess. *Imaging intracellular fluorescent proteins at nanometer resolution.* Science, vol. 313, no. 5793, pages 1642–1645, 2006. 16

[Bjorkholm 69] JE Bjorkholm & HG Danielmeyer. *Frequency control of a pulsed optical parametric oscillator by radiation injection.* Applied Physics Letters, vol. 15, no. 6, pages 171–173, 1969. 136

[Boas 01] David Boas, Dana H Brooks, Eric L Miller, Charles DiMarzio, Misha Kilmer, Richard J Gaudette, Quan Zhang*et al.* *Imaging the body with diffuse optical tomography.* Signal Processing Magazine, IEEE, vol. 18, no. 6, pages 57–75, 2001. 28

[Bohren 08] Craig F Bohren & Donald R Huffman. Absorption and scattering of light by small particles. John Wiley & Sons, 2008. 17

[Booth 14] Martin J Booth. *Adaptive optical microscopy: the ongoing quest for a perfect image.* Light: Science & Applications, vol. 3, no. 4, page e165, 2014. 26

[Bossy 06] Emmanuel Bossy, Khalid Daoudi, Albert-Claude Boccara, Mickael Tanter, Jean-Francois Aubry, Gabriel Montaldo & Mathias Fink. *Time reversal of photoacoustic waves.* Applied physics letters, vol. 89, no. 18, page 184108, 2006. 42, 68

[Boyden 05] Edward S Boyden, Feng Zhang, Ernst Bamberg, Georg Nagel & Karl Deisseroth. *Millisecond-timescale, genetically targeted optical control of neural activity.* Nature neuroscience, vol. 8, no. 9, pages 1263–1268, 2005. 136

[Brillouin 22] Léon Brillouin. *Diffusion de la lumière et des rayons X par un corps transparent homogène. Influence de l'agitation thermique.* Ann. Phys.(Paris), vol. 17, no. 88-122, page 21, 1922. 40

[Calasso 01] Irio G Calasso, Walter Craig & Gerald J Diebold. *Photoacoustic*

point source. Physical Review Letters, vol. 86, no. 16, page 3550, 2001. 46

[Caravaca-Aguirre 13] Antonio M Caravaca-Aguirre, Donald B Conkey, Jacob D Dove, Hengyi Ju, Todd W Murray & Rafael Piestun. *High contrast three-dimensional photoacoustic imaging through scattering media by localized optical fluence enhancement*. Optics express, vol. 21, no. 22, pages 26671–26676, 2013. 91, 133

[Chaigne 14a] T. Chaigne, O. Katz, A.C. Boccara, M. Fink, E. Bossy & S. Gigan. *Controlling light in scattering media non-invasively using the photoacoustic transmission matrix*. Nat Photon, vol. 8, no. 1, pages 58–64, January 2014. 55

[Chaigne 14b] Thomas Chaigne, Jérôme Gateau, Ori Katz, Claude Boccara, Sylvain Gigan & Emmanuel Bossy. *Improving photoacoustic-guided optical focusing in scattering media by spectrally filtered detection*. Optics letters, vol. 39, no. 20, pages 6054–6057, 2014. 86

[Chaigne 14c] Thomas Chaigne, Jérôme Gateau, Ori Katz, Emmanuel Bossy & Sylvain Gigan. *Light focusing and two-dimensional imaging through scattering media using the photoacoustic transmission matrix with an ultrasound array*. Optics letters, vol. 39, no. 9, pages 2664–2667, 2014. 55

[Chaigne 15] Thomas Chaigne, Jérôme Gateau, Marc Allain, Ori Katz, Sylvain Gigan, Anne Sentenac & Emmanuel Bossy. *Super-resolution photoacoustic fluctuation imaging with multiple speckle illumination*. Optica, in press, 2015. 102

[Chandrasekhar 13] Subrahmanyan Chandrasekhar. Radiative transfer. Courier Corporation, 2013. 18

[Cheong 90] Wai-Fung Cheong, Scott A Prahl, Ashley J Welch*et al. A review of the optical properties of biological tissues*. IEEE journal of quantum electronics, vol. 26, no. 12, pages 2166–2185, 1990. 18

[Choi 12] Youngwoon Choi, Changhyeong Yoon, Moonseok Kim, Taeseok Daniel Yang, Christopher Fang-Yen, Ramachandra R Dasari, Kyoung Jin Lee & Wonshik Choi. *Scanner-free and wide-field endoscopic imaging by using a single multimode optical fiber*. Physical review letters, vol. 109, no. 20, page 203901, 2012. 22, 37

[Cizmar 12] Tomas Cizmar & Kishan Dholakia. *Exploiting multimode waveguides for pure fibre-based imaging*. Nature communications, vol. 3, page 1027, 2012. 22

[Conkey 12a] Donald B Conkey, Albert N Brown, Antonio M Caravaca-Aguirre & Rafael Piestun. *Genetic algorithm optimization for focusing through*

turbid media in noisy environments. Optics express, vol. 20, no. 5, pages 4840–4849, 2012. 136

[Conkey 12b] Donald B Conkey, Antonio M Caravaca-Aguirre & Rafael Piestun. *High-speed scattering medium characterization with application to focusing light through turbid media*. Optics express, vol. 20, no. 2, pages 1733–1740, 2012. 37, 136

[Conkey 15] Donald B Conkey, Antonio M Caravaca-Aguirre, Jake D Dove, Hengyi Ju, Todd W Murray & Rafael Piestun. *Super-resolution photoacoustic imaging through a scattering wall*. Nature communications, vol. 6, 2015. 97, 134

[Deán-Ben 15a] X Luis Deán-Ben, Héctor Estrada, Ali Ozbek & Daniel Razansky. *Influence of the absorber dimensions on wavefront shaping based on volumetric optoacoustic feedback*. arXiv preprint arXiv:1506.03617, 2015. 61

[Deán-Ben 15b] X Luís Deán-Ben, Héctor Estrada & Daniel Razansky. *Shaping volumetric light distribution through turbid media using real-time three-dimensional opto-acoustic feedback*. Optics letters, vol. 40, no. 4, pages 443–446, 2015. 133

[Debarre 07] Delphine Debarre, Martin J Booth & Tony Wilson. *Image based adaptive optics through optimisation of low spatial frequencies*. Optics Express, vol. 15, no. 13, pages 8176–8190, 2007. 26

[Debye 32] P Debye & FW Sears. *On the scattering of light by supersonic waves*. Proceedings of the National Academy of Sciences of the United States of America, vol. 18, no. 6, page 409, 1932. 40

[Denk 90] Winfried Denk, James H Strickler & Watt W Webb. *Two-photon laser scanning fluorescence microscopy*. Science, vol. 248, no. 4951, pages 73–76, 1990. 23

[Dertinger 09] Thomas Dertinger, Ryan Colyer, G Iyer, S Weiss & J Enderlein. *Fast, background-free, 3D super-resolution optical fluctuation imaging (SOFI)*. Proceedings of the National Academy of Sciences, vol. 106, no. 52, pages 22287–22292, 2009. 118, 120, 122

[Dickson 97] Robert M Dickson, Andrew B Cubitt, Roger Y Tsien & WE Moerner. *On/off blinking and switching behaviour of single molecules of green fluorescent protein*. Nature, vol. 388, no. 6640, pages 355–358, 1997. 16

[Diebold 91] GJ Diebold, T Sun & MI Khan. *Photoacoustic monopole radiation in one, two, and three dimensions*. Physical review letters, vol. 67, no. 24, page 3384, 1991. 45, 148

[Diebold 94] GJ Diebold & T Sun. *Properties of photoacoustic waves in one, two, and three dimensions.* Acta Acustica united with Acustica, vol. 80, no. 4, pages 339–351, 1994. 113

[Dubois 04] Arnaud Dubois, Kate Grieve, Gael Moneron, Romain Lecaque, Laurent Vabre & Claude Boccara. *Ultrahigh-resolution full-field optical coherence tomography.* Applied optics, vol. 43, no. 14, pages 2874–2883, 2004. 24, 25

[Freund 88] Isaac Freund, Michael Rosenbluh & Shechao Feng. *Memory effects in propagation of optical waves through disordered media.* Physical review letters, vol. 61, no. 20, page 2328, 1988. 68

[Fried 82] David L Fried. *Anisoplanatism in adaptive optics.* JOSA, vol. 72, no. 1, pages 52–61, 1982. 68

[Gateau 13] Jérôme Gateau, Thomas Chaigne, Ori Katz, Sylvain Gigan & Emmanuel Bossy. *Improving visibility in photoacoustic imaging using dynamic speckle illumination.* Optics Letters, vol. 38, no. 23, pages 5188–5191, 2013. 102

[Gateau 15] Jérôme Gateau, Marc Gesnik, Jean-Marie Chassot & Emmanuel Bossy. *Single-side access, isotropic resolution, and multispectral three-dimensional photoacoustic imaging with rotate-translate scanning of ultrasonic detector array.* Journal of biomedical optics, vol. 20, no. 5, pages 056004–056004, 2015. 105

[Gerstner 08] Ed Gerstner. *Adaptive optics: Scattered focus.* Nature Physics, vol. 4, no. 2, pages 91–91, 2008. 38

[Goetschy 13] A Goetschy & AD Stone. *Filtering random matrices: The effect of incomplete channel control in multiple scattering.* Physical review letters, vol. 111, no. 6, page 063901, 2013. 67

[Goodman 05] Joseph W Goodman. Introduction to fourier optics. Roberts and Company Publishers, 2005. 61, 135

[Goodman 07] Joseph W Goodman. Speckle phenomena in optics: theory and applications. Roberts and Company Publishers, 2007. 30, 59, 75, 89, 111, 115, 143, 145

[Goorden 14] Sebastianus A Goorden, Jacopo Bertolotti & Allard P Mosk. *Superpixel-based spatial amplitude and phase modulation using a digital micromirror device.* Optics express, vol. 22, no. 15, pages 17999–18009, 2014. 37

[Goss 79] SA Goss, LA Frizzell & F Dunn. *Ultrasonic absorption and attenuation in mammalian tissues.* Ultrasound in medicine & biology, vol. 5, no. 2, pages 181–186, 1979. 40

[Guo 09] Zijian Guo, Li Li & Lihong V Wang. *On the speckle-free nature of photoacoustic tomography.* Medical physics, vol. 36, no. 9, pages 4084–4088, 2009. 101, 103

[Gusev 93] Vitali Gusev & Aleksandr Karabutov. Laser optoacoustics. American Institute of Physics, 1993. 43

[Hebden 07] Jeremy C Hebden & Topun Austin. *Optical tomography of the neonatal brain.* European radiology, vol. 17, no. 11, pages 2926–2933, 2007. 28

[Hell 94] Stefan W Hell & Jan Wichmann. *Breaking the diffraction resolution limit by stimulated emission: stimulated-emission-depletion fluorescence microscopy.* Optics letters, vol. 19, no. 11, pages 780–782, 1994. 16

[Helmchen 05] Fritjof Helmchen & Winfried Denk. *Deep tissue two-photon microscopy.* Nature methods, vol. 2, no. 12, pages 932–940, 2005. 23

[Hirsch 03] L_R Hirsch, RJ Stafford, JA Bankson, SR Sershen, B Rivera, RE Price, JD Hazle, NJ Halas & JL West. *Nanoshell-mediated near-infrared thermal therapy of tumors under magnetic resonance guidance.* Proceedings of the National Academy of Sciences, vol. 100, no. 23, pages 13549–13554, 2003. 79

[Hooke 03] Robert Hooke. Micrographia: or some physiological descriptions of minute bodies made by magnifying glasses, with observations and inquiries thereupon. Courier Corporation (original edition: James Allestry, 1665), 2003. 7

[Hopkins 54] Harold H Hopkins & Narinder S Kapany. *A flexible fibrescope, using static scanning.* Nature, 1954. 22

[Horstmeyer 15] Roarke Horstmeyer, Haowen Ruan & Changhuei Yang. *Guidestar-assisted wavefront-shaping methods for focusing light into biological tissue.* Nature Photonics, vol. 9, no. 9, pages 563–571, 2015. 37

[Horton 13] Nicholas G Horton, Ke Wang, Demirhan Kobat, Catharine G Clark, Frank W Wise, Chris B Schaffer & Chris Xu. *In vivo three-photon microscopy of subcortical structures within an intact mouse brain.* Nature photonics, vol. 7, no. 3, pages 205–209, 2013. 24

[Hsieh 10a] Chia-Lung Hsieh, Ye Pu, Rachel Grange, Grégoire Laporte & Demetri Psaltis. *Imaging through turbid layers by scanning the phase conjugated second harmonic radiation from a nanoparticle.* Optics Express, vol. 18, no. 20, pages 20723–20731, 2010. 38, 71

[Hsieh 10b] Chia-Lung Hsieh, Ye Pu, Rachel Grange & Demetri Psaltis. *Digital phase conjugation of second harmonic radiation emitted by nanopar-*

ticles in turbid media. Optics express, vol. 18, no. 12, pages 12283–12290, 2010. 38, 39

[Huang 91] David Huang, Eric A Swanson, Charles P Lin, Joel S Schuman, William G Stinson, Warren Chang, Michael R Hee, Thomas Flotte, Kenton Gregory, Carmen A Puliafito*et al. Optical coherence tomography.* Science, vol. 254, no. 5035, pages 1178–1181, 1991. 24

[Huang 13] Bin Huang, Jun Xia, Konstantin Maslov & Lihong V Wang. *Improving limited-view photoacoustic tomography with an acoustic reflector.* Journal of biomedical optics, vol. 18, no. 11, pages 110505–110505, 2013. 73

[Hussain 12] Altaf Hussain, Khalid Daoudi, Erwin Hondebrink & Wiendelt Steenbergen. *Quantitative photoacoustic imaging by acousto-optically measured light fluence.* In Biomedical Optics, pages BM2B–5. Optical Society of America, 2012. 47

[Ishimaru 78] Akira Ishimaru. Wave propagation and scattering in random media, volume 2. Academic press New York, 1978. 19

[Jacques 87] Steven L Jacques, CA Alter & Scott A Prahl. *Angular dependence of HeNe laser light scattering by human dermis.* Lasers Life Sci, vol. 1, no. 4, pages 309–333, 1987. 20

[Jacques 13] Steven L Jacques. *Optical properties of biological tissues: a review.* Physics in medicine and biology, vol. 58, no. 11, page R37, 2013. 18

[Jang 15] Mooseok Jang, Haowen Ruan, Ivo M Vellekoop, Benjamin Judkewitz, Euiheon Chung & Changhuei Yang. *Relation between speckle decorrelation and optical phase conjugation (OPC)-based turbidity suppression through dynamic scattering media: a study on in vivo mouse skin.* Biomedical optics express, vol. 6, no. 1, pages 72–85, 2015. 132

[Jasso 79] Guillermina Jasso. *On Gini's mean difference and Gini's index of concentration.* American Sociological Review, pages 867–870, 1979. 115

[Jose 12] Jithin Jose, Rene GH Willemink, Wiendelt Steenbergen, Cornelis H Slump, Ton G van Leeuwen & Srirang Manohar. *Speed-of-sound compensated photoacoustic tomography for accurate imaging.* Medical physics, vol. 39, no. 12, pages 7262–7271, 2012. 47, 73

[Judkewitz 13] Benjamin Judkewitz, Ying Min Wang, Roarke Horstmeyer, Alexandre Mathy & Changhuei Yang. *Speckle-scale focusing in the diffusive regime with time reversal of variance-encoded light (TROVE).* Nature photonics, vol. 7, no. 4, pages 300–305, 2013. 41, 78

[Judkewitz 15] Benjamin Judkewitz, Roarke Horstmeyer, Ivo M. Vellekoop, Ioannis N. Papadopoulos & Changhuei Yang. *Translation correlations in anisotropically scattering media.* Nature Physics, vol. 11, pages 684–689, 2015. 71, 135

[Kang 15] Sungsam Kang, Seungwon Jeong, Wonjun Choi, Hakseok Ko, Taeseok D Yang, Jang Ho Joo, Jae-Seung Lee, Yong-Sik Lim, Q-Han Park & Wonshik Choi. *Imaging deep within a scattering medium using collective accumulation of single-scattered waves.* Nature Photonics, vol. 9, no. 4, pages 253–258, 2015. 67

[Katz 11] Ori Katz, Eran Small, Yaron Bromberg & Yaron Silberberg. *Focusing and compression of ultrashort pulses through scattering media.* Nature photonics, vol. 5, no. 6, pages 372–377, 2011. 37, 38, 85, 134

[Katz 12] Ori Katz, Eran Small & Yaron Silberberg. *Looking around corners and through thin turbid layers in real time with scattered incoherent light.* Nature Photonics, vol. 6, no. 8, pages 549–553, 2012. 71

[Katz 14] Ori Katz, Eran Small, Yefeng Guan & Yaron Silberberg. *Noninvasive nonlinear focusing and imaging through strongly scattering turbid layers.* Optica, vol. 1, no. 3, pages 170–174, 2014. 37, 71, 85

[Kempe 97] M Kempe, M Larionov, D Zaslavsky & AZ Genack. *Acousto-optic tomography with multiply scattered light.* JOSA A, vol. 14, no. 5, pages 1151–1158, 1997. 40

[Kim 12] Moonseok Kim, Youngwoon Choi, Changhyeong Yoon, Wonjun Choi, Jaisoon Kim, Q-Han Park & Wonshik Choi. *Maximal energy transport through disordered media with the implementation of transmission eigenchannels.* Nature photonics, vol. 6, no. 9, pages 581–585, 2012. 71

[Kino 87] Gordon S Kino. Acoustic waves: devices, imaging, and analog signal processing, volume 107. Prentice-Hall Englewood Cliffs, NJ, 1987. 86

[Kobat 11] Demirhan Kobat, Nicholas G Horton & Chris Xu. *In vivo two-photon microscopy to 1.6-mm depth in mouse cortex.* Journal of biomedical optics, vol. 16, no. 10, pages 106014–106014, 2011. 24

[Kong 11] Fanting Kong, Ronald H Silverman, Liping Liu, Parag V Chitnis, Kotik K Lee & Ying-Chih Chen. *Photoacoustic-guided convergence of light through optically diffusive media.* Optics letters, vol. 36, no. 11, pages 2053–2055, 2011. 42, 54, 78, 84, 91

[Kruger 10] Robert A Kruger, Richard B Lam, Daniel R Reinecke, Stephen P Del Rio & Ryan P Doyle. *Photoacoustic angiography of the breast.* Medical physics, vol. 37, no. 11, pages 6096–6100, 2010. 106

[Kubby 13] Joel A Kubby. Adaptive optics for biological imaging. CRC press, 2013. 33

[Lai 15] Puxiang Lai, Lidai Wang, Jian Wei Tay & Lihong V Wang. *Photoacoustically guided wavefront shaping for enhanced optical focusing in scattering media.* Nature photonics, vol. 9, no. 2, pages 126–132, 2015. 85, 134

[Laufer 09] Jan Laufer, Edward Zhang, Gennadij Raivich & Paul Beard. *Three-dimensional noninvasive imaging of the vasculature in the mouse brain using a high resolution photoacoustic scanner.* Applied optics, vol. 48, no. 10, pages D299–D306, 2009. 105

[Lee 79] Wai-Hon Lee. *Binary computer-generated holograms.* Applied Optics, vol. 18, no. 21, pages 3661–3669, 1979. 37

[Marchetti 07] Enrico Marchetti, Roland Brast, Bernard Delabre, Robert Donaldson, Enrico Fedrigo, Christoph Frank, Norbert Hubin, Johann Kolb, Jean-Louis Lizon, Massimiliano Marchesi*et al.* *On-sky testing of the multi-conjugate adaptive optics demonstrator.* The Messenger, vol. 129, no. 8, 2007. 26

[Maslov 08] Konstantin Maslov & Lihong V Wang. *Photoacoustic imaging of biological tissue with intensity-modulated continuous-wave laser.* Journal of biomedical optics, vol. 13, no. 2, pages 024006–024006, 2008. 136

[McCabe 11] David J McCabe, Ayhan Tajalli, Dane R Austin, Pierre Bondareff, Ian A Walmsley, Sylvain Gigan & Béatrice Chatel. *Spatio-temporal focusing of an ultrafast pulse through a multiply scattering medium.* Nature Communications, vol. 2, page 447, 2011. 24

[Mello 88] Pier A Mello, E Akkermans & B Shapiro. *Macroscopic approach to correlations in the electronic transmission and reflection from disordered conductors.* Physical review letters, vol. 61, no. 4, page 459, 1988. 67

[Minsky 88] Marvin Minsky. *Memoir on inventing the confocal scanning microscope.* Scanning, vol. 10, no. 4, pages 128–138, 1988. 23

[Morel 74] Andre Morel. *Optical properties of pure water and pure sea water.* Optical aspects of oceanography, vol. 1, pages 1–24, 1974. 17

[Mosk 12] Allard P Mosk, Ad Lagendijk, Geoffroy Lerosey & Mathias Fink. *Controlling waves in space and time for imaging and focusing in complex media.* Nature photonics, vol. 6, no. 5, pages 283–292, 2012. 29

[Mudry 12] Emeric Mudry, Kamal Belkebir, J Girard, Julien Savatier, E Le Moal, C Nicoletti, Marc Allain & Anne Sentenac. *Structured illumination*

microscopy using unknown speckle patterns. Nature Photonics, vol. 6, no. 5, pages 312–315, 2012. 101

[Nasiriavanaki 14] Mohammadreza Nasiriavanaki, Jun Xia, Hanlin Wan, Adam Quentin Bauer, Joseph P Culver & Lihong V Wang. *High-resolution photoacoustic tomography of resting-state functional connectivity in the mouse brain*. Proceedings of the National Academy of Sciences, vol. 111, no. 1, pages 21–26, 2014. 136

[Neil 97] MAA Neil, Rimas Juskaitis & Tony Wilson. *Method of obtaining optical sectioning by using structured light in a conventional microscope*. Optics letters, vol. 22, no. 24, pages 1905–1907, 1997. 13

[Ng 14] Kenneth K Ng, Mojdeh Shakiba, Elizabeth Huynh, Robert A Weersink, Aron Roxin, Brian C Wilson & Gang Zheng. *Stimuli-responsive photoacoustic nanoswitch for in vivo sensing applications*. ACS nano, vol. 8, no. 8, pages 8363–8373, 2014. 132

[Ntziachristos 10] Vasilis Ntziachristos. *Going deeper than microscopy: the optical imaging frontier in biology*. Nature methods, vol. 7, no. 8, pages 603–614, 2010. 21

[Omar 13] Murad Omar, Jérôme Gateau & Vasilis Ntziachristos. *Raster-scan optoacoustic mesoscopy in the 25–125 MHz range*. Optics letters, vol. 38, no. 14, pages 2472–2474, 2013. 49, 132

[Omar 14] Murad Omar, Dominik Soliman, Jérôme Gateau & Vasilis Ntziachristos. *Ultrawideband reflection-mode optoacoustic mesoscopy*. Optics letters, vol. 39, no. 13, pages 3911–3914, 2014. 85, 86, 106, 118, 132

[Papadopoulos 12] Ioannis N Papadopoulos, Salma Farahi, Christophe Moser & Demetri Psaltis. *Focusing and scanning light through a multimode optical fiber using digital phase conjugation*. Optics express, vol. 20, no. 10, pages 10583–10590, 2012. 22

[Papagiakoumou 10] Eirini Papagiakoumou, Francesca Anselmi, Aurélien Bègue, Vincent de Sars, Jesper Glückstad, Ehud Y Isacoff & Valentina Emiliani. *Scanless two-photon excitation of channelrhodopsin-2*. Nature methods, vol. 7, no. 10, pages 848–854, 2010. 136

[Pierrat 05] Romain Pierrat, Rachid Elaloufi, Jean-Jacques Greffet & Rémi Carminati. *Spatial coherence in strongly scattering media*. JOSA A, vol. 22, no. 11, pages 2329–2337, 2005. 132

[Popoff 10a] Sébastien Popoff, Geoffroy Lerosey, Mathias Fink, Albert Claude Boccara & Sylvain Gigan. *Image transmission through an opaque material*. Nature Communications, vol. 1, page 81, 2010. 36

[Popoff 10b] SM Popoff, G Lerosey, R Carminati, M Fink, AC Boccara & S Gigan.

Measuring the transmission matrix in optics: an approach to the study and control of light propagation in disordered media. Physical review letters, vol. 104, no. 10, page 100601, 2010. 33, 36, 61, 66, 71, 84

[Popoff 11a] Sébastien Michel Popoff, Alexandre Aubry, Geoffroy Lerosey, Mathias Fink, Albert-Claude Boccara & Sylvain Gigan. *Exploiting the time-reversal operator for adaptive optics, selective focusing, and scattering pattern analysis.* Physical review letters, vol. 107, no. 26, page 263901, 2011. 71, 72

[Popoff 11b] SM Popoff, Geoffroy Lerosey, Mathias Fink, Albert Claude Boccara & Sylvain Gigan. *Controlling light through optical disordered media: transmission matrix approach.* New Journal of Physics, vol. 13, no. 12, page 123021, 2011. 68, 84

[Popoff 14] Sebastien M Popoff, A Goetschy, SF Liew, A Douglas Stone & Hui Cao. *Coherent control of total transmission of light through disordered media.* Physical review letters, vol. 112, no. 13, page 133903, 2014. 67

[Prada 94] Claire Prada & Mathias Fink. *Eigenmodes of the time reversal operator: A solution to selective focusing in multiple-target media.* Wave motion, vol. 20, no. 2, pages 151–163, 1994. 36, 71, 72

[Prada 96] Claire Prada, Sébastien Manneville, Dimitri Spoliansky & Mathias Fink. *Decomposition of the time reversal operator: Detection and selective focusing on two scatterers.* The Journal of the Acoustical Society of America, vol. 99, no. 4, pages 2067–2076, 1996. 71, 72

[Prevedel 14] Robert Prevedel, Young-Gyu Yoon, Maximilian Hoffmann, Nikita Pak, Gordon Wetzstein, Saul Kato, Tina Schrödel, Ramesh Raskar, Manuel Zimmer, Edward S Boyden*et al. Simultaneous whole-animal 3D imaging of neuronal activity using light-field microscopy.* Nature methods, 2014. 136

[Prost 15] Amaury Prost, Florian Poisson & Emmanuel Bossy. *Photoacoustic generation by a gold nanosphere: From linear to nonlinear thermoelastics in the long-pulse illumination regime.* Phys. Rev. B, vol. 92, page 115450, Sep 2015. 45

[Ramon y Cajal 99] Santiago Ramon y Cajal. Comparative study of the sensory areas of the human cortex. 1899. 8

[Ramon Y Cajal 04] S Ramon Y Cajal. Textura del sistema nervioso del hombre y de los vertebrados, volume 2. Madrid Nicolas Moya, 1904. 7

[Rao 11] Bin Rao, Konstantin Maslov, Amos Danielli, Ruimin Chen, K Kirk Shung, Qifa Zhou & Lihong V Wang. *Real-time four-dimensional*

optical-resolution photoacoustic microscopy with Au nanoparticle-assisted subdiffraction-limit resolution. Optics letters, vol. 36, no. 7, pages 1137–1139, 2011. 130

[Razansky 09] Daniel Razansky, Martin Distel, Claudio Vinegoni, Rui Ma, Norbert Perrimon, Reinhard W Köster & Vasilis Ntziachristos. *Multispectral opto-acoustic tomography of deep-seated fluorescent proteins in vivo.* Nature Photonics, vol. 3, no. 7, pages 412–417, 2009. 79

[Razansky 11] Daniel Razansky, Andreas Buehler & Vasilis Ntziachristos. *Volumetric real-time multispectral optoacoustic tomography of biomarkers.* Nature protocols, vol. 6, no. 8, pages 1121–1129, 2011. 105

[Resink 12] Steffen G Resink, Albert C Boccara & Wiendelt Steenbergen. *State-of-the art of acousto-optic sensing and imaging of turbid media.* Journal of biomedical optics, vol. 17, no. 4, pages 0409011–04090110, 2012. 40

[Roddier 99] Francois Roddier. Adaptive optics in astronomy. Cambridge university press, 1999. 25

[Roitner 14] Heinz Roitner, Markus Haltmeier, Robert Nuster, Dianne P O'Leary, Thomas Berer, Guenther Paltauf, Hubert Grün & Peter Burgholzer. *Deblurring algorithms accounting for the finite detector size in photoacoustic tomography.* Journal of biomedical optics, vol. 19, no. 5, pages 056011–056011, 2014. 131

[Rosenthal 13] Amir Rosenthal, Vasilis Ntziachristos & Daniel Razansky. *Acoustic inversion in optoacoustic tomography: A review.* Current medical imaging reviews, vol. 9, no. 4, page 318, 2013. 49

[Santos 09] Silvia Santos, Kengyeh K Chu, Daryl Lim, Nenad Bozinovic, Tim N Ford, Claire Hourtoule, Aaron C Bartoo, Satish K Singh & Jerome Mertz. *Optically sectioned fluorescence endomicroscopy with hybrid-illumination imaging through a flexible fiber bundle.* Journal of biomedical optics, vol. 14, no. 3, pages 030502–030502, 2009. 22

[Schermelleh 10] Lothar Schermelleh, Rainer Heintzmann & Heinrich Leonhardt. *A guide to super-resolution fluorescence microscopy.* The Journal of cell biology, vol. 190, no. 2, pages 165–175, 2010. 16

[Schott 15] Sam Schott, Jacopo Bertolotti, Jean-Francois Léger, Laurent Bourdieu & Sylvain Gigan. *Characterization of the angular memory effect of scattered light in biological tissues.* Optics Express, vol. 23, no. 10, pages 13505–13516, 2015. 71, 135

[Schweiger 99] Martin Schweiger & Simon R Arridge. *Application of temporal filters to time resolved data in optical tomography.* Physics in medicine and biology, vol. 44, no. 7, page 1699, 1999. 24

[Sebbah 02] P Sebbah, B Hu, AZ Genack, R Pnini & B Shapiro. *Spatial-field correlation: the building block of mesoscopic fluctuations.* Physical review letters, vol. 88, no. 12, page 123901, 2002. 67

[Sela 15] Gali Sela, Antonella Lauri, X Luís Deán-Ben, Moritz Kneipp, Vasilis Ntziachristos, Shy Shoham, Gil G Westmeyer & Daniel Razansky. *Functional optoacoustic neuro-tomography (FONT) for whole-brain monitoring of calcium indicators.* arXiv preprint arXiv:1501.02450, 2015. 136

[Sheng 06] Ping Sheng. Introduction to wave scattering, localization and mesoscopic phenomena, volume 88. Springer Science & Business Media, 2006. 19

[Si 12] Ke Si, Reto Fiolka & Meng Cui. *Fluorescence imaging beyond the ballistic regime by ultrasound-pulse-guided digital phase conjugation.* Nature photonics, vol. 6, no. 10, pages 657–661, 2012. 41

[Simandoux 15a] Olivier Simandoux, Amaury Prost, Jérôme Gâteau & Emmanuel Bossy. *Influence of nanoscale temperature rises on photoacoustic generation: Discrimination between optical absorbers based on thermal nonlinearity at high frequency.* Photoacoustics, vol. 3, no. 1, pages 20–25, 2015. 47

[Simandoux 15b] Olivier Simandoux, Nicolino Stasio, Jérome Gateau, Jean-Pierre Huignard, Christophe Moser, Demetri Psaltis & Emmanuel Bossy. *Optical-resolution photoacoustic imaging through thick tissue with a thin capillary as a dual optical-in acoustic-out waveguide.* Applied Physics Letters, vol. 106, no. 9, page 094102, 2015. 22

[Sivankutty 15] Siddharth Sivankutty, Esben Ravn Andresen, Rosa Cossart, Géraud Bouwmans, Serge Monneret & Hervé Rigneault. *Ultra-thin rigid endoscope: Two-photon imaging through a graded-index multi-mode fiber.* arXiv preprint arXiv:1510.04818, 2015. 22

[Sreenivasiah 79] I Sreenivasiah & Akira Ishimaru. *Beam wave two-frequency mutual-coherence function and pulse propagation in random media: an analytic solution.* Applied optics, vol. 18, no. 10, pages 1613–1618, 1979. 61

[Stockbridge 12] C Stockbridge, Y Lu, J Moore, S Hoffman, R Paxman, K Toussaint & T Bifano. *Focusing through dynamic scattering media.* Optics express, vol. 20, no. 14, pages 15086–15092, 2012. 37

[Szabo 14] Vivien Szabo, Cathie Ventalon, Vincent De Sars, Jonathan Bradley & Valentina Emiliani. *Spatially selective holographic photoactivation and functional fluorescence imaging in freely behaving mice with a fiberscope.* Neuron, vol. 84, no. 6, pages 1157–1169, 2014. 22

[Tay 14a] Jian Wei Tay, Puxiang Lai, Yuta Suzuki & Lihong V Wang. *Ultrasonically encoded wavefront shaping for focusing into random media.* Scientific reports, vol. 4, 2014. 41

[Tay 14b] Jian Wei Tay, Jinyang Liang & Lihong V Wang. *Amplitude-masked photoacoustic wavefront shaping and application in flowmetry.* Optics letters, vol. 39, no. 19, pages 5499–5502, 2014. 133, 136

[Thomas 02] Gary E Thomas & Knut Stamnes. Radiative transfer in the atmosphere and ocean. Cambridge University Press, 2002. 20

[Vellekoop 07] IM Vellekoop & AP Mosk. *Focusing coherent light through opaque strongly scattering media.* Optics letters, vol. 32, no. 16, pages 2309–2311, 2007. 8, 29, 30, 31, 32, 61, 66, 84

[Vellekoop 08a] IM Vellekoop & AP Mosk. *Phase control algorithms for focusing light through turbid media.* Optics Communications, vol. 281, no. 11, pages 3071–3080, 2008. 32, 88, 139

[Vellekoop 08b] IM Vellekoop & AP Mosk. *Universal optimal transmission of light through disordered materials.* Physical review letters, vol. 101, no. 12, page 120601, 2008. 67

[Vellekoop 08c] IM Vellekoop, EG Putten, A Lagendijk & AP Mosk. *Demixing light paths inside disordered metamaterials.* Optics express, vol. 16, no. 1, pages 67–80, 2008. 37, 84, 85

[Vellekoop 10a] IM Vellekoop, Ad Lagendijk & AP Mosk. *Exploiting disorder for perfect focusing.* Nature Photonics, vol. 4, no. 5, pages 320–322, 2010. 59, 84

[Vellekoop 10b] Ivo M Vellekoop & Christof M Aegerter. *Scattered light fluorescence microscopy: imaging through turbid layers.* Optics letters, vol. 35, no. 8, pages 1245–1247, 2010. 37, 71, 78, 135

[Vellekoop 12] Ivo M Vellekoop, Meng Cui & Changhuei Yang. *Digital optical phase conjugation of fluorescence in turbid tissue.* Applied physics letters, vol. 101, no. 8, page 081108, 2012. 39

[Ventalon 06] Cathie Ventalon & Jerome Mertz. *Dynamic speckle illumination microscopy with translated versus randomized speckle patterns.* Optics express, vol. 14, no. 16, pages 7198–7209, 2006. 101

[Vermeulen 11] Pierre Vermeulen, Eleonora Muro, Thomas Pons, Vincent Loriette & Alexandra Fragola. *Adaptive optics for fluorescence wide-field microscopy using spectrally independent guide star and markers.* Journal of biomedical optics, vol. 16, no. 7, pages 076019–076019, 2011. 26

[Vogel 02] C. R. Vogel. Computational methods for inverse problems. SIAM (Frontiers in Applied Mathematics), 2002. 130

[Wang 09] Lihong V Wang. *Multiscale photoacoustic microscopy and computed tomography.* Nature photonics, vol. 3, no. 9, pages 503–509, 2009. 22

[Wang 12] Lihong V Wang & Song Hu. *Photoacoustic tomography: in vivo imaging from organelles to organs.* Science, vol. 335, no. 6075, pages 1458–1462, 2012. 42, 43, 79, 118

[Wang 14a] Kai Wang, Daniel E Milkie, Ankur Saxena, Peter Engerer, Thomas Misgeld, Marianne E Bronner, Jeff Mumm & Eric Betzig. *Rapid adaptive optical recovery of optimal resolution over large volumes.* nature methods, vol. 11, no. 6, pages 625–628, 2014. 27

[Wang 14b] Lidai Wang, Chi Zhang & Lihong V Wang. *Grueneisen relaxation photoacoustic microscopy.* Physical review letters, vol. 113, no. 17, page 174301, 2014. 47, 130

[Wilson 11] T Wilson. *Resolution and optical sectioning in the confocal microscope.* Journal of microscopy, vol. 244, no. 2, pages 113–121, 2011. 23

[Xu 04] Yuan Xu, Lihong V Wang, Gaik Ambartsoumian & Peter Kuchment. *Reconstructions in limited-view thermoacoustic tomography.* Medical Physics, vol. 31, page 724, 2004. 75

[Xu 05] Minghua Xu & Lihong V Wang. *Universal back-projection algorithm for photoacoustic computed tomography.* Physical Review E, vol. 71, no. 1, page 016706, 2005. 49, 73

[Xu 06] Minghua Xu & Lihong V. Wang. *Photoacoustic imaging in biomedicine.* Review of Scientific Instruments, vol. 77, no. 4, page 041101, 2006. 42, 49, 79

[Xu 11] Xiao Xu, Honglin Liu & Lihong V Wang. *Time-reversed ultrasonically encoded optical focusing into scattering media.* Nature photonics, vol. 5, no. 3, pages 154–157, 2011. 41, 78, 85

[Yaqoob 08] Zahid Yaqoob, Demetri Psaltis, Michael S Feld & Changhuei Yang. *Optical phase conjugation for turbidity suppression in biological samples.* Nature photonics, vol. 2, no. 2, pages 110–115, 2008. 38

[Zhang 06] Hao F Zhang, Konstantin Maslov, George Stoica & Lihong V Wang. *Functional photoacoustic microscopy for high-resolution and noninvasive in vivo imaging.* Nature biotechnology, vol. 24, no. 7, pages 848–851, 2006. 41, 79

[Zhang 08] Edward Zhang, Jan Laufer & Paul Beard. *Backward-mode multi-*

wavelength photoacoustic scanner using a planar Fabry-Perot polymer film ultrasound sensor for high-resolution three-dimensional imaging of biological tissues. Applied optics, vol. 47, no. 4, pages 561–577, 2008. 47

[Zhang 09] EZ Zhang, JG Laufer, RB Pedley & PC Beard. *In vivo high-resolution 3D photoacoustic imaging of superficial vascular anatomy.* Physics in medicine and biology, vol. 54, no. 4, page 1035, 2009. 85, 97

[Zhang 10] Chi Zhang, Changhui Li & Lihong V Wang. *Fast and robust deconvolution-based image reconstruction for photoacoustic tomography in circular geometry: experimental validation.* Photonics Journal, IEEE, vol. 2, no. 1, pages 57–66, 2010. 131

[Zharov 11] Vladimir P Zharov. *Ultrasharp nonlinear photothermal and photoacoustic resonances and holes beyond the spectral limit.* Nature photonics, vol. 5, no. 2, pages 110–116, 2011. 45, 135